Discrete multitone modulation for short-range optical communications

Please check the document version of this publication:

• A submitted manuscript is the version of the article upon submission and before peer-review. There can be important differences between the submitted version and the official published version of record. People interested in the research are advised to contact the author for the final version of the publication, or visit the DOI to the publisher's website.
• The final author version and the galley proof are versions of the publication after peer review.
• The final published version features the final layout of the paper including the volume, issue and page numbers.

Link to publication

Discrete Multitone Modulation for Short-Range Optical Communications

Jeffrey Lee

Discrete Multitone Modulation for Short-Range Optical Communications

PROEFSCHRIFT

ter verkrijging van de graad van doctor aan de
Technische Universiteit Eindhoven, op gezag van de
rector magnificus, prof.dr.ir. C.J. van Duijn, voor een
commissie aangewezen door het College voor
Promoties in het openbaar te verdedigen
op donderdag 10 december 2009 om 16.00 uur

door

Sian Chong Jeffrey Lee

geboren te Singapore, Singapore

Dit proefschrift is goedgekeurd door promotor:

prof.ir. A.M.J. Koonen

Copromotoren:
Dr.-Ing. S. Randel
en
dr.ir. E. Tangdiongga

*"Empty your mind, be formless. Shapeless, like water.
If you put water into a cup, it becomes the cup. You put water into a bottle and it
becomes the bottle. You put it in a teapot it becomes the teapot.
Now, water can flow or it can crash. Be water my friend."*

Bruce Lee

iv

Summary

Discrete Multitone Modulation for Short-Range Optical Communications

As the need for higher information throughput increases, standard solutions such as copper lines and radio links seem to approach their limits. Therefore, optical solutions, after having conquered the long and medium-range networks, are nowadays also migrating into short-range data communication scenarios, offering the possibility of high capacity information transfer for both professional as well as consumer applications.

The challenge is to offer cost-effective and robust optical solutions at relatively short (≤ 1 km) transmission distances, where traditional single-mode fiber for long-haul transmission systems are unsuitable. Solutions such as multimode glass fibers (MMF), plastic optical fibers (POF), using light-emitting diodes (LED) or low-cost vertical cavity surface emitting laser diodes (VCSEL), and optical wireless links (based on LEDs) are therefore being proposed and seem to be promising candidates. These solutions feature low costs, easy handling and installation, flexibility, and robustness, which are all very suitable characteristics for consumer needs. However, this comes at the expense of less bandwidth when compared to single-mode fiber systems.

This thesis investigates the use of digital signal processing in order to overcome the bandwidth limitations in short-range optical communication systems, ensuring that such solutions are future-proof. In particular, discrete multitone (DMT) modulation is proposed and investigated in order to increase the capacity of such systems. Derived from the more general orthogonal frequency division multiplexing (OFDM), DMT is a baseband multicarrier modulation technique that is already widely employed in copper-based digital subscriber lines (DSL) systems such as asymmetrical DSL (ADSL) and very high data rate DSL (VDSL).

By dividing a high-speed serial data stream into multiple parallel low-speed substreams and transmitting them simultaneously using different frequencies, DMT

Summary

can be used to efficiently combat various signal impairments such as dispersion and narrowband interference. Due to the use of intensity-modulation and direct-detection (IM/DD) in low-cost optical systems, where only the intensity of light is modulated and not the phase, the application of DMT is different from standard electrical systems. Characteristics such as high crest factor, which is the ratio of the peak to root-mean-square amplitude value of the DMT signal, and clipping have different consequences and are studied in this thesis.

After an introduction to the principles of DMT and rate-adaptive bit-loading, an analytical model of the optical IM/DD channel for short-range optical communications is presented. Making use of this model, the theoretical capacity of such a channel is derived for both a Gaussian and a first-order low-pass electrical-to-electrical channel response by means of the water-filling method. It is found that the crest factor of the modulation signal plays a dominant role in defining the capacity of the optical IM/DD channel. Furthermore, by including characteristics of DMT modulation such as clipping and quantization, it is shown that the calculated capacity values can be refined and optimum parameters for DMT transmission over an optical IM/DD channel exist.

Following this, the optimum clipping values and number of subcarriers for maximizing DMT transmission performance over an optical IM/DD channel are investigated. It is shown that the optimum clipping value, which depends on various system parameters such as receiver noise power and modulation order, can be determined by using an analytical expression. In the case of the number of subcarriers, larger values generally lead to better performance when DMT with bit-loading is used.

Additionally, various experiments to explore the system limits of DMT techniques have been performed and the results for POF, MMF, and optical wireless are presented. It is shown that record bit-rates of up to 47 Gbit/s can be achieved using DMT. Finally, an efficient way to implement DMT is presented, together with results regarding the implementation of a real-time DMT transmission system operating at 1.25 Gbit/s. System complexity issues of real-time hardware implementation are also discussed, showing that pipelining and parallelization are essential in high-speed designs, adding to the need of extra hardware resources. Moreover, it is verified that for DMT, the Fast Fourier Transform (FFT) operations require most

hardware resources.

After the presentation of some alternative modulation techniques such as pulse-amplitude-modulated DMT (PAM-DMT), which also were investigated by the author, this thesis ends with the conclusions and some recommendations for further research work.

Contents

CONTENTS

CHAPTER 1
INTRODUCTION

As both the need for higher information throughput as well as user densities are increasing, standard solutions such as copper and radio seem to approach their limits. Besides novel initiatives such as 60 GHz and multiple-input multiple-output (MIMO) techniques, optical solutions are nowadays also migrating into short-range data communication scenarios, offering the possibility for high capacity information transfer in both professional and consumer applications.

The challenge here is to offer cost-effective and robust optical solutions at relatively short ($\leq$1 km) transmission distances, where traditional single-mode fiber systems are too expensive due to the required delicate installation and handling. Alternative solutions such as multimode glass fibers (MMF), plastic optical fibers (POF), light-emitting diodes (LED), and optical wireless (using LED) are therefore being proposed and demonstrated to be promising candidates. Moreover, such solutions can offer signal format transparency, and thus enable to carry services with widely different characteristics in a unified single network.

Major advantages of these proposed solutions are low cost, easy handling and installation, flexibility, and robustness, which are very suitable for consumer needs. However, this comes at an expense of less bandwidth when compared to single-mode fiber systems. This thesis investigates the use of digital signal processing in order to overcome the bandwidth limitations in short-range optical communication systems, thus ensuring that such solutions are future-proof. In particular, discrete multitone

(DMT) modulation is proposed and investigated to increase the capacity of short-range optical communication systems, both for multimode fiber and optical wireless systems.

Derived from the more general orthogonal frequency division multiplexing (OFDM) [1, 2], DMT is a baseband multicarrier modulation technique that is for example employed in digital subscriber lines (DSL) over twisted-pair copper cables such as asymmetric DSL (ADSL) and very high data rate DSL (VDSL) [3, 4, 5]. By dividing a high-speed serial data stream into multiple parallel low-speed sub-streams and transmitting them simultaneously using different frequencies, DMT can be used to efficiently combat various signal impairments such as dispersion and narrowband interference. Due to the use of intensity-modulation and direct-detection (IM/DD) in low-cost optical systems, where only the intensity of light is modulated (and not the phase), the application of DMT is different from standard DSL systems. Characteristics such as high peak-to-average power ratio and clipping have different consequences and are studied in this work. Also, bit-loading algorithms which are typical in DMT systems are investigated for the IM/DD channel and capacity calculations are performed. Moreover, experimental investigations showing record bit-rates of up to 47 Gbit/s DMT transmission are presented and discussed. Finally, the implementation of a real-time DMT transmission system operating at bit-rates beyond 1 Gbit/s is presented and system complexity issues are discussed.

The organization of this thesis is as follows: after an introduction to short-range optical communications, the principle of DMT modulation and bit-loading is presented. Following this, an analytical model for calculating the capacity of short-range optical IM/DD channels is derived, and the influence of using DMT transmission on this capacity is investigated. Furthermore, different parameters of DMT transmission such as clipping, number of subcarriers, and transmitter non-linearity are analyzed and optimum values for maximizing performance are derived. After this, several DMT experiments over POF, silica MMF, and optical wireless are presented, demonstrating the potential of DMT. Real-time implementation of DMT will also be discussed, showing for the first time a 1.25-Gbit/s DMT transmitter for SI-POF applications. After the presentation of pulse-amplitude-modulated DMT (PAM-DMT), this thesis ends with conclusions and recommendations for follow-up research.

CHAPTER 2
SHORT-RANGE OPTICAL
COMMUNICATION

In this chapter, an overview of short-range optical communications is given. POF, MMF, and optical wireless are mentioned including their applications in networks in data-centers, inter-/intra-building, in-building, in-car, industrial automation, inter-/intra computers, mobile phones, wireless usb, HDMI, FireWire, etc.

2.1 Plastic Optical Fibers

With an increasing number and variety of new services being offered like for example VoIP, IPTV, and HDTV, the need for a central distribution network inside buildings and homes is emerging. Such a network should ideally combine large bandwidth with robustness, easy installation, and low cost. Additionally, this network should not only be able to distribute various new services, but also traditional ones such as CATV, voice telephony, high-speed internet, etc., making transparency also an important issue to consider.

Optical fiber enables to open the way towards such a common distribution network. Optical fiber is not susceptible to electromagnetic interference, has no electromagnetic emission and does not conduct electricity so it can be installed in existing conduits used for e.g. main power supply. This makes optical fiber from an instal-

lation point of view very attractive compared with copper coaxial and unshielded twisted pair (UTP) cable.

In particular, plastic optical fiber (POF) is attractive because it is easy to install due to its large core diameter. Moreover, POF offers large flexibility and ductility, which further reduces installation costs in often less accessible customer locations. The large diameter of plastic fiber allows relaxation of connector tolerances without sacrificing optical coupling efficiency. This simplifies the connector design and permits the use of low cost plastic components.

POF exists in many different types and varieties. The most common ones are the step-index poly-methyl-methacrylate (PMMA) POF (SI-POF) and graded-index PMMA POF (GI-POF), both with a core diameter of nearly 1 mm, and the graded-index perfluorinated POF (PF-GI-POF) with core diameters varying from 50 and 65 μm up to 120 μm.

2.1.1 Poly-Methyl-Methacrylate (PMMA) SI-POF

During the past years, the SI-POF has established itself as the preferred alternative transmission medium for robust short-distance data communications in fast-growing markets such as industrial automation networks (PROFINET standard) and multimedia communication in cars (MOST standard). Its main benefits are its robustness to electromagnetic interference and mechanical stress, its ease of installation and connection, its low weight, as well as its low price. Fig. 2.1 shows a comparison of the SI-POF with a standard single-mode silica optical fiber, used for long-haul transmission systems. It can be seen that the 1-mm large diameter of the SI-POF allows easier connection and handling, and at the same time guides more light with larger angle due to the large numerical aperture (NA) of 0.5, resulting in larger tolerances to bending and alignment. Moreover, the large core diameter and large NA also imply a very large number of guided modes, which yields low modal noise in case of fiber coupling misalignments.

With Intel announcing the development of a new high speed USB 3.0 standard including optical capabilities [6], optical communications is also finding its way into the consumer market. Besides the Firewire standard for SI-POF, connector-less SI-POF systems are nowadays available on the consumer market for in-house networks,
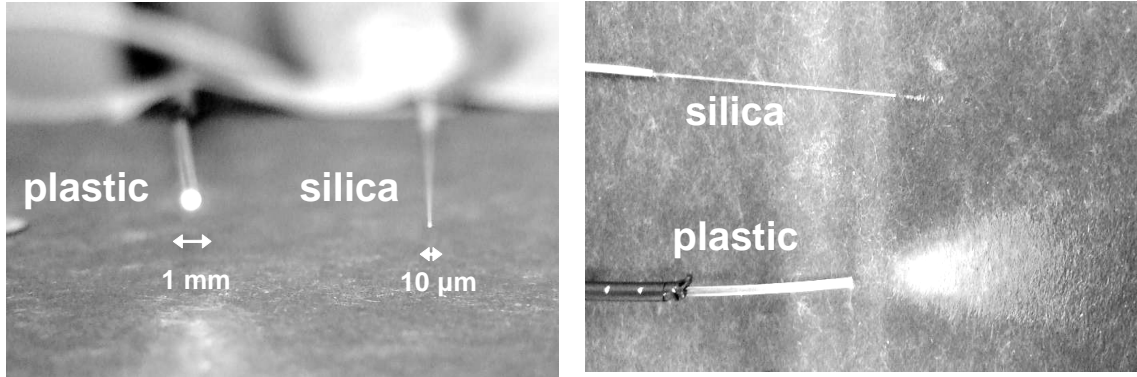
Figure 2.1: Comparison of standard PMMA step-index POF (SI-POF) with silica optical fiber.

supporting various applications such as e.g. IP-TV distribution in homes [7]. While today's commercial systems operate at 100 Mbit/s over up to 100 m of SI-POF, next generation systems are expected to carry Gigabit Ethernet data over comparable distances. However, due to the large amount of modal dispersion resulting from its large numerical aperture (NA) of 0.5, the bandwidth of SI-POF is limited to around 50 MHz × 100 m. This makes the possibility of Gigabit transmission over SI-POF seem unlikely. Nevertheless, several advanced modulation techniques have been proposed recently that make this step feasible [8, 9, 10]. By combining spectral-efficient modulation using high-order quadrature amplitude modulation (QAM) formats with multicarrier modulation and the ability to optimally adapt the transmission parameters per subcarrier to the channel, this thesis proposes and investigates the use of discrete multitone (DMT) modulation for increasing the transmission rates of SI-POF in order to support novel bandwidth-demanding applications.

Fig. 2.2 shows the attenuation curve of the SI-POF for different wavelengths, which is due to the spectral attenuation characteristics of the PMMA material. From this figure, it can be seen that the transmission windows with least attenuation for SI-POF are around 520 nm (blue), 570 nm (green), and 650 nm (red). This implies that the SI-POF should be operated in the visible wavelength range, which eases system inspection (system is working when one can see the light). The most common sources for SI-POF are LEDs, which are available in a large variety of wavelengths. However, the modulation bandwidth of LEDs is usually relatively low (up to at most 200 MHz -3 dB bandwidth). This adds to the bandwidth constraint of SI-
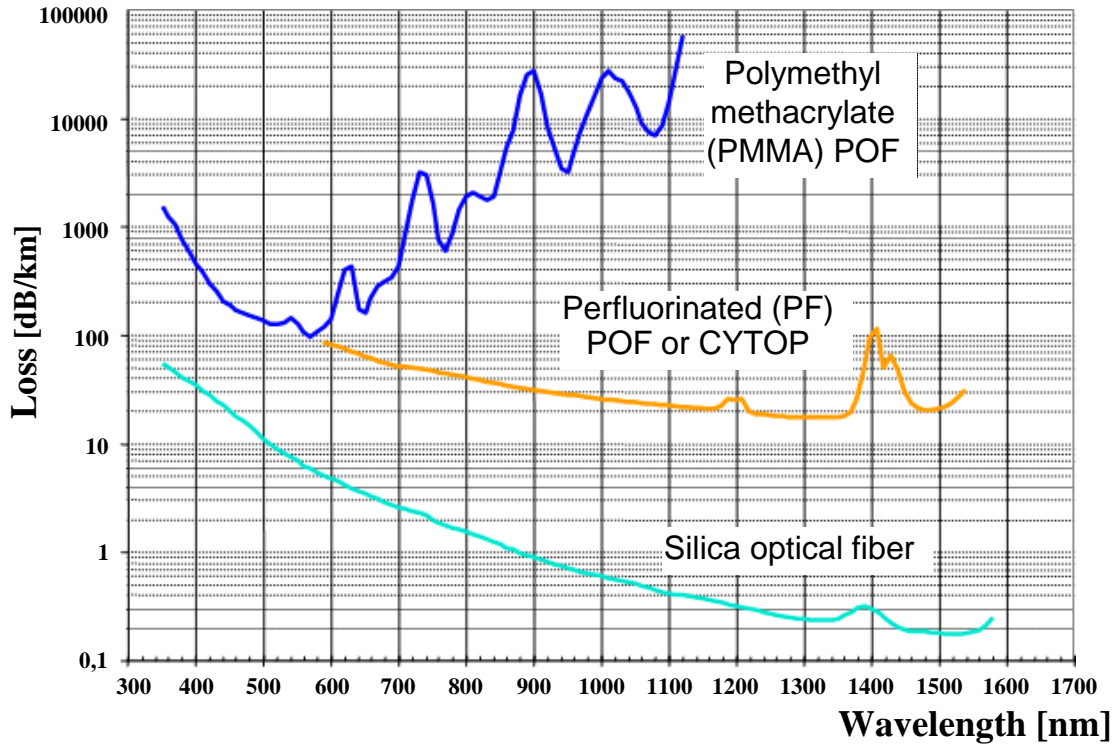
Figure 2.2: Attenuation characteristics of POF and silica fiber.

POF, resulting in even lower transmission rates. A higher-bandwidth alternative is the resonant-cavity LED (RC-LED) [11, 12]. Due to its structure with two reflectors and a cavity that promotes resonance, the RC-LED is able to emit light at higher efficiency. Therefore, larger modulation bandwidths are possible.

Some other higher-bandwidth options are (edge-emitting) laser diodes for DVD applications emitting at a wavelength of around 655 nm, or 670-nm vertical cavity surface emitting lasers (VCSELs) [13]. However, the performance of such transmitters are more dependent on temperature, so that further improvements are necessary for mass consumer application.

Due to the large NA of SI-POF, low-cost, large-diameter (300 μm to 1 mm), standard silicon-based (Si) PIN photodiodes are usually used for detecting the output light of the SI-POF at the receiver end. Therefore, this makes the SI-POF a potentially low-cost system suitable for mass consumer products.

2.1.2   Poly-Methyl-Methacrylate (PMMA) GI-POF

With similar characteristics as the SI-POF, the main difference that characterizes the PMMA GI-POF is the use of a gradient refractive index profile in order to reduce the modal dispersion of the fiber [14, 15, 16]. This results in a higher fiber bandwidth (up to 3 GHz over 50 m), allowing higher transmission rates. Nowadays, commercial GI-POFs are available with core diameters ranging from 0.5 to 1 mm.

However, a major disadvantage of the GI-POF is its high bending loss. This leads to higher attenuation values (approximately 200 dB/km) compared to its step-index counterpart, which is already widely accepted and used in commercial markets. Nevertheless, the GI-POF is a promising candidate for providing Gigabit communication networks in consumer applications and is therefore also considered in this thesis. By using DMT, it is shown that even 10-Gbit/s transmission is possible over such kind of fibers.

This opens another market for PMMA POF, which is high-speed (super-)computer interconnects, server backplane applications, flexible laptop display cables, high-definition multimedia interface (HDMI) [17], etc.

2.1.3   Perfluorinated GI-POF

In recent years, there has been increasing interest for using perfluorinated graded-index POF (PF-GI-POF) for high-speed $\geq$ 10-Gb/s short-reach applications such as low-cost interconnects in data centers, local area networks (LAN), and super-computers. For such applications, multimode fibers (MMF) are preferred above single-mode fiber (SMF) due to their large core diameter and numerical aperture. Especially the PF-GI-POF, with core diameters of 50-62.5 m up to 120 m, is very attractive for such applications. Due to the large alignment tolerances in transceiver components and fiber splices, the PF-GI-POF is attractive for in-building networks as its installation is easy and low cost. In addition, when compared to silica MMF, PF-GI-POF offers further advantages such as smaller bending radius (5 mm), better tolerance to tensile load and stress, and simpler connectorization.

However, the large numerical aperture ($\pm$ 0.2) and refractive index profile of PF-GI-POF also causes its bandwidth to decrease when compared to silica MMF and SMF. In this thesis, the application of DMT to counter such bandwidth problems

and provide 10 to 47-Gbit/s transmission is analyzed and demonstrated.

2.2 Multimode Silica Fibers

Next to POF, silica MMF with core diameters of 50 to 62.5 μm are also attractive for use as high-capacity and low-cost optical fiber-based links in local area networks (LAN), such as enterprise in-building and datacenter backbones, but also short-distance server/computer interconnects. In contrary to long-haul transmission links, silica MMF is used for the vast majority of the optical LAN links [18]. Unlike single-mode fiber, the large core diameter of the MMF allows large alignment and dimensional tolerances in transceiver components, thereby lowering installation, maintenance, and component costs. Therefore, high-speed networking standards like Gigabit Ethernet, Fiber Channel, 10 Gigabit Ethernet, and 40/100 Gigabit Ethernet all include the silica MMF as a transmission medium. Additionally, silica MMF has attenuation values of typically 1 to 3.5 dB/km, which is lower than that of POF. This makes the silica MMF attractive for distances up to a few kilometers.

Being the most-installed type of optical fiber in local area networks and server interconnects [18], silica MMF is a very attractive solution especially for speeds of 10 Gbit/s and beyond. However, transceiver bandwidth limitations ($\approx$ 10 GHz) due to cost reasons are limiting the applicability of silica MMF in short-range optical communication networks to higher speeds defined by for example the 40/100 Gigabit Ethernet standard. By using DMT and bit-loading, it is shown in this thesis that even conventional transceivers with bandwidths of around 10 GHz can be used to achieve up to 40-Gbit/s transmission. Therefore, DMT is a potentially interesting modulation format to consider for high-speed standards in short-range optical communications.

2.3 Optical Wireless

Next to fiber-base optical solutions, optical wireless communications based on low-cost LEDs is also gaining a lot of interest for application in short-range communication for mass consumer products. One of the most popular standards is the
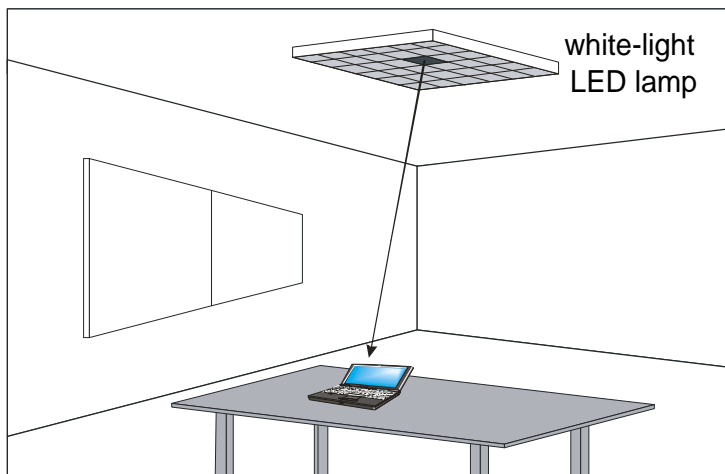
Figure 2.3: Data transmission and illumination scenario using white-light LEDs.

IrDA [19], which can already be found in various applications for information transfer between laptops and mobile phones. Recently the visible light communication consortium [20] was founded to extend this kind of short-range communications for visible light sources.

Another application of optical wireless communications is the use of white-light LEDs meant for illumination purposes. White-light LEDs are expected to become a major player in the future lighting market. So far, the opportunity of modulating their light emission for communication purposes remains untapped. Available modulation bandwidths lie in the MHz range [21, 22] and white-light LEDs might thus serve for illumination and data transmission simultaneously, as illustrated in Fig. 2.3. Advantages would be the inherent low investment and maintenance cost due to the dual-use scenario of illumination and communication, virtually zero interference with radio frequency wireless communication, and the potential to spatially recycle the modulation bandwidth in pico- and femto-cells (due to the pronounced directivity of light and the highly efficient shielding by opaque surfaces).

However, issues such as reflections and interference from other sources should be investigated. By proposing the use of DMT, it is shown in this thesis that high transmission rates up to 100 Mbit/s can be achieved using commercial lighting LEDs due to the high spectral efficiency of DMT. Furthermore, the possibility to adapt the multiple DMT subcarriers at different frequencies in order to cancel out interference

from for example fluorescent lamps proves to be very useful.

Chapter 3
Discrete Multitone Modulation

Discrete multitone modulation (DMT) is a baseband version of the better-known orthogonal frequency division multiplexing (OFDM). While OFDM is known for its mass-application in Wireless Fidelity (WiFi) or wireless local area networks (WLAN) and terrestrial digital video broadcasting (DVB-T), DMT is widely employed in copper-based digital subscriber lines (DSL) for providing high-speed Internet access via asymmetric DSL (ADSL) and very high speed DSL (VDSL).

Due to the already large amount of books and publications on OFDM [1, 2, 23] and DMT [24], this chapter will only give a brief introduction to the principles of DMT. For more details, the reader is recommended to study the aforementioned references.

As this thesis deals with the application of DMT for short-range optical communication networks, this chapter will explain how DMT is beneficial in such systems and how it is applied. A more thorough analysis of this will be given in Section 4.3 of this thesis.

3.1   Principle of DMT Modulation

DMT is a multicarrier modulation technique where a high-speed serial data stream is divided into multiple parallel lower-speed streams and modulated onto

multiple subcarriers of different frequencies for simultaneous transmission [24, 23]. Based on the fast Fourier transform (FFT) algorithm, multicarrier modulation and demodulation are efficiently implemented with DMT. Contrary to OFDM [1, 2], the DMT modulator output signal after the inverse FFT (IFFT) is real-valued and no in-phase and quadrature-phase (IQ-) modulation onto a radio frequency (RF) carrier is required [24, 25, 26]. Therefore, broadband, high-frequency, analog RF-components required for IQ-modulation are omitted from DMT transceivers, reducing system costs and complexity. As a result, only a single digital-to-analog (D/A) converter and a single analog-to-digital (A/D) converter is needed to respectively generate and capture a DMT sequence.

A common misconception of DMT is that it requires twice as much hardware complexity when compared to OFDM. This, however, is not true. A possible reason that gives rise to such a misconception is that in order to generate a multicarrier sequence consisting of N subcarriers, DMT requires the use of an IFFT operation which is twice the length of the one needed for OFDM. Similar, of course, applies to the case of demodulation with an FFT.

As will be shown in (3.1), real-valued input and output sequences of respectively an FFT and IFFT are characterized by symmetry properties. As a result, the FFT and IFFT operations can be optimized for DMT modulation and half of the number of computations can be saved [27, 28]. In Chapter 7.1, a method to efficiently implement a DMT modulator based on the computation of two real-valued FFTs with one complex-valued FFT is presented. Therefore, DMT and OFDM require approximately the same amount of complexity and the longer IFFT/FFT lengths needed for DMT are not disadvantageous.

In Fig. 3.1, the principle of DMT is shown. A high-speed binary serial input data sequence is divided into N parallel lower-speed binary streams. For each stream indexed by n, where $n = 0, 1, \ldots, N-1$, every M number of bits are grouped together and mapped onto complex values $C_n = A_n + jB_n$ according to a quadrature amplitude modulation (QAM) constellation mapping consisting of 2^M states. Usually, the IFFT is used in the DMT transmitter to efficiently modulate the complex values C_n onto N different subcarrier frequencies, which, as a result, are mutually orthogonal [1].

In order to achieve a real-valued, baseband DMT transmission sequence consist-

ing of N subcarriers, a $2N$-point IFFT is needed. For the $2N$ inputs of the IFFT, indexed by $n = 0, 1, \ldots, 2N - 1$, the first half are assigned the values C_n and the second half have to be assigned the complex conjugate values of C_n, following the Hermitian symmetry property given by

$$C_{2N-n} = C_n^* \tag{3.1}$$

for $n = 1, 2, \ldots, N - 1$ and $\text{Im}\{C_0\} = \text{Im}\{C_N\} = 0$. The $\text{Im}\{\cdot\}$ operator denotes the imaginary part. In practice, it is common to set $C_0 = C_N = 0$ so that the resulting DMT sequence does not contain any direct current (DC) value at all.

Following this, the output $u(k)$ of the $2N$-point IFFT is always real-valued, which can be proven by

$$u(k) = \frac{1}{\sqrt{2N}} \sum_{n=0}^{2N-1} C_n \exp\left(j2\pi n \frac{k}{2N}\right) \tag{3.2a}$$

$$= \frac{1}{\sqrt{2N}} \sum_{n=0}^{N-1} \left\{ C_n \exp\left[j2\pi n \frac{k}{2N}\right] + C_n^* \exp\left[j2\pi(2N - n)\frac{k}{2N}\right] \right\} \tag{3.2b}$$

$$= \frac{1}{\sqrt{2N}} \sum_{n=0}^{N-1} \left\{ C_n \exp\left(j2\pi n \frac{k}{2N}\right) + \left[C_n \exp\left(j2\pi n \frac{k}{2N}\right)\right]^* \right\} \tag{3.2c}$$

$$= \frac{1}{\sqrt{2N}} \sum_{n=0}^{N-1} 2 \cdot \text{Re}\left\{ C_n \exp\left(j2\pi n \frac{k}{2N}\right) \right\}, \tag{3.2d}$$

$$k = 0, 1, \ldots, 2N - 1 \tag{3.2e}$$

where the $\text{Re}\{\cdot\}$ operator denotes the real part. For convenience, (3.2) is written as

$$u(k) = \frac{1}{\sqrt{2N}} \sum_{n=0}^{2N-1} C_n \exp\left(j2\pi n \frac{k}{2N}\right), \quad k = 0, 1, \ldots, 2N - 1 \tag{3.3}$$

where $u(k)$, with $k = 0, 1, \ldots, 2N - 1$, is a real-valued sequence consisting of $2N$ points, resulting from every $2N$-point IFFT computation.

Additionally, notice from Fig. 3.1 that a cyclic prefix (CP) is added to $u(k)$ before D/A conversion. The CP is a copy of the last fraction of $u(k)$, which is inserted in front of $u(k)$. For a CP with a length of N_{CP}, the overall sequence can
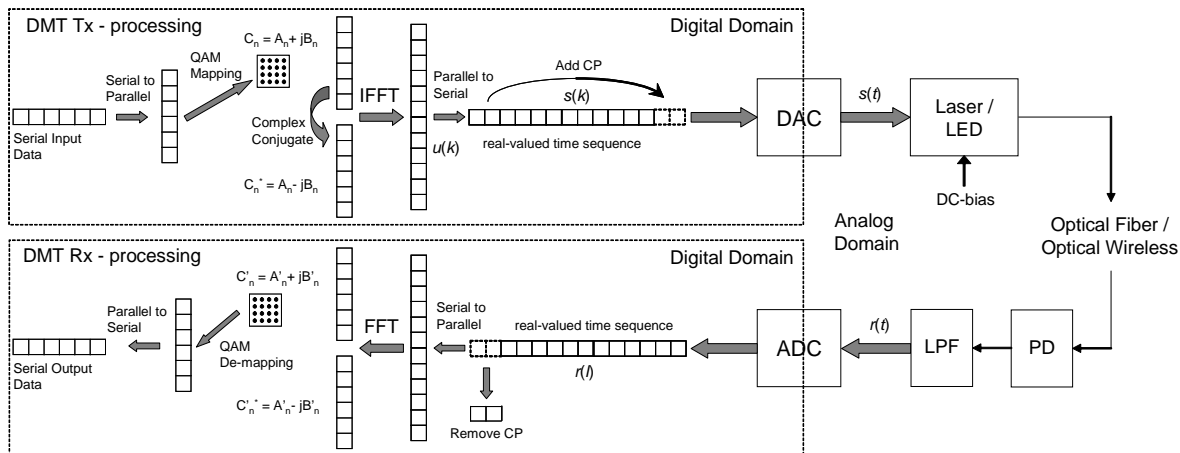
Figure 3.1: Schematic block diagram showing the principle of DMT over an optical IM/DD channel. DAC: digital-to-analog converter, ADC: analog-to-digital converter, LED: light-emitting diode, PD: photodetector, LPF: low-pass anti-aliasing filter, CP: cyclic prefix.

be represented as

$$s(k) = \frac{1}{\sqrt{2N}} \sum_{n=0}^{2N-1} C_n \exp\left(j2\pi n \frac{k - N_{CP}}{2N}\right),$$

$$k = 0, 1, \ldots, 2N - 1 + N_{CP} . \quad (3.4)$$

This $(2N + N_{CP})$-point sequence $s(k)$ corresponds to the samples of the multicarrier DMT time-discrete sequence to be transmitted, which is referred to as a DMT frame in this thesis. Taking the sampling speed of the D/A converter into account, (3.4) is written as

$$s(k) = \frac{1}{\sqrt{2N}} \sum_{n=0}^{2N-1} C_n \exp\left[j2\pi n \frac{(k - N_{CP})\,\Delta t_s}{T}\right],$$

$$k = 0, 1, \ldots, 2N - 1 + N_{CP} \quad (3.5)$$

where $\Delta t_s = 1/f_s$ depicts the sampling period of the D/A converter and f_s its sampling frequency. T is the period of a DMT frame, defined as

$$T = (2N + N_{CP}) \cdot \Delta t_s \quad (3.6)$$

where $1/T = f_{sc}$ is also known as the subcarrier frequency spacing. Note that this subcarrier frequency spacing f_{sc} is not a system parameter that can be chosen

freely, but results indirectly from N, N_{CP}, and the D/A converter sampling speed f_s following the derivation in (3.6).

Depending on the D/A converter impulse response $h_{DAC}(t)$, the resulting time-continuous waveform of each DMT frame after D/A conversion can be written as

$$s(t) = \sum_{k=0}^{2N-1+N_{CP}} s(k)\delta(t - k\Delta t_s) \otimes h_{DAC}(t) \tag{3.7}$$

where $\otimes$ denotes the linear convolution operator and $\delta(t)$ the Dirac impulse. Due to the sample-and-hold function of most D/A converters, $h_{DAC}(t)$ can be modeled as a rectangular pulse ranging from 0 to Δt_s.

Assuming transmission over a linear and lossless channel, the (noise-free) received DMT frame $r(t)$ at the receiver (directly before A/D conversion) can be characterized as

$$r(t) = \sum_{k=0}^{2N-1+N_{CP}} s(k)\delta(t - k\Delta t_s) \otimes h(t) \tag{3.8a}$$

$$= \sum_{k=0}^{2N-1+N_{CP}} s(k)p(t - k\Delta t_s) \tag{3.8b}$$

where $p(t)$ is the pulse shaping function given by

$$p(t) = \delta(t) \otimes h(t) \tag{3.9a}$$

$$= \int_{-\infty}^{\infty} \delta(\tau)h(t - \tau)\, d\tau \tag{3.9b}$$

and $h(t) = h_{DAC}(t) \otimes h_{ch}(t) \otimes h_f(t)$ is the combined impulse response of the D/A converter $h_{DAC}(t)$, the entire channel including the electrical-to-optical and optical-to-electrical conversion $h_{ch}(t)$, and the low-pass, anti-aliasing filter response $h_f(t)$ before A/D conversion. In this analysis, $h(t)$ is assumed to be causal and has a finite time length.

In order for the DMT frames to be received and demodulated properly, two conditions have to be satisfied (refer also to Fig. 3.3):

1. The length of the DMT frame without CP, given by $T - N_{CP} \cdot \Delta t_s$ should be longer than or at least equal to the time length of $h(t)$ in order to avoid inter-frame interference.

2. N_{CP} should be chosen so that its time period $N_{CP} \cdot \Delta t_s$ is longer or equal to the time length of $h(t)$.

Assuming ideal sampling instances and no sampling frequency offset, every received DMT frame $r(t)$ is sampled by the A/D converter with a sampling speed of $f_s = 1/\Delta t_s$, resulting in the discrete samples

$$r(l\Delta t_s) = \sum_{k=0}^{2N-1+N_{CP}} s(k)p\left(l\Delta t_s - k\Delta t_s\right) \tag{3.10a}$$

$$= \sum_{k=0}^{2N-1+N_{CP}} s(k)p\left[(l-k)\,\Delta t_s\right] \tag{3.10b}$$

where, ideally, l should consist of integer values given by $l = -\infty, \ldots, \infty$. However, efficient demodulation of a DMT frame is accomplished by use of a $2N$-point FFT, so that $r(l\Delta t_s)$ can only consist of $2N$ points per DMT frame. If N_{CP} is chosen so that its time period $N_{CP} \cdot \Delta t_s$ is long enough to represent the entire pulse shape $p(t)$, choosing $l = N_{CP}, N_{CP}+1, \ldots, 2N-1+N_{CP}$ will result in FFT demodulation of a DMT frame $r(l\Delta t_s)$ given by

$$\hat{C}_n = \sum_{l=N_{CP}}^{2N-1+N_{CP}} r(l\Delta t_s) \exp\left[-j2\pi\left(l - N_{CP}\right)\frac{n}{2N}\right] \tag{3.11a}$$

$$= \sum_{l=N_{CP}}^{2N-1+N_{CP}} \sum_{k=0}^{N_{CP}} s(k)p\left[(l-k)\,\Delta t_s\right] \exp\left[-j2\pi\left(l - N_{CP}\right)\frac{n}{2N}\right] \tag{3.11b}$$

$$= H_n \cdot \sum_{l=N_{CP}}^{2N-1+N_{CP}} s(l) \exp\left[-j2\pi\left(l - N_{CP}\right)\frac{n}{2N}\right] \tag{3.11c}$$

$$= H_n \cdot \sum_{k=0}^{2N-1} u(k) \exp\left(-j2\pi k\frac{n}{2N}\right) \tag{3.11d}$$

$$= |H_n| \cdot \exp(-j\phi_n) \cdot C_n \,, \qquad n = 0, 1, \ldots, 2N-1 \,. \tag{3.11e}$$

H_n is the $2N$-point FFT of the channel impulse response $h(t)$ at index/subcarrier n, where $n = 0, 1, \ldots, 2N-1$. This can also be considered as a multiplicative gain $|H_n|$ and a phase shift $\exp(-j\phi_n)$ of each subcarrier in the received DMT frame. Usually, preamble DMT frames with known data values are transmitted in a DMT system in order to estimate $|H_n|$ and $\exp(-j\phi_n)$ of the transmission channel. At the

receiver, multiplying $\hat{C}_n$ with $1/H_n$ will result in the transmitted symbols C_n. This operation is often denoted as one-tap, zero-forcing, frequency-domain equalization.

From (3.11), it can be seen that inclusion of the CP allows the linear convolution of the DMT frame $s(t)$ with the channel impulse response $h(t)$ to be converted into a cyclic convolution. Therefore, demodulation with the FFT will result in just a complex multiplication of the sent data symbols with the channel response. When no CP is used, demodulation with the FFT will result in inter-carrier interference. This is also schematically represented in Fig. 3.3. Naturally, the inclusion of a CP comes at the expense of additional redundancy.

3.2   DMT in an Optical IM/DD Channel

Especially in low-cost optical communication systems such as multimode fiber and optical wireless systems, intensity-modulation and direct-detection (IM/DD) is employed where only the intensity of light is modulated and not the phase. Next to the principle of DMT, Fig. 3.1 also shows how DMT can be applied in an optical IM/DD channel. Such an application of DMT is different from standard electrical systems, where a bipolar baseband signal is used. However, the intensity of the optical source can only have positive values. In IM/DD DMT systems, this problem is commonly solved by adding a DC-bias to the bipolar DMT signal to make it unipolar [29, 9, 21]. This is also shown in Fig. 3.1, where a DC-bias is added to the electrical (AC-coupled) DMT waveform before driving the laser or light-emitting diode of a short-range optical communication system. At the receiver, a simple (low-cost) photodetector is used to detect the intensity of the received light. This converts the DMT signal, which was modulated on the intensity, to an electrical signal which is then sampled by an analog-to-digital A/D converter for further digital processing.

Other techniques for DMT over IM/DD channels exist, without the need to add a DC-bias to the DMT signal. One such example is asymmetrically-clipped optical OFDM (ACO-OFDM), where the bipolar DMT waveform is clipped at the zero value and only the positive parts are transmitted [30]. Another related technique is pulse amplitude modulated DMT (PAM-DMT), which is discussed in Chapter 8. Such techniques, however, are currently still under investigation and have so far only

been proposed theoretically without practical proof of concept.

Therefore, the main method of DMT over optical IM/DD channels on which this thesis focuses will be the one with DC-bias, as depicted in Fig. 3.1. In [31, 29], this technique is also denoted as adaptively-modulated optical OFDM (AMOOFDM).

3.3 Cyclic Prefix and Dispersion

One important reason to use DMT (and OFDM) is the advantage to counter multipath delay spread, also known as dispersion, with the CP. In the case of optical OFDM transmission over single-mode fiber, the CP is used to deal with e.g. chromatic dispersion [32, 33, 34]. For DMT transmission over multimode fiber, the CP is used to counter the effects of modal dispersion [31, 25].

The resilience of DMT to dispersion in a transmission channel is the combined result of parallel transmission and cyclic prefix. Due to parallel transmission of the data with multiple subcarriers, the frame period of a DMT frame is much longer than the symbol period in the case of standard serial transmission. Therefore, inter-frame interference due to channel dispersion affects only a small fraction of a frame period. By employing a cyclic prefix, this interference can be easily eliminated and orthogonality among the subcarriers is always ensured [1].

3.3.1 Modal Dispersion in Multimode Fiber

In a multimode fiber (MMF), many different modes are excited and propagate through the fiber. These different modes traverse different paths in the MMF, leading to a total channel impulse response $h(t)$ which can be modeled as a summation of individual modes [1] given by

$$h(t) = \sum_{m=1}^{M} \gamma_m \, \delta\left(t - \tau_m\right) \tag{3.12}$$

where m is the mode index number, M is the total number of excited modes, γ_m is the attenuation value of the m-th mode, τ_m is the delay of the m-th mode, and $\delta(t)$ represents the Dirac impulse. Although (3.12) is commonly used to describe

---

[1]without taking mode-coupling and mode-mixing into account.

Figure 3.2: Modal (multipath) dispersion in a multimode fiber.
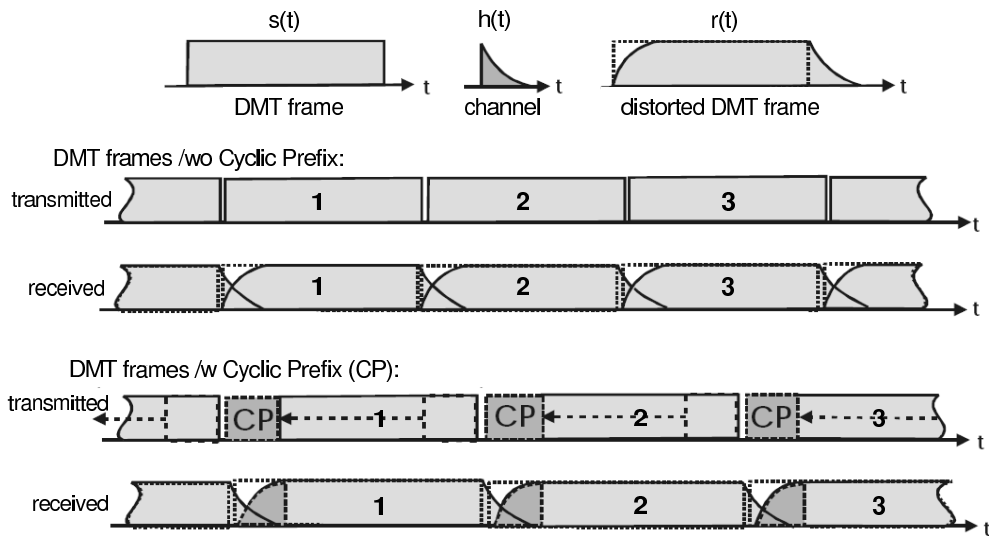
Figure 3.3: Using cyclic prefix to combat channel dispersion.

the effect of modal dispersion for electromagnetic fields in multimode optical fibers, it is used here to describe the power of the electromagnetic fields (of the optical signal) following square-law detection. This is valid because mode-coupling and mode-mixing are not considered in the model presented here, so that interference of electromagnetic fields after photodetection is not present. Due to this effect of modal dispersion, an ideal square pulse transmitted over the MMF will result in a dispersed waveform, as depicted by Fig. 3.2.

When a DMT frame $s(t)$ is transmitted, the received signal after propagation

over the MMF can be written as

$$r(t) = s(t) \otimes h(t) = \sum_{m=1}^{M} \gamma_m \, s \, (t - \tau_m) \ . \tag{3.13}$$

Without using CP, the first way to reduce the influence of modal dispersion is to increase the DMT frame period T as given in (3.6) for $N_{CP} = 0$, so that $T >> \max(\tau_m)$ where $\max(\tau_m)$ is the largest value of τ_m encountered in the multimode fiber. This is obvious from Fig. 3.3 because if the time period T of a DMT frame is far much longer than the maximum value of modal dispersion τ_m, the relative effect of inter-frame interference will be reduced to a minimum. The value of T can be increased by using a larger number of subcarriers N for transmission, as given in (3.6) when the sampling frequency f_s and therefore signal bandwidth and bit-rate are fixed.

However, observe from Fig. 3.3 that when no cyclic prefix is employed, even very small values of modal dispersion will cause some inter-frame interference when $r(t)$ is demodulated using (3.11), resulting in a performance degradation.

By inserting a cyclic prefix (see Fig. 3.3), inter-frame interference can be avoided. The time length of the cyclic prefix, given by $T_{CP} = N_{CP} \cdot \Delta t_s$ where N_{CP} is the number of cyclic prefix points per DMT frame and Δt_s is the D/A sampling period, should be chosen to be larger than the largest delay span or channel impulse response length $\max(\tau_m)$, of the multimode fiber. This leads to a DMT frame period length (including CP) of T as given in (3.6). Demodulation of $r(t)$ for $T_{CP} < t \leq T$ will lead to the same results as derived in (3.11).

3.3.2 Bandwidth Limitation and Dispersion

Next to modal dispersion in multimode fibers, bandwidth limitations of transmitter and receiver components in the frequency domain can also be regarded as dispersion in the time domain. This effect can be included in the fiber channel response as a low-pass filtering channel impulse response $h(t)$, so that the same methods mentioned previously to combat multimode dispersion can again be used to compensate for the effects of bandwidth-limited transceiver component. Therefore, DMT is also effective for reducing the effects of bandwidth limitations in an IM/DD channel.

3.4   Crest Factor

A DMT signal is basically the sum of a large number of subcarriers that are independently modulated. In multicarrier transmission systems such as OFDM and DMT, independently modulated subcarriers may incidentally add up constructively, leading to high peak amplitude values in the transmitted time signal [1]. When N subcarriers add up in phase, they may produce instantaneous peak amplitude values that are N times the average. Given a DMT time frame $s(t)$, which was derived in (3.7), the crest factor, is written as

$$\mu = \frac{s_{peak}}{s_{rms}} \tag{3.14}$$

where s_{peak} is the peak signal amplitude and s_{rms} is the effective or root-mean-square (rms) amplitude of $s(t)$ given by

$$s_{rms} = \sqrt{\langle s^2(t)\rangle} \tag{3.15}$$

and $\langle s^2(t)\rangle$ denotes the mean power of $s(t)$, averaged over a large number of DMT frames.

Although clipping is a straightforward and easy way to limit the crest factor of a DMT signal, it introduces distortion to the signal and as a result can lead to a degradation in performance. However, when applied moderately and properly, it is shown in 4.3 that a certain amount of clipping can improve performance in an IM/DD channel.

Next to clipping, various other methods have been proposed to reduce the crest factor of DMT signals without introducing any distortion to the signal. Some of the most well-known and popular methods include for instance selective mapping [35, 36, 37] where different QAM constellation mapping schemes containing the same information can be chosen depending on the resulting crest factor, partial transmit sequence [38, 39] where selective mapping is applied to a few groups of multiple subcarriers for less computational complexity, modified signal constellations [40, 41], and algebraic coding [42]. Although such distortion-less crest factor reduction techniques can theoretically reduce the crest factor of a DMT system to very low values, the complexity of such methods is often too high for practical implementation. Therefore, distortion-less crest factor reduction techniques are nowadays mostly limited to theoretical investigation.

3.5 Synchronization

Synchronization is an important issue in DMT transmission systems. Without synchronization, the receiver will not be able to distinguish between different DMT frames, leading to erroneous demodulation of the received sequence. Although numerous timing and synchronization schemes have been proposed and used for both OFDM and DMT [43, 44, 45, 46], this thesis will limit the scope to what has been used in the experiments presented in Chapters 4, 5, 6 and 7.

Basically, two different methods for synchronization are used. First, the cyclic prefix of every DMT frame is used for quickly finding the start of a DMT frame. With this method, the cyclic prefix is correlated with its delayed version at the end of a DMT frame [47], resulting in

$$x(t) = \int_0^{T_{CP}} r(\tau)\, r(t - \tau - T)\, d\tau \tag{3.16}$$

where $x(t)$ is the output of the correlator, $r(t)$ is the received DMT frame, T_{CP} is the time duration of the cyclic prefix, and T is the time period of a DMT frame. When the frame timing is correct, the cyclic prefix will correlate with the delayed version of itself and a large correlation value $x(t)$ is achieved, indicating the start of a frame.

However, as a result of convolution with the channel impulse response, the CP value of a received DMT frame $r(t)$ for $0 \le t < T_{CP}$ is not exactly the same as its delayed version in the frame for $T - T_{CP} \le t < T$. This results in a lower correlation value $x(t)$ from (3.16), where proper detection depends on the SNR of the received DMT signal. For better synchronization performance, one can increase T_{CP} to larger values for better correlation results.

After the start of a DMT frame is found through the cyclic prefix, synchronization between the DMT transmitter and receiver sampling clocks is performed. This is done in the digital domain on the received data by tracking (in a decision-directed manner) the phase of each subcarrier after the FFT operation and correcting this for every DMT frame. Inter-carrier interference resulting from sampling frequency offset is not corrected. Note that the method described here is the one used for the experiments in this thesis, which is only one of many different possible methods for clock synchronization.

3.6 Bit-Loading

An important feature of DMT is the possibility to allocate the number of bits per subcarrier according to its corresponding signal-to-noise ratio (SNR), typically known as bit-loading. This is accomplished by selecting the corresponding QAM constellation size of each subcarrier according to the number of bits that are allocated to it. Bit-loading can be divided into two categories: rate-adaptive and margin-adaptive. Rate-adaptive algorithms maximize the bit rate for a fixed bit-error ratio (BER) and given power constraint, while margin-adaptive algorithms minimize the BER for a fixed bit rate.

In practical systems, bit-loading is often used in wireline communications such as DSL. This is because wireline transmission channels do not vary significantly with time, resulting in a large performance gain at relatively low complexity because such bit-loading algorithms only have to be computed during setup of a transmission link and not updated continuously. Until now, only rate-adaptive bit-loading has found widespread use in commercial systems. The main advantage of rate-adaptive bit-loading is that no matter how bad the transmission channel is, data transmission (even at very low bit-rates) is always possible. In this thesis, only rate-adaptive bit-loading will be discussed and considered, due to its use for maximizing achievable bit-rates.

The rate-adaptive bit-loading algorithm is a reformulation of the Shannon capacity formula and can be expressed as a problem of maximizing the total achievable bit-rate R in bit/s, which is the sum of the allocated bits per subcarrier b_n used for DMT transmission given by [4, 48]

$$\max_{P_n}(R) = \max_{P_n} \left(\frac{1}{N} \sum_{n=0}^{N-1} b_n \right) \cdot B \tag{3.17a}$$

$$= \max_{P_n} \left[\frac{1}{N} \sum_{n=0}^{N-1} \log_2 \left(1 + \frac{\text{SNR}_n}{\Gamma} \right) \right] \cdot B \tag{3.17b}$$

$$= \max_{P_n} \left[\frac{1}{N} \sum_{n=0}^{N-1} \log_2 \left(1 + \frac{P_n \cdot g_n}{\Gamma} \right) \right] \cdot B \tag{3.17c}$$

where B is the bandwidth of the signal, n is the subcarrier index, N is the total number of available subcarriers, $\text{SNR}_n = P_n \cdot g_n$ is the SNR per subcarrier, g_n

represents the subcarrier SNR when unit power is applied, Γ is the difference (gap) between the SNR needed to achieve maximum (Shannon) capacity and the SNR to achieve this capacity at a given bit error probability, and P_n is the allocated power per subcarrier, subject to a power constraint given by

$$\sum_{n=1}^{N-1} P_n = P_{tot} \ . \tag{3.18}$$

P_{tot} is the fixed total available power for transmission. The problem is now to find the optimum distribution of b_n, for $n = 0, 1, \ldots, N$, and the corresponding power distribution per subchannel P_n, in order to maximize the system bit-rate. Note that maximum bit-rate is not always achieved when all N subchannels are allocated with information bits, so that b_n and P_n can be 0 for some particular n. Therefore, the optimal solution is not always to use all available subchannels to transmit information, but to use only the ones with the highest SNR.

The solution to this bit-rate maximization problem, which is similar to the one that is presented in Chapter 4.2.1, is based on the use of Lagrange multipliers and is given by [4, 49]

$$P_n + \frac{\Gamma}{g_n} = \text{constant} \ , \tag{3.19}$$

which is commonly known as water-filling. This equation states that the solution that maximizes bit-rate, under the constraint of (3.18), is the one where all the subcarriers that are used to transmit information have a constant level $P_n + \frac{\Gamma}{g_n}$. Simply stated, the optimum solution is to distribute the total available transmission power P_{tot} to the subcarriers with the highest channel SNR represented by $\frac{g_n}{\Gamma}$, just like filling a bathtub with water where water flows into the deepest point first.

Numerical computation of this water-filling algorithm is possible and leads to the optimum solution which, however, allocates non-integer number of bits to each subcarrier. This is not suitable for practical realization, so that alternative loading algorithms resulting in bit-allocation with finite bit granularity should be considered.

In [48], Chow proposed a numerical bit-loading algorithm that results in the allocation of bits with finite granularity. This algorithm, based on an approximation of the water-filling solution given by (3.19), initially decides which subcarriers to use by discarding the subcarriers with the lowest SNR for information transmission, and redistributes the power to subcarriers with a higher SNR in order to support higher

data rates. The non-integer number of allocated bits per subcarrier are then rounded (both up- and downwards) to the nearest integer and the corresponding power is adapted (both upwards and downwards) to support the newly-allocated number of bits at the same BER performance. Due to the approximation of the water-filling solution, Chow's algorithm does not achieve optimum performance but has been shown to achieve near-optimum performance [4, 48].

In the subsequent chapters of this thesis, Chow's algorithm will be used to compute rate-adaptive bit-loading for the DMT measurements. For more details on the implementation of this algorithm, the reader is referred to [4] and [48].

CHAPTER 4
CHANNEL CAPACITY

Due to costs reasons, short-range optical communication systems mainly employ intensity-modulation and direct-detection. Such systems do not need such high levels of performance like long-haul single-mode fiber systems because of the much shorter reach. Moreover, due to its enormous market volume and low sharing factor, it is essential that the cost level of short-range optical communication systems is lowered to the bare minimum. It is therefore most straightforward and easy to modulate the intensity of an optical source such as an LED or a laser diode just by modulating its driving current. Consequently, at the receiver side, only the intensity of the received optical signal needs to be detected. A simple photodiode is enough to detect this intensity, making an IM/DD optical communication system the cheapest system for transmitting information by optical means.

However, such a cost advantage also comes at the expense of lower performance as a result of lower bandwidth, leading to lower transmission bit-rates than achievable by single-mode fiber systems. It is therefore of interest to be able to characterize a short-range optical communication system using several key parameters and estimate the maximum achievable transmission rates using these parameters.

In this chapter, theoretical investigations of the Shannon capacity of a general optical IM/DD channel are performed. An analytical IM/DD channel model is derived and capacity calculations are made based on this model for two common low-pass frequency channel responses: the Gaussian and the first-order low-pass.

These two channel responses are chosen because they approximate the response of an optical IM/DD channel well. Additionally, the influence of DMT on the ideal channel capacity is analyzed and the concept of bit-loading is introduced and it is shown how it is used to maximize the achievable capacity with DMT.

4.1   The IM/DD Channel Model

Before analyzing the capacity of an optical IM/DD system, a general model for the transmitter, channel, and receiver should first be considered. Fig. 4.1 shows a block diagram of such an IM/DD channel model which will be used in the further analysis.
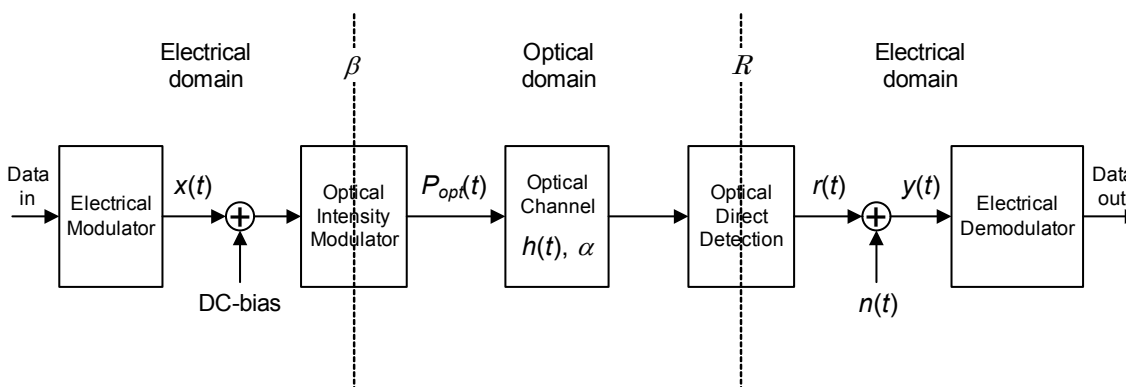
Figure 4.1: The optical IM/DD channel model.

First, an electrical modulator is used to modulate the incoming data into the appropriate modulation format, which for example can be baseband (such as amplitude shift keying), consisting of a single subcarrier (modulated with phase shift keying or QAM), or multiple subcarriers such as DMT. This results in a transmitted electrical current $x(t)$, which is used to drive an optical intensity-modulated source such as an LED or a laser diode. Note that $x(t)$ is considered to be an alternating current (AC) coupled, bipolar signal, so that its mean value $\langle x(t) \rangle = 0$. Due to the fact that only the intensity of light is modulated and detected in an IM/DD channel, a unipolar modulated signal is needed to drive the optical intensity of the light source. This is achieved by adding a DC bias to $x(t)$.

Fig. 4.2 shows a model of an ideal linear optical intensity modulator, which will

Output Power

P_{opt}

$I(t)$

Input Current

0

I_{th}

I_{bias}

$x(t)$
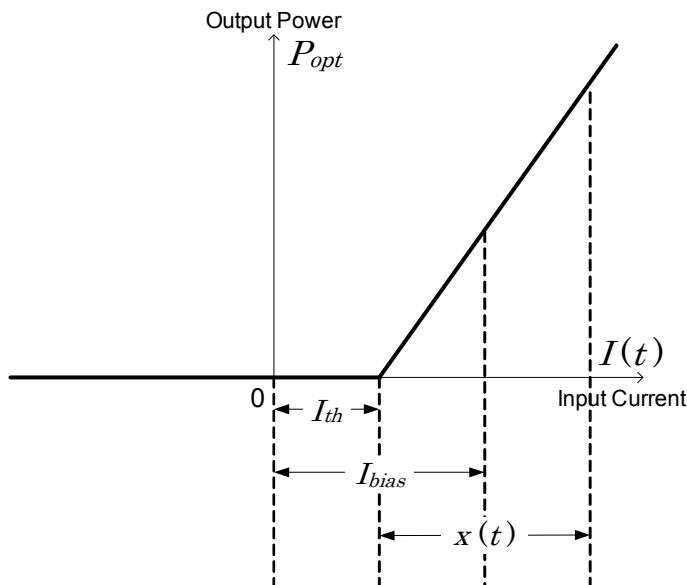
Figure 4.2: Ideal intensity modulator model.

be used for the analysis. Using this model, it is assumed that no optical power is emitted when the driving current is below the threshold value of I_{th}, and the optical power emission is linearly proportional to the driving current when this current is above I_{th}. Moreover, there is no saturation effect for infinite values of the driving current.

Because $\langle x(t) \rangle = 0$, it is most efficient to set the DC bias current I_{bias} to a value

$$I_{bias} = I_{th} + x_{peak} \tag{4.1}$$

where x_{peak} represents the peak amplitude of $x(t)$ and all values are given in the unit A. Although I_{th} is depicted in Fig. 4.2 with a non-zero value, it will, for convenience, be assumed to be 0 in the following analysis. The resulting instantaneous transmitted optical power $P_{opt}(t)$ in W_o can then be written as a function of its driving current

$$
\begin{aligned}
P_{opt}(t) &= \beta \left[I_{bias} + x(t) \right] \\
&= \beta \left[x_{peak} + x(t) \right] \\
&= \beta \left[\mu \sqrt{\langle x^2(t) \rangle} + x(t) \right] \\
&= \beta \left[\mu x_{rms} + x(t) \right]
\end{aligned}
\tag{4.2}
$$

where β is the quantum efficiency of the electrical current-to-optical power conversion given in W_o/A and x_{rms} is the rms amplitude of $x(t)$ given by

$$x_{rms} = \sqrt{\langle x^2(t) \rangle} \tag{4.3}$$

and $\langle x^2(t) \rangle$ denotes the mean electrical signal power of $x(t)$. μ is the peak-to-rms factor of $x(t)$, which is commonly known as the crest factor

$$\mu = \frac{x_{peak}}{x_{rms}} \ . \tag{4.4}$$

Note that the crest factor μ is always ≥ 1. As $x(t)$ is a generic zero-mean signal, the mean transmitted optical power P_{mean} depends on the crest factor μ of $x(t)$ given by

$$P_{mean} = \langle P_{opt}(t) \rangle = \beta \mu x_{rms} = \beta x_{peak} \ . \tag{4.5}$$

After transmission over the channel, the optical signal is detected by a receiver which is assumed to consist of a photodiode and a trans-impedance amplifier. The received electrical signal from the photodetector $y(t)$ in V, which is assumed to be passed through a DC-block, can be written as

$$y(t) = r(t) + n(t) \tag{4.6}$$

where $r(t)$ is the noiseless received electrical signal from the photodetector and $n(t)$ is additive white Gaussian noise (AWGN) which represents the thermal noise resulting from the trans-impedance amplifier in the receiver. Because $y(t)$ is assumed to be passed through a DC-block, the noiseless received electrical signal $r(t)$ is AC-coupled (i.e. its DC component is removed), resulting in

$$r(t) = R \cdot G \cdot \alpha \cdot [P_{opt}(t) - P_{mean}] \otimes h(t) \tag{4.7a}$$
$$= R \cdot G \cdot \alpha \cdot \beta x(t) \otimes h(t) \tag{4.7b}$$

where R is the responsivity of the photodiode in A/W_o, G is the trans-impedance gain of the photodetector in V/A, α is the channel attenuation and $\otimes$ denotes the linear convolution between the modulated part of the transmitted optical power $\beta x(t)$ and $h(t)$. $h(t)$ represents the normalized, optical intensity fiber channel impulse response.

4.2 The IM/DD Channel Capacity

As described previously, bandwidth is often the limiting factor for achieving higher transmission data rates in an optical IM/DD channel. Such bandwidth limitations can either originate from the transmitter, channel, receiver, or combinations of the aforementioned. Using the channel model derived in Section 4.1, the Shannon capacity of a general bandwidth-limited optical IM/DD channel will be analyzed in this section by making use of the well-known water-filling method as described in [50, 49, 4]. The idea for this IM/DD channel analysis has first been presented by Gaudino et al. for the SI-POF channel in [51], which forms the basis of the first part given by Section 4.2.1. The rest of the analysis is based on the results shown in [9], which is further elaborated in this thesis. The main results are achieved by reviewing the theory for the evaluation of the channel capacity for the general case of a receiver characterized by additive white Gaussian noise (AWGN) with power spectral density $G_n(f)$, and a relevant received signal with power spectral density $G_s(f)$. $G_s(f)$ is influenced by the bandwidth-limiting response of the entire transmission system (transmitter, receiver, and channel), which, for convenience, will be denoted as the channel response $H(f)$ in the rest of this thesis. In particular, two common types of optical IM/DD channel responses will be considered for analysis of the Shannon capacity: the Gaussian low-pass and the first-order low-pass.

4.2.1 Gaussian Low-Pass Channel Response

An example of an IM/DD optical channel is the SI-POF channel, which, according to measurement results given in [52], can be modeled as a Gaussian low-pass filter. Its frequency response can thus be expressed as

$$H(f) = e^{-\frac{1}{2}\left(\frac{f}{f_0}\right)^2}, \quad \text{with } f_0 = f_{3dB}/\sqrt{\ln(2)} \tag{4.8}$$

where f_{3dB} is the -3dB bandwidth of the full electrical-optical-electrical channel given in Hz. At the receiver side, the only noise source in the system that is taken into account is additive white Gaussian noise, which represents the noise introduced by the trans-impedance amplifier in the photodetector.

By treating this channel as a sum of infinitesimal subchannels and following the advanced but well-known results from information theory [50, 49], the resulting

31
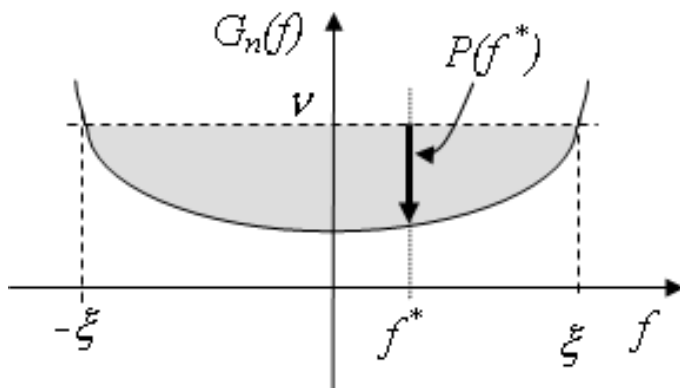
Figure 4.3: Water-filling for optical IM/DD channel.

capacity C in bits/s is given by maximizing the quantity

$$C \leq \int_{-\infty}^{+\infty} \frac{1}{2} \log_2 \left[1 + \frac{G_s(f)}{G_n(f)} \right] df \qquad (4.9)$$

under the constraint

$$P_s = \int_{-\infty}^{+\infty} G_s(f) \, df . \qquad (4.10)$$

The unknown in this problem is the "signal spectral distribution" $G_s(f)$ that solves this optimization problem. The solution, based on Lagrange multipliers, is given in [50, 49] and can be expressed by

$$G_s(f) = (\nu - G_n(f))^+ \qquad (4.11)$$

where ν is an unknown constant value to be chosen so that

$$\int_{-\infty}^{+\infty} (\nu - G_n(f))^+ \, df = P_s \qquad (4.12)$$

and $(\cdot)^+$ is the functional giving the positive part of its argument, i.e.

$$(z)^+ = \begin{cases} z & \text{if } z \geq 0 \\ 0 & \text{if } z < 0 \end{cases} \qquad (4.13)$$

This method is known in literature as water-filling [50], and has an intuitive explanation given in Fig. 4.3. For a given $G_n(f)$, finding ν in (4.11) means finding the "level" ν so that the area of the gray region in the figure is exactly equal to P_s. The meaning of the resulting optimal $G_s(f)$ is indicated in the figure using a thick

arrow. Intuitively, the solution allocates most of the power in the frequency range where the noise is least. In particular, no power is allocated outside the "critical frequency" ξ, which satisfies the equation $G_n(\xi) = \nu$. This parameter ξ will play a key role in the following calculations regarding the Shannon capacity.

By combining (4.9) and (4.10) with the general result given by (4.11) and (4.12), the capacity of the SI-POF channel can be calculated. The noiseless AC-coupled received signal $r(t)$ after photodetection, as derived in (4.7), has a power spectral density in V^2/Hz given by

$$G_r(f) = R^2\, G^2\, \alpha^2 \cdot |H(f)|^2 \cdot \beta^2 G_x(f) \tag{4.14}$$

where $\beta^2 G_x(f)$ is the power spectral density of the modulated part of the transmitted optical power, which is proportional to the modulating current $x(t)$. By considering flat receiver noise with power spectral density $N_0/2$ and using (4.9), the capacity of the POF channel can be written as

$$C \le \int_{-\infty}^{+\infty} \frac{1}{2} \log_2 \left[1 + \frac{R^2\, G^2\, \alpha^2 \cdot \beta^2 G_x(f) \cdot |H(f)|^2}{N_0/2} \right]\, df \tag{4.15}$$

with bound given by (4.18). Equation (4.15) can be further simplified to

$$C \le \int_{-\infty}^{+\infty} \frac{1}{2} \log_2 \left[1 + \frac{2\alpha^2 \cdot \beta^2 G_x(f) \cdot |H(f)|^2}{\text{NEP}^2} \right]\, df \tag{4.16}$$

with NEP defined as the noise equivalent power in $\text{W}_\text{o}/\sqrt{\text{Hz}}$. NEP is a commonly-used figure of merit to characterize the noise performance of photodetectors. The general optimization problem given by (4.9) and (4.10) can now be re-formulated for the optical IM/DD channel if we set

$$G_s(f) = \beta^2 G_x(f) \tag{4.17a}$$

$$G_n(f) = \frac{\text{NEP}^2}{2\alpha^2} \cdot e^{\left(\frac{f}{f_0}\right)^2} \tag{4.17b}$$

with $H(f)$ as given in (4.8). The power spectral density $G_x(f)$ of the modulating current $x(t)$ is now the unknown in the optimization problem and must satisfy the

power constraint set by (4.10), re-written as

$$\int_{-\infty}^{+\infty} \beta^2 G_x(f) df = \beta^2 \left\langle x^2(t) \right\rangle$$
$$= \beta^2 x_{rms}^2 \qquad (4.18)$$
$$= \left(\frac{P_{mean}}{\mu}\right)^2$$

with $P_s = \left(\frac{P_{mean}}{\mu}\right)^2$. Using the water-filling solution given by (4.11) and (4.12), and by explicitly inserting the parameter ξ, the problem is re-written as

$$\int_{-\xi}^{+\xi} \left(\nu - G_n(f)\right)^+ df = P_s \qquad (4.19)$$

with

$$\nu = G_n(\xi) = \frac{\text{NEP}^2}{2\alpha^2} \cdot e^{\left(\frac{\xi}{f_0}\right)^2} \qquad (4.20)$$

which can finally be formulated as [1]

$$\frac{\text{NEP}^2}{2\alpha^2} \int_{-\xi}^{+\xi} \left[e^{\left(\frac{\xi}{f_0}\right)^2} - e^{\left(\frac{f}{f_0}\right)^2} \right] df = \left(\frac{P_{mean}}{\mu}\right)^2 . \qquad (4.21)$$

This turns out to be a nonlinear problem in the unknown ξ which can be solved numerically. After some algebraic passages shown in Appendix A.1, the following results arise

1. By introducing a new normalized parameter $\eta = \xi/f_0$, this parameter depends only on

$$\text{SNR}_{\text{norm}} = \frac{\alpha^2 \cdot P_{mean}^2}{\text{NEP}^2 \cdot f_0 \cdot \mu^2} \qquad (4.22)$$

through a nonlinear law $\eta = g(\text{SNR}_{\text{norm}})$ that can be easily computed numerically. SNR_{norm} represents the normalized signal-to-noise ratio after photodetection.

2. The resulting capacity has a closed-form expression in η, given by

$$C = \frac{2}{3\ln(2)\sqrt{\ln(2)}} f_{3dB} \, \eta^3 . \qquad (4.23)$$

---

[1] note that $\int_{-\xi}^{+\xi} e^{\left(\frac{f}{f_0}\right)^2} df$ does not result in the error function, which is $\frac{f_0}{\sqrt{\pi}} \int_{-\xi}^{+\xi} e^{-\left(\frac{f}{f_0}\right)^2} df$.

In conclusion, the capacity of the SI-POF channel can be calculated by

$$C = \frac{2}{3\ln(2)\sqrt{\ln(2)}} f_{3dB} \cdot g^3(\text{SNR}_{\text{norm}}) \tag{4.24}$$

which depends on the -3dB bandwidth f_{3dB} of the (Gaussian low-pass) channel and the normalized signal-to-noise ratio SNR_{norm} given in (4.22). Fig. 4.4 gives a general curve for (4.24) by plotting C/f_{3dB} as a function of SNR_{norm}. From this curve, it can be seen that for a system with for example $\text{SNR}_{\text{norm}} = 20$ dB, the resulting C/f_{3dB} is approximately 10. This means that the channel capacity C in [bit/s] is 10 times larger than its -3dB bandwidth f_{3dB}.
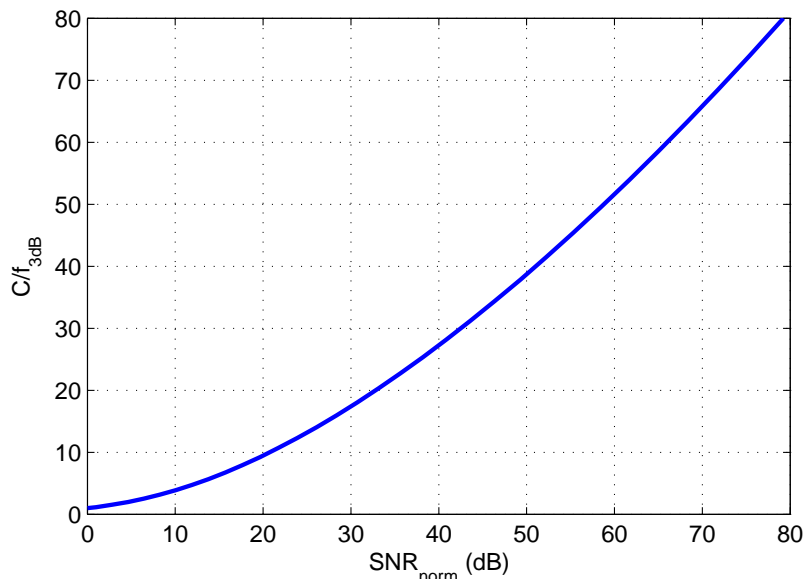
Figure 4.4: Normalized capacity C/f_{3dB} vs. SNR_{norm} for Gaussian low-pass channel.

4.2.2 First-Order Low-Pass Channel Response

For a first-order low-pass optical IM/DD channel, the frequency response can be expressed as

$$H(f) = \frac{1}{\sqrt{1 + \left(\frac{f}{f_0}\right)^2}}, \quad \text{with } f_0 = f_{3dB} \tag{4.25}$$

where f_{3dB} is the -3dB bandwidth of the full electrical-optical-electrical channel. Similar to the case in Section 4.2.1, the starting point for calculating the Shannon

capacity is given by (4.9)

$$C \leq \int_{-\infty}^{+\infty} \frac{1}{2} \log_2 \left[1 + \frac{G_s(f)}{G_n(f)} \right] df$$

which again can be written as in (4.16)

$$C \leq \int_{-\infty}^{+\infty} \frac{1}{2} \log_2 \left[1 + \frac{2\alpha^2 \cdot \beta^2 G_x(f) \cdot |H(f)|^2}{\text{NEP}^2} \right] df$$

where the difference here with (4.17) is that

$$G_s(f) = \beta^2 G_x(f) \tag{4.26a}$$

$$G_n(f) = \frac{\text{NEP}^2}{2\alpha^2} \cdot \left[1 + \left(\frac{f}{f_0} \right)^2 \right] \tag{4.26b}$$

due to a different channel response $|H(f)|^2$ given by (4.25). Analogous to (4.21), the resulting equation to solve is now given by

$$\frac{\text{NEP}^2}{2\alpha^2} \int_{-\xi}^{+\xi} \left[\left(\frac{\xi}{f_0} \right)^2 - \left(\frac{f}{f_0} \right)^2 \right] df = \left(\frac{P_{mean}}{\mu} \right)^2 \tag{4.27}$$

which leads a closed-form expression for the capacity of a first-order low-pass optical IM/DD channel

$$C = f_0 \frac{2}{\ln(2)} \left(\sqrt[3]{\frac{3}{2} \text{SNR}_{\text{norm}}} - \arctan \sqrt[3]{\frac{3}{2} \text{SNR}_{\text{norm}}} \right) \tag{4.28}$$

where the normalized signal-to-noise ratio SNR_{norm} is defined as in (4.22). Details regarding the mathematical passages to arrive at (4.28) are shown in Appendix A.2.

For a first-order low-pass channel response, f_0 is equal to f_{3dB}. Therefore, (4.28) can also be written as

$$C = f_{3dB} \frac{2}{\ln(2)} \left(\sqrt[3]{\frac{3}{2} \text{SNR}_{\text{norm}}} - \arctan \sqrt[3]{\frac{3}{2} \text{SNR}_{\text{norm}}} \right) . \tag{4.29}$$

Fig. 4.5 depicts the normalized capacity C/f_{3dB} as a function of SNR_{norm} for a first-order low-pass optical IM/DD channel. The curve for Gaussian low-pass channel response (already shown in Fig. 4.4) is also plotted in the same figure for comparison. It is obvious that the first-order low-pass channel response has a larger capacity than the Gaussian low-pass. For large values of SNR_{norm}, this difference gets significantly larger.
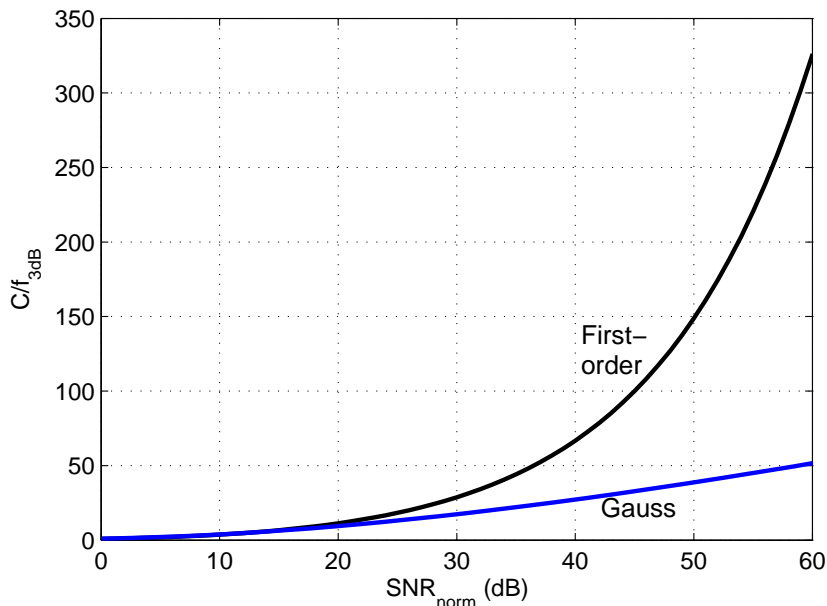
Figure 4.5: Normalized capacity C/f_{3dB} vs. SNR_{norm} for first-order and Gaussian low-pass optical IM/DD channel response.

4.2.3 Crest Factor

In the previous subsections 4.2.1 and 4.2.2, the general optical IM/DD channel capacity was theoretically analyzed for respectively a Gaussian and a first-order low-pass channel response corrupted with AWGN. Basically, three main expressions were derived for calculating the capacity given by the normalized SNR in (4.22)

$$\text{SNR}_{\text{norm}} = \frac{\alpha^2 \cdot P_{mean}^2}{\text{NEP}^2 \cdot f_0 \cdot \mu^2}$$

the capacity for the Gaussian low-pass response in (4.24)

$$C = \frac{2}{3\ln(2)\sqrt{\ln(2)}} f_{3dB} \cdot g^3(\text{SNR}_{\text{norm}})$$

and the capacity for the first-order low-pass response in (4.29)

$$C = f_{3dB} \frac{2}{\ln(2)} \left(\sqrt[3]{\tfrac{3}{2}\text{SNR}_{\text{norm}}} - \arctan \sqrt[3]{\tfrac{3}{2}\text{SNR}_{\text{norm}}} \right) \ .$$

By using these expressions, the capacity of an optical IM/DD channel can be separated into two parts, namely a noise-dependent part given by (4.22) and a channel-response-dependent part given by (4.24) and (4.29).

In particular, for a given fixed channel response, the capacity can be optimized by optimizing SNR_{norm}. Other than the channel attenuation α and its bandwidth f_0, the mean transmitted optical power P_{mean}, and the photodetector noise given by its NEP, notice from (4.22) that the crest factor μ of the transmitted signal $x(t)$, given in (4.4) as

$$\mu = \frac{x_{peak}}{x_{rms}}$$

also plays an important role in defining the channel capacity. In order to achieve the highest capacity in an optical IM/DD channel, μ should be kept as close as possible to the minimum value of 1.

It is interesting to observe that, based on the analysis presented here, the modulation format with $\mu = 1$ will achieve the largest normalized SNR and result in the highest capacity value possible in an optical IM/DD channel. This implies that standard on-off-keying modulation using rectangular pulses resulting in $\mu = 1$ will theoretically achieve the highest capacity in an optical IM/DD channel. However, note that this is only true under the assumption that transmission over the channel does not cause inter-symbol interference in the pulses. Therefore, for this statement to be valid, it is required that the channel impulse response is ideally equalized, which is often impossible in practical realization.

4.3 Influence of DMT on Channel Capacity

In this section, the IM/DD channel capacity calculation is revised for the case when DMT is used as the modulation format. For a large number of subcarriers (>10), a DMT time signal $x(t)$ can be modeled as a zero-mean, Gaussian-distributed process with variance σ_x^2 as in [53, 5, 54]. In order to efficiently transmit the DMT signal over an optical IM/DD channel, the signal has first to be limited in amplitude [29, 25, 9]. A common and straightforward method to realize this is by clipping the time-discrete DMT waveform in the digital domain before D/A conversion, resulting in a clipped electrical DMT signal $\hat{x}(t)$ after D/A conversion

$$\hat{x}(t) = \begin{cases} x(t) & \text{for } |x(t)| \leq A_{clip} \\ A_{clip} & \text{for } |x(t)| > A_{clip} \end{cases} \tag{4.30}$$

Figure 4.6: Instantaneous amplitude $x(t)$ of a DMT symbol and its associated Gaussian-distributed probability density function

where A_{clip} is the maximum allowed amplitude level and $x(t)$ is the DMT signal without clipping. The modulated signal to be transmitted is now given by $\hat{x}(t)$ and its clipping-limited crest factor μ defined in (4.4) depends now on the amount of clipping as

$$\mu = \frac{x_{peak}}{x_{rms}} = \frac{A_{clip}}{\sqrt{\langle x^2(t)\rangle}} \tag{4.31}$$

where $\langle x^2(t)\rangle$ denotes the mean power of the DMT time signal $x(t)$ without clipping. Typical values for μ lie in the range of 2.5 to 3.5 as given in [29, 25, 26]. After clipping, a DC bias is added to the electrical DMT signal $\hat{x}(t)$ for driving the optical intensity modulator so that (4.2) is rewritten as

$$P_{opt}(t) = \beta \left[\mu x_{rms} + \hat{x}(t) \right] . \tag{4.32}$$

Although clipping can improve the system performance by minimizing μ, it how-ever also introduces additional noise-like distortion into the system, thereby degrad-ing performance. While the general channel capacity analysis in Section 4.2 only considered AWGN resulting from the photodetector, this section will include clipping noise into the capacity analysis as a result of the use of DMT. Additionally, DMT requires the use of D/A and A/D converters so that the influence of quantization noise is also considered.

4.3.1 Clipping Noise

A DMT modulated signal is basically the sum of a large number of subcarriers that are independently QAM modulated. As shown in [53] and [5, 54], such a DMT signal can be approximated with a zero-mean Gaussian-distributed process with variance $\sigma_x^2 = \langle x^2(t) \rangle$ as depicted in Fig. 4.6. From the figure, it can be seen that the instantaneous amplitude $x(t)$ spans a large range with a maximum value that arises when a large number of modulated subcarriers incidentally add in-phase.

Since the maximum instantaneous amplitude occurs very rarely due to statistical averaging, it can be advantageous to clip the signal to a certain value A_{clip} to trade-off the resulting clipping noise against the gain with regard to photodetector thermal noise due to a smaller μ (see equation (4.22)) as shown in [29, 25, 26]. Using this Gaussian-distribution model, the noise power resulting from symmetrical clipping of a bipolar DMT signal to $-A_{clip}$ and A_{clip} according to (4.30) can easily be expressed by

$$P_{clip} = 2 \cdot \int_{A_{clip}}^{+\infty} \left(z^2 - A_{clip}^2 \right) \cdot p(z)\, dz \tag{4.33}$$

with the probability density function

$$p(z) = \mathrm{prob}\, \{x(t) = z\} = \frac{1}{\sigma_x \sqrt{2\pi}} \exp\left(-\frac{z^2}{2\sigma_x^2} \right) . \tag{4.34}$$

Solving (4.33) leads to

$$
\begin{aligned}
P_{clip} &= \frac{2}{\sigma_x \sqrt{2\pi}} \int_{A_{clip}}^{+\infty} \left(z^2 - A_{clip}^2 \right) \exp\left(-\frac{z^2}{2\sigma_x^2} \right) dz \\
&= \left[\left(\sigma_x^2 - A_{clip}^2 \right) \mathrm{erf}\left(\frac{z}{\sqrt{2}\sigma_x} \right) - \sigma_x z \sqrt{\frac{2}{\pi}} \exp\left(-\frac{z^2}{2\sigma_x^2} \right) \right]_{A_{clip}}^{+\infty} \\
&= \sigma_x^2 \left[\left(1 - \mu^2 \right) \mathrm{erfc}\left(\frac{\mu}{\sqrt{2}} \right) + \mu \sqrt{\frac{2}{\pi}} \exp\left(-\frac{\mu^2}{2} \right) \right]
\end{aligned}
\tag{4.35}
$$

where μ is the clipping-limited crest factor given by $\mu = A_{clip}/\sigma_x$, σ_x^2 is the mean DMT signal power before clipping, and $\mathrm{erf}(\cdot)$ and $\mathrm{erfc}(\cdot)$ denote respectively the error-function and the complementary error-function. Note that (4.35) is different from the results derived in [54], due to a different approach of calculation.

Because of the many independently modulated subcarriers and incidental occurrence of large peaks, clipping can be approximated by a random process and therefore clipping noise can be assumed to be white. Additionally, due to the use of D/A converters with finite dynamic range and quantization, clipping is performed digitally before D/A conversion. Assuming that no digital oversampling is used, the clipping noise bandwidth is equal to the signal bandwidth so that the signal-to-clipping noise power ratio is written as

$$
\begin{aligned}
\text{SNR}_{\text{clip}} &= \frac{\sigma_x^2 - P_{clip}}{P_{clip}} \\
&= \left[(1 - \mu^2) \, \text{erfc} \left(\frac{\mu}{\sqrt{2}} \right) + \mu \sqrt{\frac{2}{\pi}} \exp \left(-\frac{\mu^2}{2} \right) \right]^{-1} - 1 \, .
\end{aligned}
\tag{4.36}
$$

In order to calculate the capacity of a DMT signal over an IM/DD channel, (4.22) should be re-formulated to include the effect of clipping. From (4.22), SNR_{norm} can be re-written to consist of an electrical photodetector (white) thermal noise power part P_{therm} and a received electrical signal power part P_{sig} as

$$
\begin{aligned}
\text{SNR}_{\text{norm}} &= \frac{1}{\text{NEP}^2 \cdot f_0} \cdot \frac{\alpha^2 P_{mean}^2}{\mu^2} \\
&= \frac{1}{P_{therm}} \cdot P_{sig}
\end{aligned}
\tag{4.37}
$$

where

$$
P_{therm} = \text{NEP}^2 \cdot f_0
\tag{4.38}
$$

and

$$
P_{sig} = \frac{\alpha^2 P_{mean}^2}{\mu^2} \, .
\tag{4.39}
$$

By adding the influence of clipping and setting $\sigma_x^2 = P_{sig}$, (4.37) becomes

$$
\text{SNR}_{\text{norm}} = \frac{\hat{P}_{sig}}{P_{therm} + P_{clip}}
\tag{4.40}
$$

where P_{therm} is given in (4.38), P_{clip} is given in (4.35), and $\hat{P}_{sig}$ is the received electrical DMT signal power after clipping given by

$$
\hat{P}_{sig} = P_{sig} - P_{clip} \, .
\tag{4.41}
$$

Figure 4.7: SNR_{norm} as a function of crest factor μ after clipping. Lines depict analytical results and circles depict Monte-Carlo simulation results.

In Fig. 4.7, the analytical expressions for SNR_{norm} with and without taking clipping noise into account are plotted as a function of the (clipping-limited) crest factor μ using the parameters given in Table 4.1. The dashed line depicts the curve of $\hat{P}_{sig}/P_{therm}$, indicating that clipping also reduces the useful DMT signal power, leading to lower SNR values when compared to the values given by (4.37). Furthermore, Monte-Carlo simulation results using a 256-subcarrier DMT system are plotted in the same figure to compare the accuracy of the analytical model. A difference can clearly be observed between the analytical and simulation results for large values of clipping (low crest factor values). However, by use of a correction

Table 4.1: Parameters used for results in Fig. 4.7 and 4.8.

Parameter	Value	[Units]
$\alpha \cdot P_{mean}$	-11.5	dBm
NEP	$16 \cdot 10^{-12}$	$\text{W}/\sqrt{\text{Hz}}$
f_0	$500 \cdot 10^6$	Hz
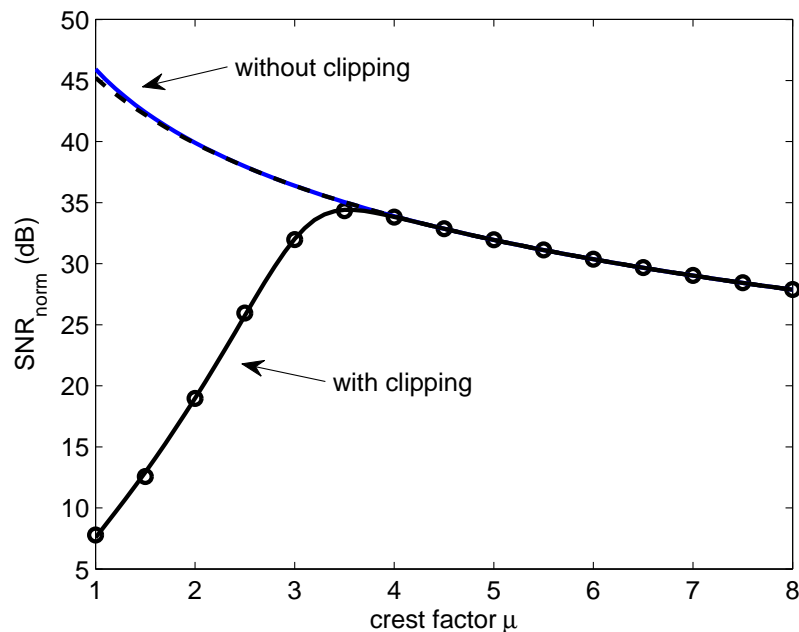
Figure 4.8: $\mathrm{SNR_{norm}}$ as a function of crest factor μ after clipping, with correction factor. Lines depict analytical results and circles depict Monte-Carlo simulation results.

factor

$$\mu' = \mu - 0.7 \tag{4.42}$$

for P_{clip}, (4.35) is re-written as

$$P_{clip} = \sigma_x^2 \left[\left(1 - \mu'^2 \right) \operatorname{erfc} \left(\frac{\mu'}{\sqrt{2}} \right) + \mu' \sqrt{\frac{2}{\pi}} \exp \left(-\frac{\mu'^2}{2} \right) \right] \tag{4.43}$$

leading to the results shown in Fig. 4.8. From the figure, it can be seen that the analytical results correspond very well to simulation results when the correction factor is taken into account.

4.3.2 Quantization Noise

Next to clipping noise, DMT implies the use of D/A and A/D converters so that the effect of quantization noise should also be taken into account. This will result in a more realistic approach for the IM/DD channel capacity calculations when using DMT. Assuming that only two-fold oversampling is used according to the Nyquist

criterion, the quantization noise power P_{quan} of the A/D and D/A converters is given by [49, 55]

$$
\begin{aligned}
P_{quan} &= \frac{1}{12}\Delta^2 \\
&= \frac{1}{12}\left(\frac{2A_{max}}{2^q}\right)^2 \\
&= \frac{(2A_{max})^2}{12\cdot 2^{2q}}
\end{aligned}
\tag{4.44}
$$

where Δ is the quantization step size, A_{max} is the maximum amplitude of the generated respectively captured waveform and q is the number of quantization bits. According to the IM/DD channel model in Section 4.1, A_{max} should be set equal to P_{mean} as derived in (4.5) and can therefore be expressed as a function of the crest factor μ, leading to

$$
P_{quan} = \frac{(2P_{mean})^2}{12\cdot 2^{2q}} = \frac{4\mu^2\langle x^2(t)\rangle}{12\cdot 2^{2q}} = \frac{\mu^2 P_{sig}}{3\cdot 2^{2q}}\,.
\tag{4.45}
$$

This shows that quantization noise also depends on the crest factor of the transmit and receive electrical waveform.

4.3.3 Conclusion

In conclusion, for calculating the IM/DD channel capacity when DMT is used as the modulation format, the normalized SNR (4.22) derived in Section 4.2 is reformulated in this section to include clipping and quantization noise, resulting in

$$
\text{SNR}_{\text{norm}} = \frac{P_{sig} - P_{clip}}{P_{therm} + P_{clip} + P_{quan}}
\tag{4.46}
$$

with P_{sig} as defined in (4.39), P_{therm} as in (4.38), P_{clip} as in (4.43), and P_{quan} as in (4.45). (4.46) is a closed-form expression that depends on μ so that the optimum clipping factor resulting in the maximum normalized SNR and therefore the maximum capacity can always be determined for a given IM/DD DMT transmission system. In Fig. 4.9, analytical curves for SNR_{norm} are plotted as a function of μ at different levels of quantization.

In order to calculate the DMT IM/DD channel capacity, (4.46) should be used together with the channel-response-dependent expressions given by (4.24) and (4.29) for the Gaussian respectively first-order low-pass IM/DD channel responses.

Figure 4.9: SNR_{norm} as a function of crest factor μ after clipping, for different number of quantization bits.

4.4 Validation with Experimental Results

In order to validate the capacity values determined in Section 4.3, experiments with DMT transmission over different lengths of SI-POF have been performed.

4.4.1 Ideal Theoretical Capacity

Using the analytical results derived in Section 4.2 and 4.3, the capacity of an SI-POF channel can be calculated if its f_{3dB} is known. Therefore, measurements have been done to determine the f_{3dB} of different lengths of SI-POF. For the measurements, a 655-nm DVD laser diode (LD) (500-MHz bandwidth) is used as transmitter and a Si-photodetector with trans-impedance amplifier (300-MHz bandwidth) is used as receiver. The SI-POF used is a commercially-available Mitsubishi ESKA GH4001, with a core-diameter of 1 mm, an NA of 0.5, and an attenuation of approximately 140 dB/km at 650 nm.

45

General Case

The measured electrical-to-electrical f_{3dB} values for different lengths of SI-POF are listed in Table 4.2, together with the channel capacity values, calculated based on the parameters given in Table 4.3. These capacity values represent the Shannon capacity, in an ideal case where only Gaussian white (thermal) noise is present (no clipping and quantization noise), limited by the IM/DD channel response. The appropriate expressions used for calculating these values are given by (4.22), (4.24), and (4.29). Additionally, the crest factor μ of the transmitted information signal is assumed to be 1, which maximizes capacity.

Observe from Table 4.2 that two sets of capacity values are calculated, one assuming a Gaussian low-pass and the other assuming a first-order low-pass response for the SI-POF channel. In both cases, the -3dB frequency is chosen to be the same as the experimental values. For comparison, the measured frequency response for 50 m, 100 m, and 200 m of SI-POF are depicted in Fig. 4.10. Although the frequency response of an SI-POF channel can be approximated well with a Gaussian low-pass function for lengths $\geq$ 200 m [52], it can be seen from Fig. 4.10 that the same does not apply for SI-POF with lengths < 200 m. Especially when the LD is directly coupled to the SI-POF, a Gaussian approximation of the frequency response (dashed lines) results in large discrepancies at frequencies beyond the -3dB point. This can clearly be seen from the curves measured with 100 m and 50 m of SI-POF (solid dark lines). The difference is caused by mode coupling, where equilibrium mode

Table 4.2: Calculated theoretical capacity of SI-POF approximated by a Gaussian respectively first-order low-pass channel response. Only Gaussian white noise is considered and a crest factor $\mu = 1$ is assumed.

Length [m]	Measured -3dB bandwidth [MHz]	Gaussian approx. $\mathrm{SNR_{norm}}$ [dB]	Capacity [Gbit/s]	First-order approx. $\mathrm{SNR_{norm}}$ [dB]	Capacity [Gbit/s]
25	200	70.1	13.2	70.9	151.7
50	110	65.7	6.6	66.5	59.4
75	83	59.9	4.3	60.7	28.6
100	62	54.2	2.7	55.0	13.7
150	33	42.9	1.0	43.7	3.0
200	17	31.8	0.3	32.6	0.6

Table 4.3: Parameters used for calculating the SI-POF channel capacity.

Parameter		Value	[Units]
Mean transmitted optical power	P_{mean}	2.5	dBm
Fiber attenuation at 650 nm	α	140	dB/km
Noise equivalent power	NEP	$16 \cdot 10^{-12}$	$W/\sqrt{Hz}$
D/A and A/D quantization*	q	8	bits

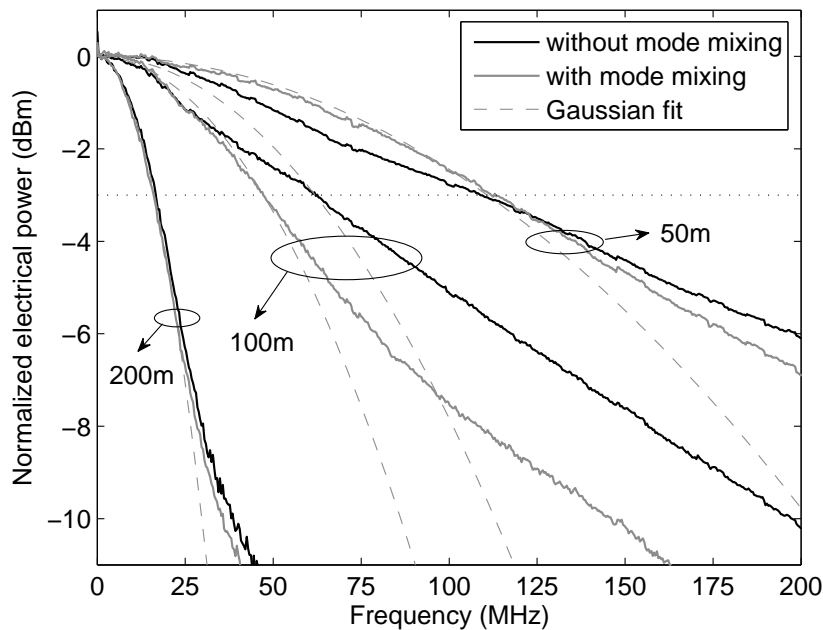*Only for results depicted in Table 4.4 and Fig. 4.12.

Figure 4.10: Measured frequency response for different lengths of SI-POF using a 650-nm laser diode (solid lines), with (gray) and without (black) mode-mixing applied. The dashed lines depict Gaussian low-pass curves, fitted to the same electrical -3dB bandwidth.

distribution is not reached for SI-POF lengths < 200 m due to the low-NA launch by directly coupling the LD to the SI-POF. Naturally, when other optical sources such as an LED or RC-LED are used for coupling light into the SI-POF, different results might be obtained.

However, when mode mixing is introduced at the beginning of the link by winding the SI-POF four times around a cylinder with a radius of 0.5 cm, the results (solid gray lines) resemble the Gaussian approximation more. Nevertheless, it can be seen that a Gaussian low-pass is a pessimistic approximation of the SI-POF channel
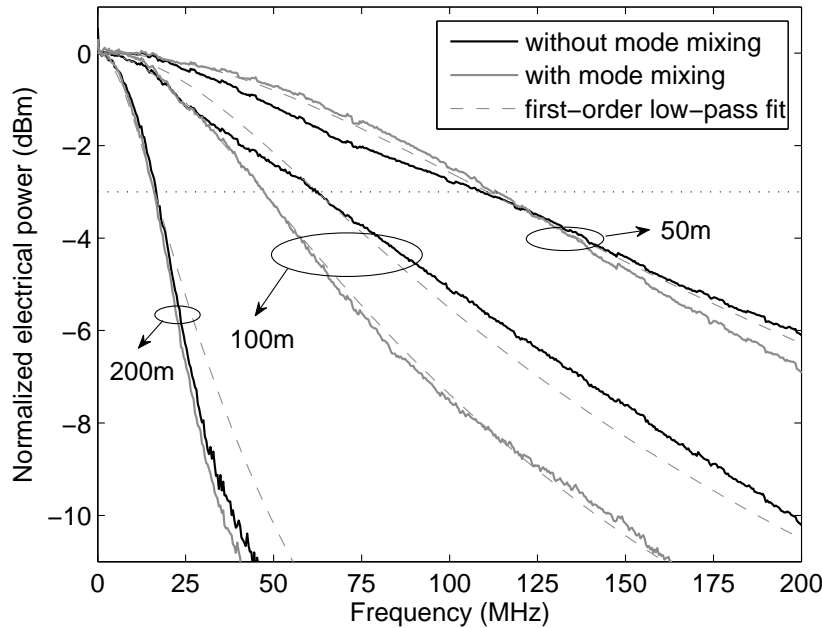
Figure 4.11: Similar results as in Fig. 4.10, but with the dashed lines now representing first-order low-pass curves, fitted to the same electrical -3dB bandwidth.

response for lengths < 200 m. For 100 m of SI-POF, mode mixing reduces the channel bandwidth as a result of a larger amount of modal dispersion. In the case of 200 m of SI-POF, mode mixing doesn't influence the results very much, indicating that equilibrium mode distribution is reached after 200 m. From the results given in Fig. 4.10, it can be concluded that for lengths < 200 m, a Gaussian approximation of the channel response leads to lower capacity values compared to the actual case. This is also the case when mode mixing is introduced at the beginning of the SI-POF. Therefore, actual capacity values of SI-POF should be larger than those calculated using a Gaussian low-pass approximation given in Table 4.2.

As a result, Table 4.2 also shows capacity values that are calculated using a first-order low-pass approximation for the channel response. Obviously, these values are much larger than those using a Gaussian low-pass approximation. Fig. 4.11 shows again the same SI-POF measurement results, but with first-order low-pass frequency response curves having the same -3dB frequencies as the measured curves. For SI-POF lengths < 200 m, it is clear that a first-order low-pass channel approximation is more realistic.

In conclusion, Fig. 4.10 and 4.11 show that the SI-POF channel can be approx-

imated by both a Gaussian and a first-order low-pass response model, depending largely on the launching condition, the amount of mode mixing, and the length of the SI-POF. When insufficient mode filling is present in the SI-POF, a first-order low-pass channel approximation is generally valid. In the case where sufficient mode filling is present so that equilibrium mode distribution is achieved, a Gaussian low-pass channel response model should be used for the SI-POF. In the following, a first-order low-pass channel approximation will be used to evaluate the capacity of SI-POF for lengths < 200 m and a Gaussian low-pass channel approximation will be used to evaluate the capacity of 200 m SI-POF.

DMT Modulation

As already shown in Section 4.3, the use of DMT will produce clipping and quantization noise in addition to the photodetector thermal noise in an IM/DD channel. This will reduce the maximum achievable capacity of the channel depending on the amount of clipping (resulting in a clipping-limited signal crest factor) and the number of quantization bits used by the D/A and A/D converters.

The derived analytical expression (4.46) can be used to determine the normalized SNR, represented by $\mathrm{SNR}_{\mathrm{norm}}$, and used in combination with (4.24) or (4.29) to calculate the maximum theoretically achievable capacity of an IM/DD channel using DMT as the signal modulation format. This has been done for the measured SI-

Table 4.4: Calculated theoretical capacity of DMT over SI-POF at optimum crest factor values, including thermal, clipping, and quantization noise. For lengths up to 150 m, a first-order low-pass channel approximation is used.

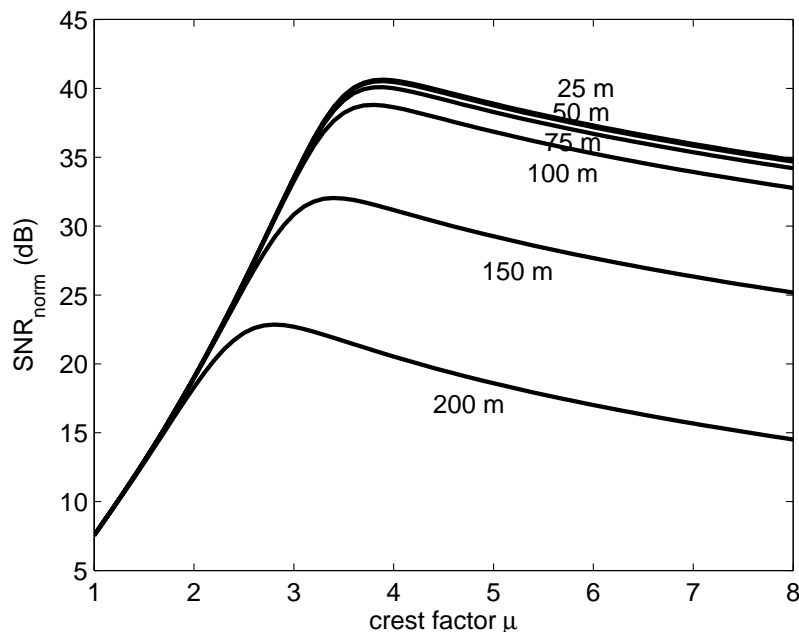| Length [m]	Measured -3dB bandwidth [MHz]	Optimum crest factor	$\mathrm{SNR}_{\mathrm{norm}}$ [dB]	Capacity [Gbit/s]
25	200	3.9	40.6	14.1
50	110	3.9	40.5	7.7
75	83	3.9	40.1	5.6
100	62	3.8	38.8	3.8
150	33	3.4	32.0	1.1
200	17	2.8	22.2*	0.2*

*Gaussian low-pass approximation

Figure 4.12: SNR_{norm} as a function of clipping-limited crest factor μ for different SI-POF lengths.

POF -3dB bandwidth results based on the parameters in Table 4.3 and is presented in Table 4.4. The number of quantization bits is set to 8. For the capacity results, optimum crest factor values that maximize capacity are used for the calculation. These values are derived from Fig. 4.12, where the calculated SNR_{norm} from (4.46) is plotted as a function of the clipping-limited crest factor μ at different SI-POF lengths. From the capacity calculations shown in Table 4.4, Gbit/s-transmission speeds can be expected over up to 150 m SI-POF by employing DMT.

4.4.2 Bandwidth-Limited Numerical Approach

Application of DMT over SI-POF requires the use of D/A and A/D converters. Due to sampling speed limitations of both D/A and A/D converters, the capacity values shown in Table 4.4 may not be realistic when compared to an actual DMT over SI-POF system. In order to make a more realistic estimation of achievable SI-POF capacity values when DMT modulation is employed, a bandwidth-limited numerical approach should be used.

The key aspect of DMT is to decompose a single frequency-selective communi-

cation channel into an equivalent multitone channel consisting of multiple parallel frequency-flat subchannels. By limiting the SI-POF system's bandwidth to B as a result of D/A and A/D sampling speed and dividing the frequency response into N equal subchannels, the optimization problem given in (4.9) and (4.10) can be reformulated [4] as a problem of maximizing the total achievable bit-rate R in bits/s given by

$$\max_{P_n}(R) = \max_{P_n} \left(\frac{1}{N} \sum_{n=0}^{N-1} b_n \right) \cdot B \tag{4.47a}$$

$$= \max_{P_n} \left[\frac{1}{N} \sum_{n=0}^{N-1} \log_2 \left(1 + \frac{\mathrm{SNR}_n}{\Gamma} \right) \right] \cdot B \tag{4.47b}$$

$$= \max_{P_n} \left[\frac{1}{N} \sum_{n=0}^{N-1} \log_2 \left(1 + \frac{P_n \cdot g_n}{\Gamma} \right) \right] \cdot B \tag{4.47c}$$

where b_n is the number of bits allocated to each subchannel n, $\mathrm{SNR}_n = P_n \cdot g_n$ is the SNR per subchannel, g_n represents the subchannel SNR when unit power is applied, Γ is the difference (gap) between the SNR needed to achieve Shannon capacity and the SNR to achieve this capacity at a given bit error probability, and P_n is the allocated power per subchannel, subject to a power constraint given by:

$$\sum_{n=0}^{N-1} P_n = P_{tot} \, . \tag{4.48}$$

P_{tot} is the fixed total available power for transmission. The problem is now to find the optimum distribution of b_n, for $n = 0, 1, \ldots, N$, and the corresponding power distribution per subchannel P_n, in order to maximize the bit-rate. Note that maximum bit-rate is not always achieved when all N subchannels are allocated with information bits, so that b_n and P_n can be 0 for some particular n. Therefore, the optimal solution is not always to use all available subchannels to transmit information, but to use only the ones with the highest SNR.

Similar to (4.12), the solution to this bit and power allocation problem is the water-filling method. In this case, the solution is computed numerically using the optimum rate-adaptive water-filling algorithm as described in [4]. This algorithm computes the maximum achievable bit-rate R for a given communication channel when the SNR per subchannel is known. Due to this numerical approach, the measured frequency response values of different lengths of SI-POF are used for the computation,

Table 4.5: Parameters used for numerical computation of the DMT over SI-POF channel capacity, including quantization and clipping noise, and sampling bandwidth limitation.

Parameter		Value	[Units]
Clipping-limited crest factor	μ	3	
Mean transmitted optical power	P_{mean}	2.5	dBm
Fiber attenuation at 650 nm	α	140	dB/km
Noise equivalent power	NEP	$16 \cdot 10^{-12}$	$W/\sqrt{Hz}$
D/A and A/D quantization	q	8	bits
D/A and A/D sampling bandwidth	B	312.5	MHz

Table 4.6: Comparison of DMT over SI-POF capacities at 650 nm.

Length [m]	Theoretical Capacity* (optimum μ) [Gbit/s]	Theoretical Capacity ($\mu = 3$) [Gbit/s]	Numerical Capacity ($\mu = 3$) [Gbit/s]	Measured Capacity ($\mu = 3$) @ BER $= 10^{-3}$ [Gbit/s]
25	14.1	7.8	1.7	2.0
50	7.7	4.3	1.6	1.6
75	5.6	3.2	1.4	1.5
100	3.8	2.4	1.4	1.4
150	3.4	1.0	0.7	0.4
200	2.8	0.2	0.2	0.1

*From Table 4.4

instead of an analytical low-pass channel response approximation. The considered system bandwidth B is limited to a Nyquist frequency of 312.5 MHz, which corresponds to the maximum sampling speed of the D/A converter (625 MSamples/s) used for measurements that will be described in Section 4.4.3. Additionally, quantization and clipping noise are included in the numerical analysis. In order to have realistic values for the channel SNR g_n defined in (4.47c), the noise power spectral density of the photodetector used for the measurements is measured and considered in the computation as well. Although optimum values exist for the clipping-limited crest factor μ of the DMT signal and can be calculated using (4.46), μ is fixed to 3 in this section's analysis due to comparison purposes with experimental results in Section 4.4.3.

Table 4.5 gives a summary of the parameters used in the numerical computation of the DMT over SI-POF channel capacity. The results are shown in Table 4.6. For better comparison with measurement results, the theoretical capacity results (given in Table 4.4) that were calculated using optimum values for μ have now been re-evaluated with $\mu = 3$. These values are also depicted in Table 4.6. It can be seen that for short lengths of SI-POF (< 100 m), the numerically computed capacity values are significantly lower than the theoretical values. This results from bandwidth limitation due to the D/A and A/D sampling speeds, considered in the numerical computation. For lengths > 100 m, the measured frequency responses resemble the Gaussian approximation more and the SI-POF bandwidth dominates above the D/A and A/D sampling bandwidth. Therefore, the capacity values are more similar to each other.

4.4.3 Transmission Experiments

An important feature of DMT is the possibility to allocate the number of bits per subchannel according to its SNR, typically known as bit-loading. The concept of bit-loading has already been presented in Section 3.6. In the following experiments described in this section, rate-adaptive bit-loading will be applied in order to maximize the achievable transmission rate over SI-POF.

In Section 4.4.2, the optimum rate-adaptive water-filling algorithm [4] was used to compute the maximum achievable bit-rate for the SI-POF channel by considering it as a multitone channel and allocating the optimum number of bits and energy to each subchannel. Similarly, this algorithm can also be used to compute optimum bit-loading in DMT modulation. However, infinite granularity for the number of bits per subchannel is assumed, resulting in non-integer values for the optimum number of bits per subchannel. Therefore, this algorithm is not suitable for practical implementation.

An alternative is to use sub-optimal finite bit-loading algorithms, such as the Chow's rate-adaptive algorithm [48]. This algorithm is based on (4.47) and starts by discarding the subchannels that are least energy-efficient from information transmission, and redistributing the energy to more efficient subchannels to support higher data rates. The non-integer number of allocated bits per subchannel are then

rounded to the nearest integer and the corresponding energy is in- or decreased to support the newly-allocated number of bits at the same performance. Chow's algorithm has been shown to achieve near-optimum performance [4, 48] and will be used in the following to compute rate-adaptive bit-loading for DMT over SI-POF measurements.
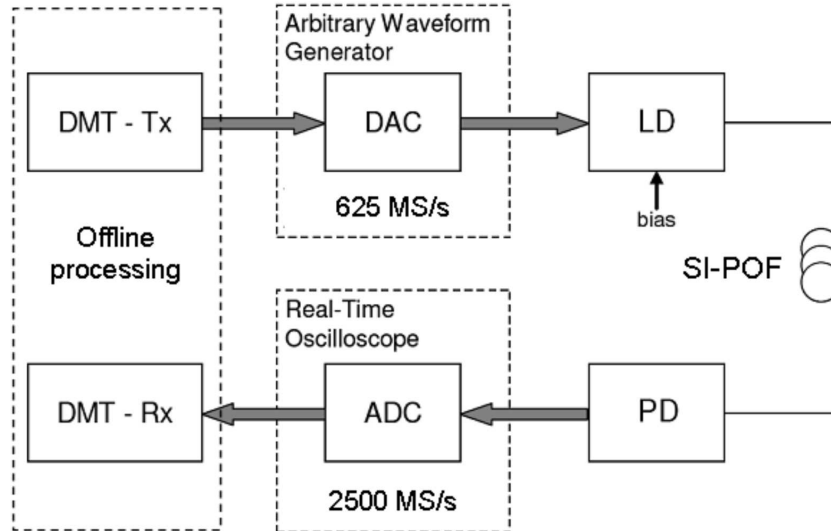

Figure 4.13: Experimental setup for DMT over SI-POF. Tx: Transmitter; Rx: Receiver; LD: Laser diode; PD: Photodetector.

DMT transmission over 100 m of SI-POF

Fig. 4.13 shows the experimental setup of DMT transmission over SI-POF. Using offline processing, a DMT time signal is computed and loaded into the memory of an Agilent N8241A arbitrary waveform generator (AWG). The AWG generates the analogue DMT waveform at a sampling speed of 625 MSamples/s and a resolution of 15 bits. The characteristics of the generated DMT waveform are:

1. 256 subcarriers, first subcarrier at DC not used,

2. 1.2 % cyclic prefix and 1 % DMT preambles,

3. clipping-limited crest factor $\mu = 3$,

4. 312.5 MHz bandwidth.

As will be shown in Chapter 5.2, a larger number of subcarriers will result in better DMT performance. In this experiment, a relatively large number of 256 subcarriers is chosen for comparison purposes with the RC-LED experimental results presented in Chapter 6.1.2. This number can certainly be increased to achieve better performance, but will require more hardware resources in practical realization. In the case of cyclic prefix length, the optimum value of 1.2 % is found by evaluating the system performance starting from a large value and decreasing until performance deterioration is observed. The amount of DMT preambles overhead is also optimized with the same method. The clipping-limited crest factor value is chosen to be comparable to the results in Chapter 6.1.2.

Following this, the analogue electrical waveform from the AWG is then used to drive a low-cost, commercially-available DVD laser diode (655 nm) with integrated ball lens. A DC-bias is added to the bipolar signal via a bias-tee in order to a have a unipolar signal, suitable for driving the laser diode. The mean transmitted optical power after coupling into 0.5 m of SI-POF is measured to be 2.5 dBm and the optical modulation amplitude (OMA), as defined in Appendix B and [56, 57], is 5.4 dBm. The same SI-POF used previously for the frequency response measurements is now used for the DMT transmission experiment. After transmission over 100 m of SI-POF, the optical signal is detected by use of a photodetector with an integrated trans-impedance amplifier.

The signal is then captured with a LeCroy Wavemaster 8500A real-time digital storage oscilloscope with a nominal resolution of 8 bits and a sampling speed of 2.5 GSamples/s. Such a high sampling speed (four-fold oversampling compared to the D/A converter in the transmitter) is used due to the lack of an appropriate (steep) low-pass filter for both anti-aliasing and receiver noise-filtering purposes. Therefore, oversampling in this case enables the implementation of an ideal brick-wall low-pass filter in the digital domain. In a practical system, it is foreseeable that custom-designed high-quality low-pass filters at dedicated frequencies will be available (which is common in commercial DMT and OFDM systems) so that digital emulation is not necessary anymore and sampling speeds closer to 625 MSamples/s can be used. Additionally, oversampling also enhances the effective resolution of the oscilloscope. After the received DMT time samples are captured, these are then stored and demodulated using offline processing.
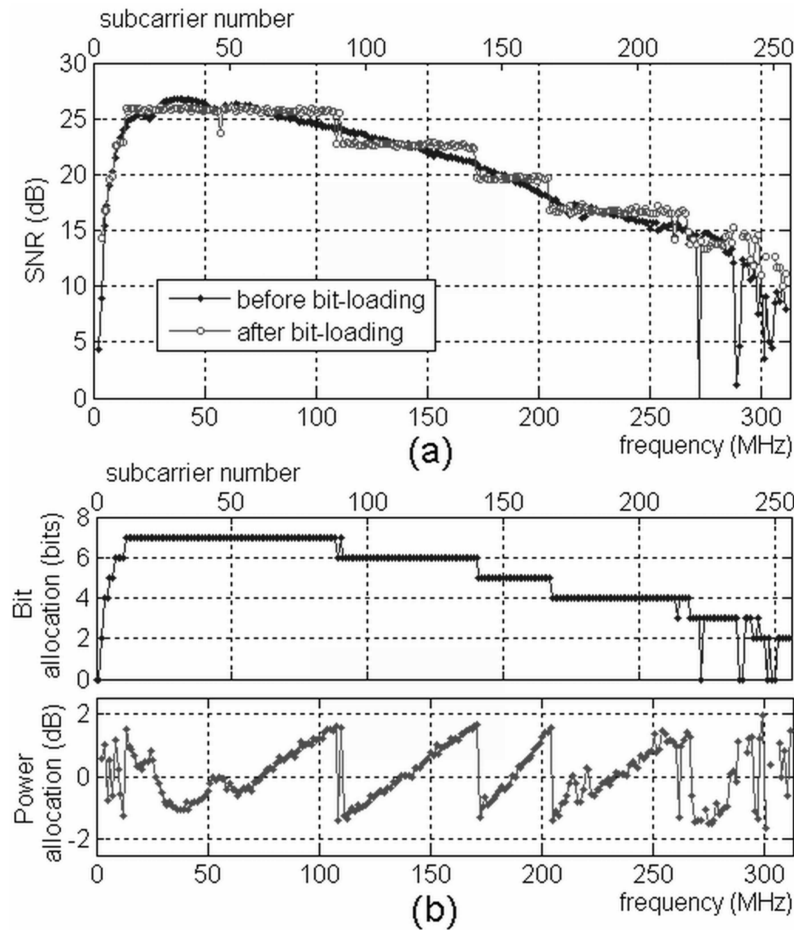
Figure 4.14: DMT transmission characteristics for 100 m SI-POF. (a) Measured SNR per subchannel, before and after bit-loading. (b) Bit and power allocation per subchannel, resulting from bit-loading.

It should be noted that for the experiments, the sampling clocks of the AWG and oscilloscope are free-running and not synchronized with a cable. This is done in order to emulate the performance of a realistic system, where the clocks of the transmitter and receiver are (physically) different and always need to be synchronized with some synchronization algorithm. In this case, synchronization is also performed on the captured data in the digital domain using offline processing according to the method described in Chapter 3.5.

Initially, all subcarriers are loaded with 4 information bits each, corresponding to a modulation format of 16-QAM. From the received and demodulated DMT signal,
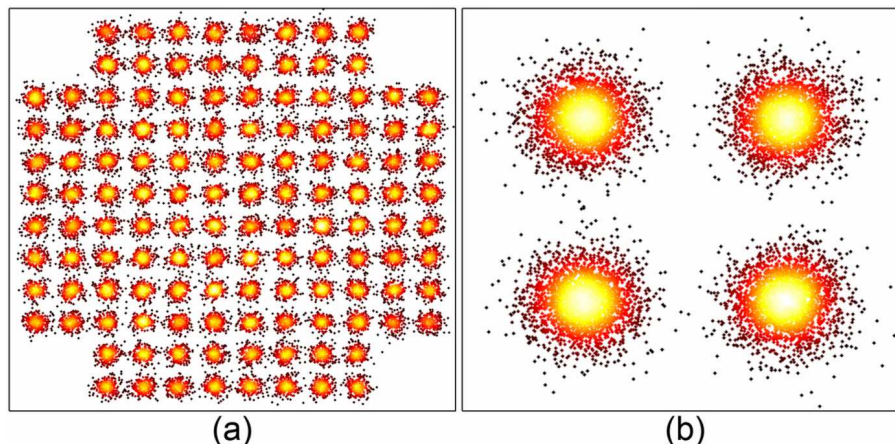
Figure 4.15: Received constellations after transmission over 100 m of SI-POF. (a) 128-QAM, subcarrier 29; (b) 4-QAM, subcarrier 252.

the SNR per subcarrier is estimated (see Fig. 4.14a) and used to compute Chow's rate-adaptive bit-loading. This results in the bit-loading scheme per subcarrier as depicted in Fig. 4.14b. Note the saw-tooth-like power allocation scheme, which is typical for Chow's bit-loading algorithm. It can be seen that the peak-to-peak power deviation is approximately 3 dB, corresponding to the increase of the required SNR for transmitting 1 additional information bit using QAM. As a result of power allocation, the typical stair-case-shaped SNR per subcarrier after bit-loading can be noticed from Fig. 4.14a. An aggregate transmission bit-rate of 1.62 Gbit/s is hereby achieved for a total averaged BER of $1 \cdot 10^{-3}$. After deduction of cyclic prefix, preambles, and 7 % forward error correction coding, a net transmission bit-rate of 1.44 Gbit/s is achieved using DMT modulation over 100 m of SI-POF.

Fig. 4.15 shows two examples of received constellations for the highest and lowest allocated number of bits used for DMT transmission over 100 m of SI-POF. The BER performance per subcarrier is plotted in Fig. 4.16, evaluated after transmission and reception of over 30000 DMT frames (more than $30 \cdot 10^6$ bits). Because the serial data is transmitted in parallel over subchannels with DMT, the total uncoded BER of the received data is evaluated by considering the total number of erroneous bits of all subchannels divided by the overall number of transmitted bits, which is calculated to be $1 \cdot 10^{-3}$. This BER value can be corrected to values $\leq 10^{-9}$ by use of forward error correction (FEC) coding, which is not implemented here in
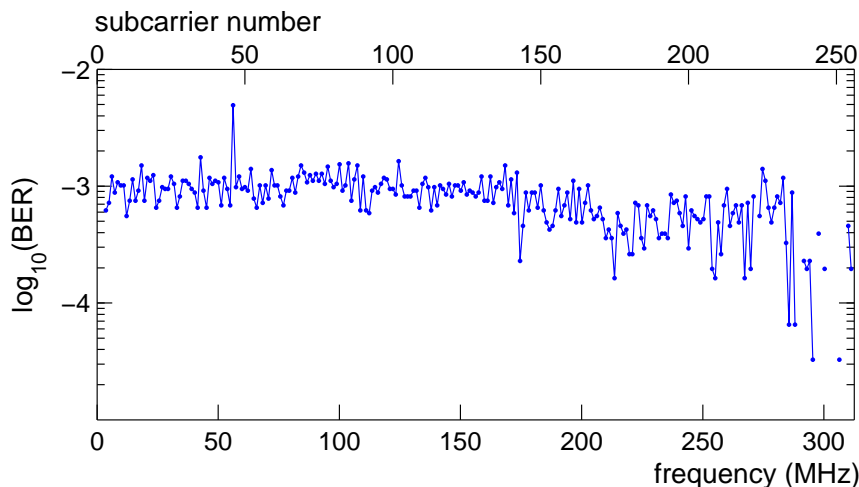
Figure 4.16: Evaluated BER per subchannel. Total averaged BER $= 1 \cdot 10^{-3}$

the experiments. The 7 % overhead required for standard (Reed-Solomon) FEC is, however, considered and included in the calculation of the transmission bit-rates.

DMT over different lengths of SI-POF

Similar measurements with DMT transmission have been performed over different lengths of SI-POF using the same experimental setup shown in Fig. 4.13, where only the cyclic prefix length is optimized for the different SI-POF lengths. The optical transmitted power and OMA are fixed at 2.5 and 5.4 dBm respectively. The maximum achievable transmission rates at a BER of $1 \cdot 10^{-3}$ are listed and compared to the theoretical and numerical values in Table 4.6.

Fig. 4.17 shows the results of Table 4.6 in graphical form, where the capacity values are plotted as maximum achievable bit-rates for the different SI-POF lengths. Notice the good correspondence between the numerical and measured values, resulting from an accurate modeling of quantization and clipping noise. At 200 m, the theoretical, numerical, and measured values correspond well with one another because the bandwidth-limitation is dominated by the SI-POF channel. As the SI-POF lengths get shorter, the numerical and measured results seem to saturate and deviate more from the theoretical ones because the performance is limited by the D/A and A/D sampling bandwidths.

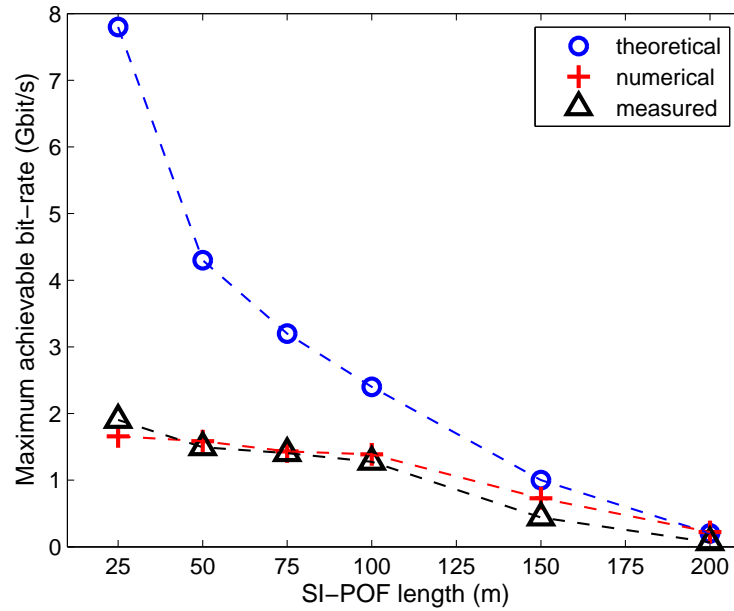By calculating the bit-rate-length products from the theoretical, numerical and

Figure 4.17: Maximum achievable bit-rate for theoretical, numerical, and measured capacity values of different lengths of SI-POF at $\mu = 3$.
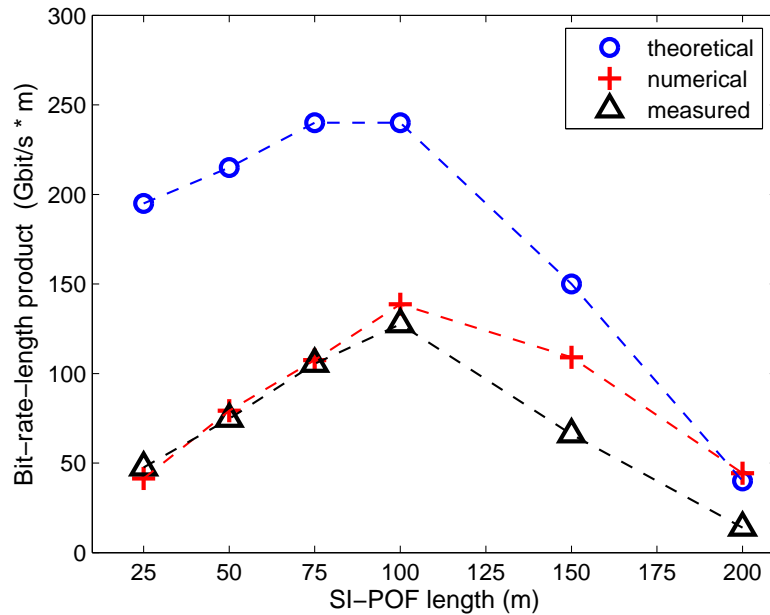

Figure 4.18: Bit-rate-length product for theoretical, numerical, and measured capacity values of different lengths of SI-POF at $\mu = 3$.

measured capacity values, a better insight to the system performance can be gained. Fig. 4.18 shows these values as a function of the SI-POF length. Unlike the capacity results in Fig. 4.17, it is observed from Fig. 4.18 that shorter SI-POF lengths do not give the best performance in terms of bit-rate-length product. For all theoretical, numerical, and measured values, the maximum bit-rate-length product is achieved at an SI-POF length of 100 m. This is caused by the fixed value of $\mu = 3$, which is apparently optimum for the measurement setup at an SI-POF length of 100 m. For lengths < 100 m, all bit-rate length products decrease due to the relatively larger influence of clipping noise. This results from the fact that $\mu = 3$ is not the optimum crest factor anymore for lengths < 100 m. For shorter SI-POF lengths, larger values of μ should be chosen to improve performance, which is confirmed by the results depicted in Fig. 4.12. For SI-POF lengths > 100 m, the bit-rate-length products reduce as a result of the low bandwidth of SI-POF. Overall, the numerical results using the measured frequency responses correspond well to the measurement results. The difference with regard to the theoretical values is due to bandwidth-limitation of the D/A and A/D converters, which is not considered in the theoretical analysis.

4.5   Summary

Fig. 4.19 shows a schematic overview of the optical IM/DD channel capacity analysis presented in this chapter. It is shown that the derived closed-form expressions for calculating the channel capacity can be split into two main parts, one considering the effects of the channel response, and the other considering the SNR resulting from the effects of white noise.

The effects of the channel response are described by expressions (4.24) and (4.29) for respectively the Gaussian and first-order low-pass.

The effects of noise are described by the normalized signal-to-noise ratio SNR_{norm}. This can be calculated using (4.22) when considering only (white) thermal noise, or adding (4.45) for quantization noise. In the case of DMT modulation, the expression given by (4.46) is derived. Next to quantization noise, (4.46) also includes the effect of clipping noise. In this expression, clipping noise is assumed to be white. Due to the use of digital clipping, where the digital DMT waveform is clipped before
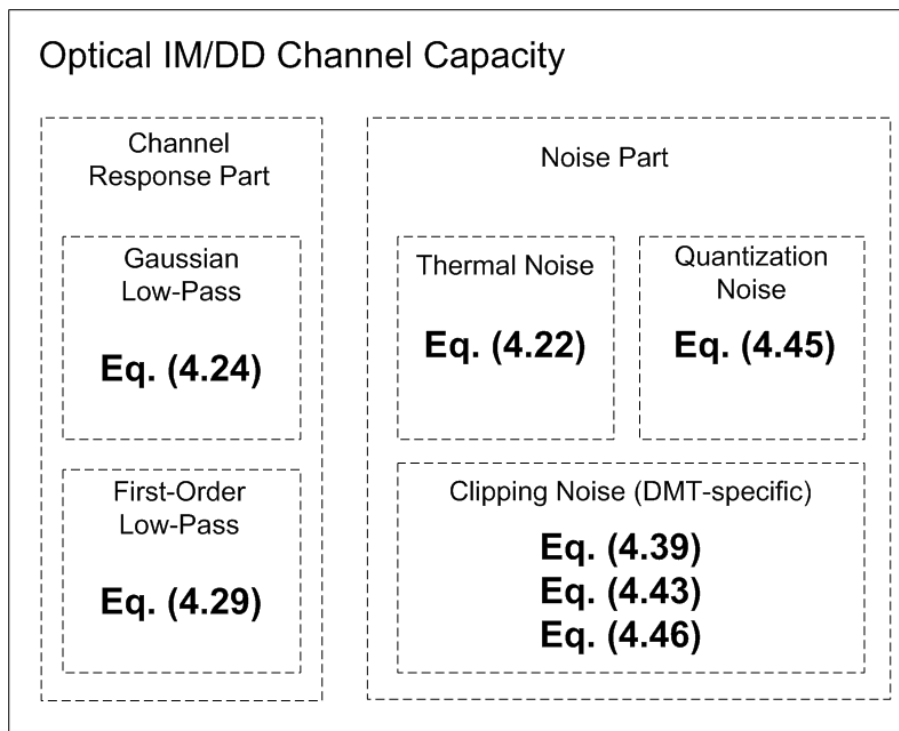
Figure 4.19: Schematic overview of the optical IM/DD channel capacity analysis.

D/A conversion, the bandwidth of this clipping noise is the same as the DMT signal bandwidth (when no extra oversampling in the digital domain is used). By using a correction factor as given by (4.43), it was validated that this corresponds well with simulation results.

Finally, experiments with SI-POF were performed to validate the expressions with DMT modulation. Results showed that the SI-POF channel can be approximated with a first-order low-pass response when insufficient mode filling is present. When sufficient mode filling is present so that equilibrium mode distribution is achieved, a Gaussian low-pass channel response should be used to model the SI-POF. Furthermore, it was found that the D/A and A/D converter sampling speeds (and therefore bandwidths) were limiting the maximum achievable bit-rates over SI-POF to values below the calculated capacity. Numerical results including the converter bandwidth limitations showed good correspondence with measurement results.

CHAPTER 5
OPTIMIZING DMT PERFORMANCE

This chapter investigates the most important parameters for optimizing the performance of DMT. Also, the advantages of DMT are presented and experimental results are presented to show why DMT is attractive to use and can counter a lot of issues found in optical IM/DD channels despite the drawback of high crest factor.

5.1 Clipping

As already shown in Chapters 3 and 4, the main drawback of DMT is the large crest factor. Especially in an IM/DD channel where only the intensity is modulated, signals with large crest factors will suffer more from the impact of receiver (thermal) noise, resulting in lower SNR values as shown by (4.22). However, in Section 4.3, it was shown to be advantageous to partly clip the DMT signal to trade-off the resulting clipping noise against the gain with regard to receiver noise (due to a smaller crest factor), since large instantaneous amplitudes occur very rarely due to statistical averaging. A closed-form expression (4.46) was derived so that the SNR of the system can be calculated as a function of the crest factor μ of the DMT signal, limited by clipping. This section investigates the influence of clipping on the performance of DMT over an IM/DD channel and shows that performance can be maximized by optimizing clipping and therefore crest factor values. The definition
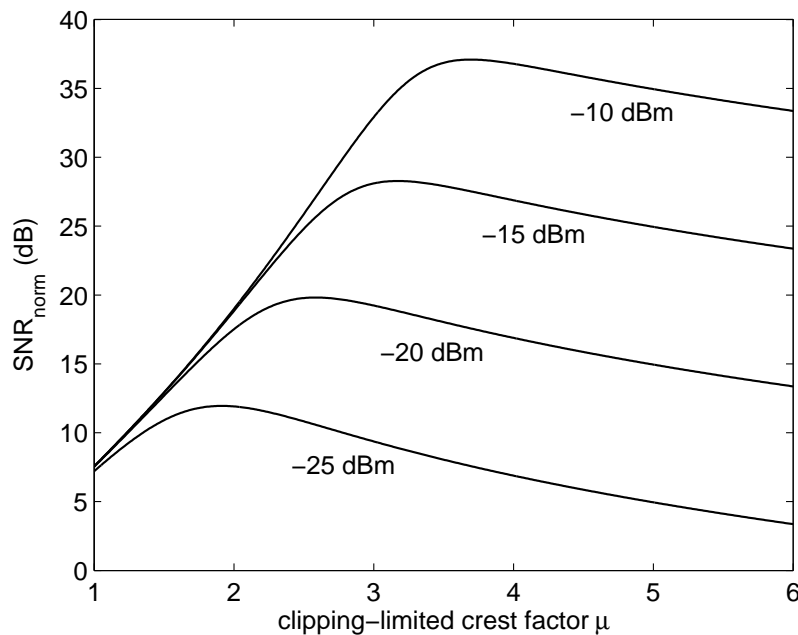
Figure 5.1: SNR_{norm} as a function of clipping-limited crest factor, for different values of mean received optical power. The results are calculated using (4.46) based on the parameters given in Table 5.1.

of clipping is given in (4.30), resulting in a clipping-limited crest factor μ given by (4.32)

$$\mu = \frac{A_{clip}}{\sqrt{\langle x^2(t) \rangle}}$$

where A_{clip} is the maximum allowed amplitude level and $\langle x^2(t) \rangle$ denotes the mean power of the DMT time signal $x(t)$ before clipping.

By using (4.46), the optimum clipping-limited crest factor μ can be determined for a given set of system parameters. Fig. 5.1 shows an example where SNR_{norm} is plotted as a function of μ for different values of mean received optical power. An NEP of $16 \cdot 10^{-12}$ W/$\sqrt{\text{Hz}}$ is assumed and quantization noise is not taken into account. Because (4.46) does not depend on the shape of the channel response, this is equivalent to an ideal flat channel response. The channel bandwidth is chosen to be 500 MHz. The parameters used for obtaining the results in Fig. 5.1 are summarized in Table 5.1.

From Fig. 5.1, it is observed that optimum clipping values exist that maximize SNR_{norm} and therefore also system performance. By plotting these curves for dif-

Table 5.1: Parameters used for obtaining the results in Fig. 5.1 and 5.2.

Parameter		Value	[Units]
Channel frequency response		ideal flat channel	
Channel bandwidth	f_{3dB}	500	MHz
Noise equivalent power	NEP	$16 \cdot 10^{-12}$	$W/\sqrt{Hz}$
D/A and A/D quantization	q	infinite (ideal)	bits
DMT FFT size*	$2N$	512	points
Cyclic prefix length*	N_{CP}	0	points
Number of subcarriers modulated with information*	$N-1$	255 (DC not modulated)	

*Only for simulation results in Fig. 5.2.

ferent values of mean received optical power and determining μ each time at the maximum value of SNR_{norm}, optimum values for μ can be obtained as a function of the mean received optical power. This is plotted in Fig. 5.2, where the mean received optical power needed for a system BER of $1 \cdot 10^{-3}$ (receiver sensitivity) is depicted as a function of μ for simulation results using different levels of QAM modulation. The simulation parameters are given in Table 5.1, where again an ideal flat channel response is assumed. For the simulation, a DMT FFT size of 512 points is used and 255 subcarriers are used to carry information. Due to the ideal flat channel, no cyclic prefix is needed.

From the simulation results in Fig. 5.2, optimum values for μ can also be determined. Comparing these simulation results with the curve derived indirectly from the analytical expression (4.46), the optimum values of μ seem to correspond well. Therefore, it can be concluded that (4.46) provides an accurate estimation of the optimum μ to use for maximizing performance of DMT transmission over an IM/DD channel.

Finally, observe from Fig. 5.1 that the optimum μ at a mean received optical power of -15 dBm is approximately 3.2. This happens to correspond well with the optimum μ for the 256-QAM simulation results in Fig. 5.2. Notice from Fig. 5.1 that SNR_{norm} in this case corresponds to a value of 28.3 dB, which is similar to the E_s/N_0 that is theoretically required for uncoded 256-QAM modulation to obtain a BER of $1 \cdot 10^{-3}$.
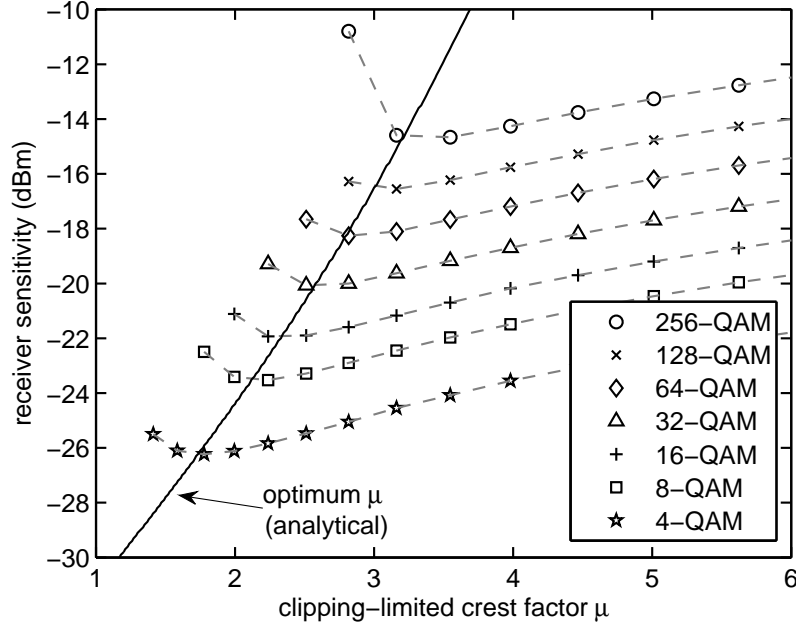
Figure 5.2: Optical receiver sensitivity for a system BER of $1 \cdot 10^{-3}$ as a function of DMT signal crest factor, limited by clipping. The dark solid line depicts the optimum clipping-limited crest factor values derived using (4.46).

5.2 Number of Subcarriers

Next to the crest factor, the number of subcarriers N used for DMT transmission should also be optimized in order to maximize the performance of DMT over an IM/DD channel. This section investigates the influence of the number of subcarriers on the effects of clipping noise, bit-loading, and non-linearity in the electrical-to-optical power conversion.

5.2.1 Bit-Loading

First of all, because the first subcarrier (at DC) is not used to transmit information due to practical purposes, higher bit-rates can be achieved when more subcarriers are used. For a flat channel frequency response with uniform bit-allocation, where all except the first subcarrier are modulated with data, the total system bit-rate b_{tot} is given by

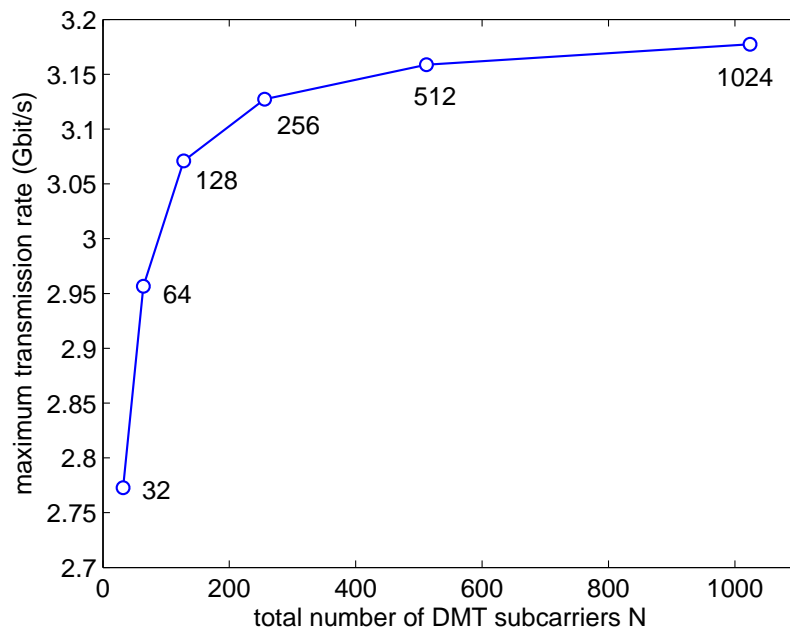$$b_{tot} = \frac{\log_2 M \cdot 2\,(N-1)}{2N + N_{CP}} \cdot f_s \tag{5.1}$$

Figure 5.3: Simulation results showing the maximum achievable DMT transmission-rate with bit-loading at BER $= 1 \cdot 10^{-3}$ for different number of DMT subcarriers N. A Gaussian channel response with f_{3dB} of 500 MHz is assumed and N_{CP} is fixed at 8 for all N. Mean received optical power is -10 dBm at an NEP of $16 \cdot 10^{-12}$ W/$\sqrt{\text{Hz}}$ and μ is set to 10 so that clipping noise is negligible.

where M is the modulation level used (e.g. 16 for 16-QAM), N is the total number of DMT subcarriers, N_{CP} is the number of cyclic prefix points, and f_s is the sampling speed of the D/A converter for an FFT size of $2N$. From (5.1), it can easily be seen that b_{tot} will increase for larger values of N.

Next to this, a large number of subcarriers also have a positive effect when combined with the use of bit-loading. As discussed in the previous sections, the key aspect of DMT is to decompose a single frequency-selective communication channel into an equivalent multitone channel consisting of multiple parallel frequency-flat subchannels. By employing bit-loading, the modulation format (number of allocated bits) and power per subchannel is optimized to the subchannel SNR. Therefore, the finer the decomposition of the frequency-selective channel into N subchannels, the better the DMT system can adapt to the frequency-dependent response of the channel.

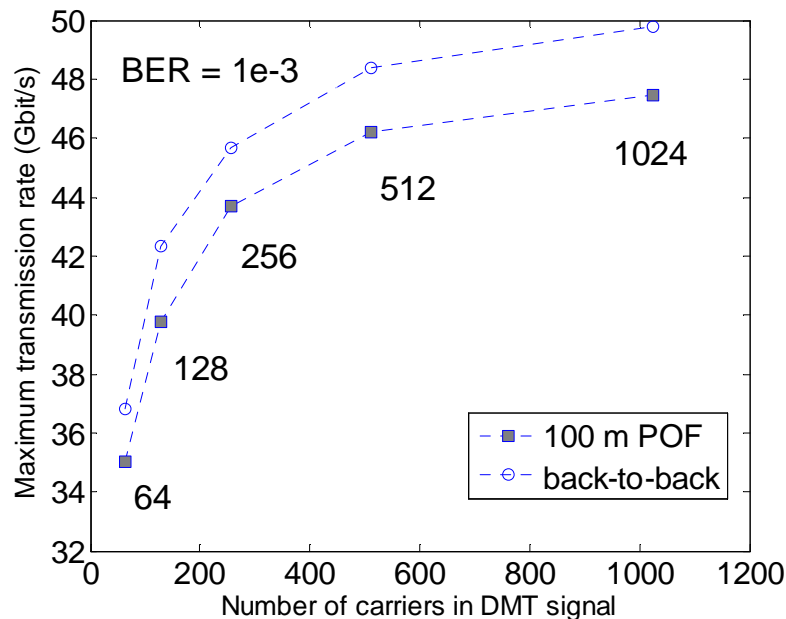This performance gain is illustrated in Fig. 5.3, where rate-adaptive bit-loading

Figure 5.4: Experimental results from Section 6.2.2 showing the maximum achievable DMT transmission rate with bit-loading at BER $= 1 \cdot 10^{-3}$ for different number of subcarriers N. Mean received optical power is fixed at $+4$ dBm.

is used to maximize the transmission rate of a DMT over IM/DD channel, with a Gaussian channel response as given in (4.8). The results are obtained by simulation, with the same parameters as given in Table 5.1, except for the channel frequency response, FFT size, cyclic prefix length, and the number of modulated subcarriers. The mean received optical power is set to -10 dBm, and the clipping-limited crest factor μ is set to 10, so that the influence of clipping noise can be neglected (see Fig. 5.1). Fig. 5.3 shows the maximum achievable bit-rate at a system BER of $1 \cdot 10^{-3}$ by employing rate-adaptive bit-loading for a different number of total available DMT subcarriers N. Because the first subcarrier at DC is not used, the number of modulated subcarriers is always equal to $N - 1$. The FFT size is $2N$ and a fixed cyclic prefix length N_{CP} of 8 is used to avoid inter-symbol interference resulting from the Gaussian channel response. Observe from the results that higher performance is achieved for larger values of N.

This conclusion is also verified by the experimental results shown in Section 6.2.2, duplicated here in Fig. 5.4. For both back-to-back and 100 m of GI-POF, perfor-
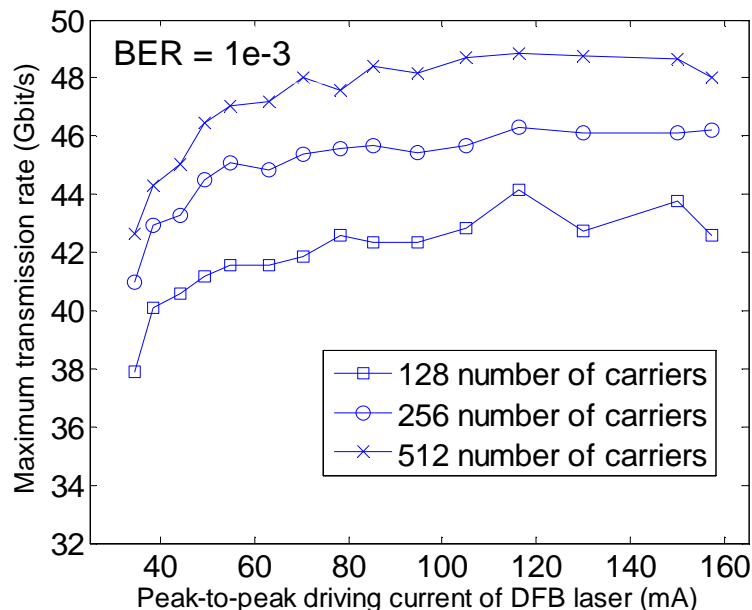
Figure 5.5: Experimental results from Section 6.2.2 showing the maximum achievable DMT transmission rate with bit-loading at BER $= 1 \cdot 10^{-3}$ for different peak-to-peak laser drive currents and number of subcarriers N.

mance is improved for larger number of DMT subcarriers used, with a fixed cyclic prefix length of 8 in all cases. More details about the results are presented in Section 6.2.2. Notice that the performance gain for larger N tends to saturate, so that the trade-off between implementation complexity for large N and its performance gain will determine what the optimum number of DMT subcarriers is. Additionally, one should note that a large N will result in a long DMT symbol period. As long as the channel response is stable during a DMT symbol period, this will not cause additional penalty when using a large number of subcarriers for DMT transmission.

5.2.2 Non-linearity

The results in Section 6.2.2 also discuss the influence of the number of subcarriers on the transmitter non-linearity in the electrical-to-optical power conversion process. Fig. 5.5 shows a preview of the results because this is also of interest in this section. In the figure, the maximum achievable bit-rate (at BER $= 1 \cdot 10^{-3}$) with rate-
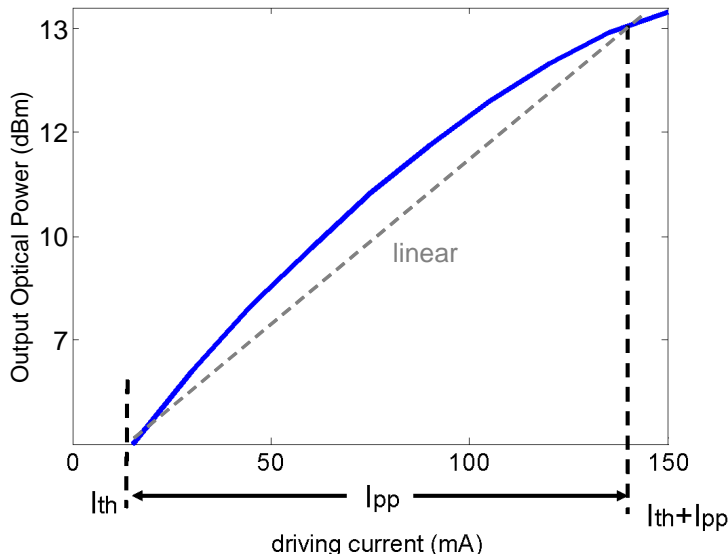
Figure 5.6: Measured static optical output power as a function of static driving current of DFB laser used for obtaining the results in Fig. 5.5 and 5.7. I_{th}: threshold current; I_{pp}: peak-to-peak driving current.

adaptive bit-loading is plotted against the peak-to-peak laser driving current I_{pp}. However, an optical attenuator is used to keep the mean optical received power at a fixed value of +4 dBm, for all values of I_{pp}. This is done to eliminate the influence of receiver (thermal) noise, resulting from higher received optical power for larger I_{pp}. Therefore, for larger I_{pp}, only the influence of non-linearity in the laser current-to-optical power conversion process should be observed.

Nevertheless, from Fig. 5.5, only the performance increase due to the use of a larger number of DMT subcarriers can be observed, which was already shown in Fig. 5.3 and 5.4. No significant connection between laser non-linearity and the number of DMT subcarriers can be noticed. Additionally, for larger I_{pp}, performance does not seem to decrease.

5.3   Transmitter Non-Linearity

Furthermore, the results in Section 6.2.2 also show the influence of non-linearity in the laser current-to-optical power conversion process on the performance of DMT.
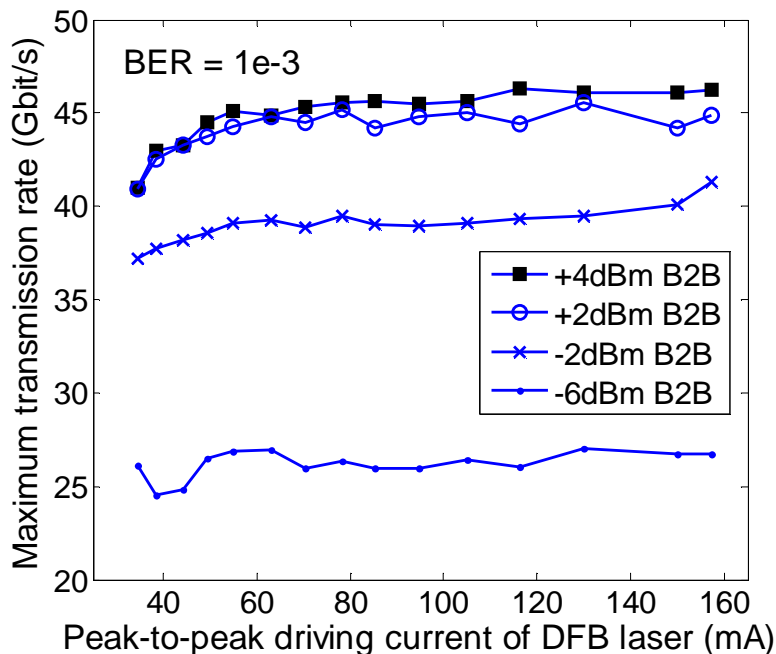
Figure 5.7: Experimental results from Section 6.2.2 showing the maximum achievable DMT transmission rate with bit-loading at BER $= 1 \cdot 10^{-3}$ for different peak-to-peak laser drive currents and at different received optical powers.

Fig. 5.6 depicts the measured static optical power as a function of static driving current for the DFB laser which is used to obtain the non-linearity results plotted in Fig. 5.7. For larger values of the peak-to-peak laser driving current I_{pp}, Fig. 5.7 shows the maximum achievable bit-rate using DMT with rate-adaptive bit-loading. An optical attenuator is used to fix the mean optical received power at a constant value for increasing I_{pp}. This is done to eliminate the influence of receiver (thermal) noise, resulting from higher received optical power for larger I_{pp}. Therefore, for larger I_{pp}, only the influence of non-linearity in the laser current-to-optical power conversion process should be observed.

However, from Fig. 5.7, it can be observed that the DMT performance stays constant for increasing peak-to-peak driving current I_{pp}, up to a value of 160 mA, which is the maximum value specified for the DFB laser. This indicates that the static non-linearity in the laser current-to-optical power conversion, which was measured and depicted in Fig. 5.6, does not influence the (dynamic) DMT performance

significantly. Indeed, static non-linearity is not a good figure of merit to charac-
terize the non-linearity effects in the current-to-optical power conversion process
when a dynamic driving current is used. The reason for this is that non-linearity in
current-to-optical power conversion mainly occurs due to saturation effects because
insufficient holes and electrons are able to recombine in a timely manner. This how-
ever, is a relatively slow process and is more evident when slow-varying or static
driving currents are applied.

For the results shown in Fig. 5.7, it can be concluded that the non-linearity limits
of the DFB laser have not yet been reached in the case of dynamic DMT modulation
with I_{pp} values up to 160 mA. Therefore, DMT performance deterioration is not
observed for larger values of I_{pp}. One might increase I_{pp} to values even larger than
160 mA until the actual limit for dynamic non-linearity is reached. However, due
to specifications of the DFB laser, this has not been done for the measurements
depicted in Fig. 5.7.

In conclusion, following the results presented in this section, it can be implied
that non-linearity in the current-to-optical power conversion process is more pro-
nounced not only for slow-varying, but also non-dynamic, periodic (low crest factor)
modulation signals. Multi-carrier waveforms such as OFDM and DMT, however,
are known for their highly dynamic amplitude values, leading to a large crest factor.
Statistically, large peaks do not occur very often and are random in nature (non-
periodic). Due to these infrequent and irregular peaks, saturation effects are less
likely to take place in the current-to-optical conversion process because sufficient
holes and electrons are often present for recombination. Therefore, non-linearity
issues are less pronounced and should be less critical for DMT transmission, when
compared to other modulation formats.

CHAPTER 6
DMT EXPERIMENTS

The DMT concept of dividing a frequency-selective channel into multiple flat-frequency subchannels and the ability to adapt the modulation format and power for each of this subchannel can prove to be very beneficial in an IM/DD channel. This chapter presents some examples in the form of experimental results for PMMA POF, perfluorinated POF, and optical wireless.

6.1 Poly-Methyl-Methacrylate (PMMA) POF

With its widespread adoption in mass-markets like automotive and industrial Ethernet, the standard PMMA step-index plastic optical fiber (SI-POF) with a 1-mm large core has proven to be a robust, low-cost, and easy to install transmission medium. These unique features make the SI-POF a highly attractive candidate for in-building networks requiring data rates ranging from 1 Gbit/s (IEEE 1394b, Gigabit Ethernet) to about 3 Gbit/s (HDTV). Due to its large diameter, modal dispersion limits the bandwidth of the SI-POF to approximately 35 MHz at 100 m, an inferior value compared to that of silica multimode fibers (MMF).

Recently, several efforts have been undertaken to counter such bandwidth problems [58]. While some efforts concentrate on the development of novel fiber and components such as respectively the 1-mm graded-index PMMA plastic optical

fiber (GI-POF) [14, 15, 16] and red-wavelength VCSELs [13], other focus on better transceiver electronics [59] or novel transmission technologies in combination with digital signal processing. Examples for these are adaptive channel equalization and multilevel signaling [60, 61, 10, 62], and multi-carrier techniques including OFDM and DMT [63, 26]. The idea of multi-carrier modulation is to split a high-data-rate stream into many parallel lower-bit-rate sub-streams, so that high-speed data transmission in highly dispersive channels is made possible [9].

6.1.1 1-Gbit/s Transmission over SI-POF

This experiment presents the initial idea of using spectral-efficient multi-carrier modulation to enable 1-Gbit/s transmission over the standard SI-POF. Although the multi-carrier modulation used here cannot be exactly considered as DMT modulation, it was the first experiment that demonstrated the feasibility of Gigabit transmission rates over SI-POF [63]. For comparison, the highest bit rate ever reported before this experiment was an optimal on-off keying SI-POF transmission experiment with equalization, achieving a bit-rate of 531 Mbit/s [64]. Similar multi-carrier techniques such as OFDM and DMT are already widely employed in commercial systems such as ADSL, WLAN, and WiMAX, demonstrating the potential for low-cost implementation in SI-POF networks.

Experimental setup

As shown in Fig. 6.1, a Rohde & Schwarz SMU200A vector-signal generator (VSG) is used to generate the multiple subcarrier waveforms for transmission. The complex waveforms are pre-computed externally using the Rohde & Schwarz WIN-IQ-SIM software and loaded into the two arbitrary waveform generators (AWG) of the VSG, where they are then output cyclically. The total length of the precomputed waveforms consist of 8 million samples. Each AWG is used to generate 40 independent subcarriers (from -40 MHz to $+40$ MHz) with a carrier spacing of 2 MHz, centered on a frequency of 0 Hz. The resulting complex baseband waveform is then output from the digital to analog converters as in phase (I) and quadrature (Q) components and modulated onto a radio frequency with an analog IQ-modulator. In the experiment, radio frequencies of 50 MHz and 150 MHz are used.
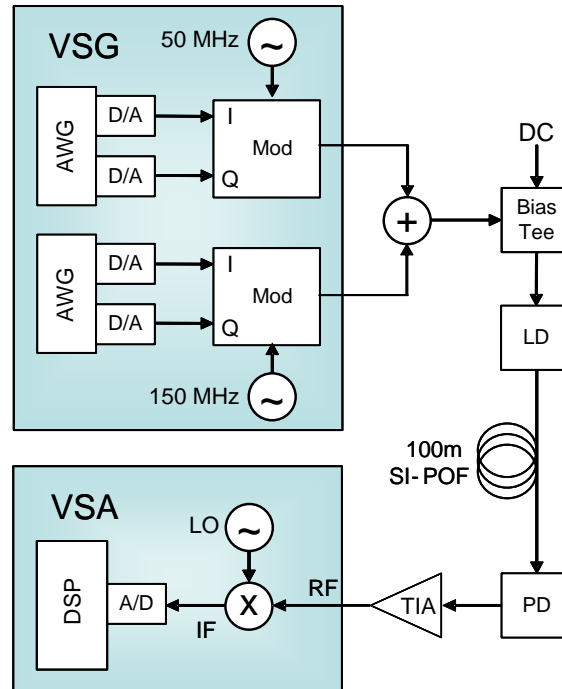
Figure 6.1: Experimental setup; VSG: vector-signal generator; AWG: arbitrary waveform generator; D/A: digital-analog converter; Mod: Modulator; LD: laser diode; PD: photodiode; TIA: trans-impedance amplifier; RF: radio frequency; VSA: vector-signal analyzer; IF: intermediate frequency; LO: local oscillator; A/D: analog-digital converter; DSP: digital signal processing.

At the output of the VSG, the RF modulated signals from the two AWGs are combined to yield the transmission signal. This signal comprises two transmission bands of 80 MHz bandwidth each, centered respectively at 50 MHz and 150 MHz (see Fig. 6.2b). The resulting signal is then used to directly modulate a lensed 650-nm laser diode (LD), normally used in DVD players. A DC-bias is added to the bipolar electrical signal in order to achieve a unipolar signal for driving the LD. The output light from the LD (+3.5 dBm optical power) is directly coupled into 100 m of commercial SI-POF (ESKA Premier GH4001) with a numerical aperture of 0.5, a diameter of 1 mm, and an optical attenuation of 14 dB. The receiver comprises a standard Si-PIN photodiode with an active diameter of 1 mm, followed by a trans-impedance amplifier. A Rohde & Schwarz FSQ3 vector-signal analyzer (VSA) is used to demodulate the received multiple subcarrier waveforms.

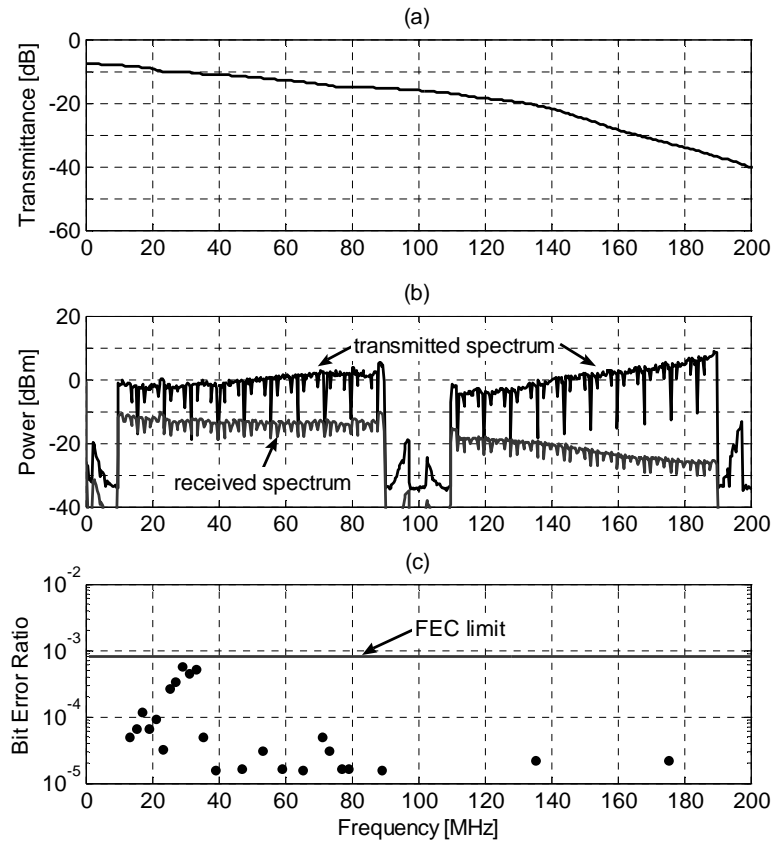The electrical transfer function of the entire system (see Fig. 6.2a) has a -3 dB

Figure 6.2: (a) Electrical transfer function of the transmission system. (b) Transmitted and received signal power spectra. (c) Measured bit-error ratio of each sub-carrier. No errors were detected for subcarriers without a dot.

bandwidth of 33 MHz and decreases smoothly to -32 dB relative attenuation at 200 MHz. By using a simple version of adaptive multiple subcarrier modulation, the transmitted signal is manually adapted for this specific channel characteristic. This is done first by adjusting the relative powers of the subcarriers in a way such that constant SNR is achieved throughout each transmission band, which is commonly known as pre-emphasis. This effect becomes clear from a comparison of the transmitted and received spectra as shown in Fig. 6.2b. Secondly, the modulation format of each transmission band is chosen according to the achievable SNR. Each subcarrier is hereby modulated with M-ary quadrature amplitude modulation (M-QAM), at a symbol rate of 1.8 MBaud. By using root-raised cosine filters with a roll-off factor of 0.1, spectral interference between adjacent subchannels is avoided.
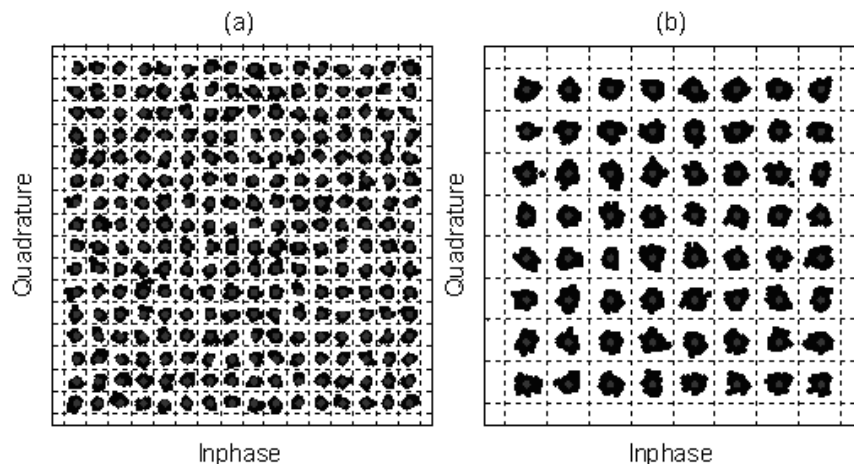
Figure 6.3: Constellation diagrams received after transmission over 100 m of SI-POF. (a) 256-QAM modulated carrier at 11 MHz. (b) 64-QAM modulated carrier at 111 MHz.

The crest factor of the transmit time signal is minimized by proper adjustment of the relative phases of the subcarriers. While the SNR of the lower-frequency transmission band allows 256-QAM to be used, the upper band allows 64-QAM. The total bit rate thus amounts: 40 Ch × 1.8 MBd/Ch × (8 bits/symbol + 6 bits/symbol) = 1.008 Gbit/s.

Results

Using the VSA, the received multiple subcarrier signal is demodulated. This is done by separately down converting each of the in total 80 subcarriers to an intermediate frequency (IF) of 20 MHz and sampling the resulting signal with an analog-to-digital (A/D) converter. Further demodulation of the M-QAM signal is done in real-time digitally in the VSA. For every subcarrier, a block of 8000 continuously demodulated symbols is recorded. The performance of each subchannel is then evaluated by comparing the stored demodulated and de-mapped received sequence with the transmitted pseudo-random binary sequence of length 2^{9-1}. The resulting bit error ratios (BER) of all individual subcarriers are depicted in Fig. 6.2c. No error was detected at those subcarriers where no dot is plotted. Using for example a Reed-Solomon (511,479) forward error correction coding will reduce the BER values to below 10^{-9} for all subcarriers, resulting in a net bit rate of 945 Mbit/s.

The constellation diagrams shown in Fig. 6.3 further illustrate the efficiency of the modulation technique as well as the linearity of the system.
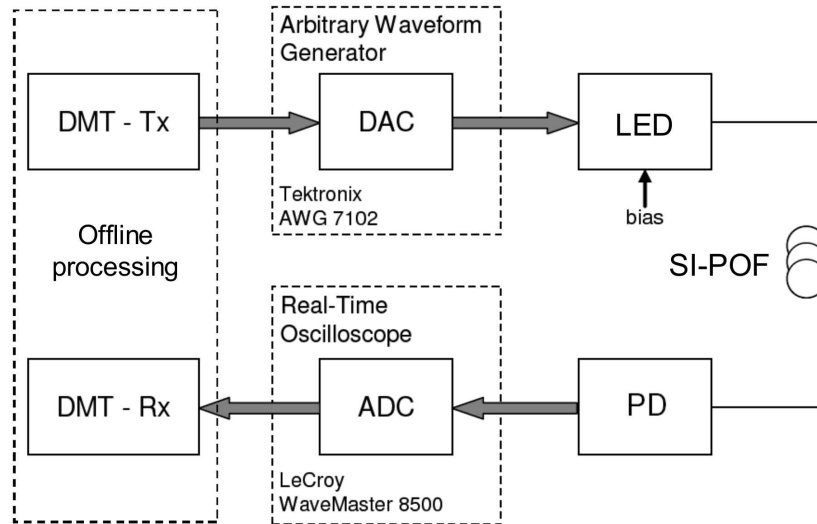
Figure 6.4: Measurement setup. Tx: transmitter, Rx: receiver, DAC: digital-to-analog conversion, ADC: analog-to-digital conversion, PD: photodetector.

6.1.2   1-Gbit/s Transmission using RC-LED

So far, all reported Gigabit transmission experiments over SI POF required the use of laser diodes due to insufficient bandwidth of light emitting diodes (LEDs). However, LEDs have significant advantages such as high reliability and robustness, longer lifetime, lower cost, less sensitivity to temperature variations, and relaxed eye safety regulations. Combining such advantages with high speed Gigabit transmission will make the use of SI-POF even more attractive. In this section, it is shown that by use of spectrally efficient DMT modulation, it is possible to realize 1 Gbit/s transmission over 50 m of SI-POF, even with an LED-based transmitter [26]. The LED used in this experiment is a resonant-cavity type [12], which is denoted here as RC-LED.

Measurement Setup

Fig. 6.4 depicts the measurement setup of the DMT transmission system for SI-POF. The principle of DMT transmission over an optical IM/DD channel is presented in details in Chapter 3 and 4. A single D/A converter is used to generate the digitally-computed DMT waveform, which is then used to drive an RC-LED. For the measurement, a DMT time signal consisting of 18000 random DMT symbols is
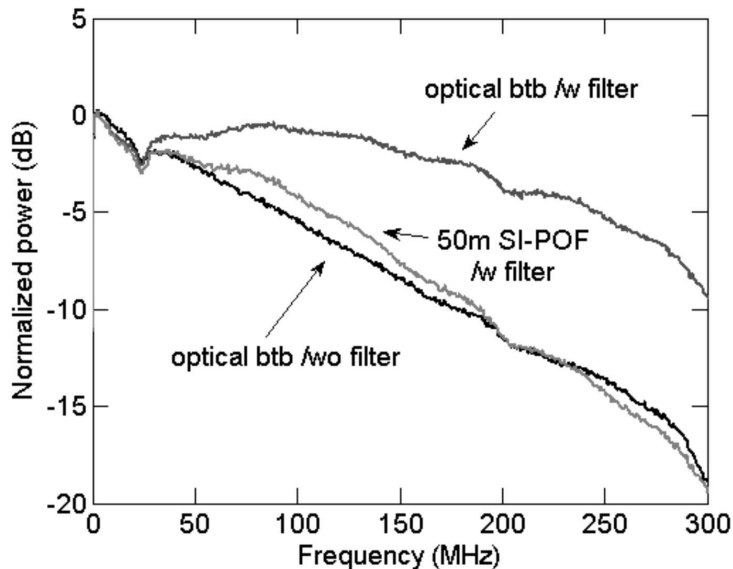
Figure 6.5: Measured frequency responses of transmission system with and without analog peaking filter.

pre-computed using custom Matlab software and output cyclically by an arbitrary waveform generator (AWG) with 10 bits of resolution. In order to easily filter out the baseband signal from the high frequency aliasing products produced by the D/A converter of the AWG, the 250 MHz DMT waveform is output with four-fold oversampling at a rate of 1 GS/s. In a practical system with a properly designed anti-aliasing filter, lower sampling speeds closer to the Nyquist frequency of 500 MS/s can be used.

The transmitter used in the experiment consists of a commercial resonant cavity type LED (Firecomms) with a wavelength of 650 nm and an optical output power of -3 dBm, driven in its linear region with a modulation index of approximately 0.8. This corresponds to an optical modulation amplitude (OMA) of -0.97 dBm, defined as in Appendix B. As can be seen from Fig. 6.5, the optical back-to-back system has a -3 dB bandwidth of around 50 MHz, a value which is normally insufficient for Gigabit transmission using conventional on-off keying modulation. By adding a simple analog peaking filter consisting of a two-stage air-inductor based high-pass filter [65], the -3 dB bandwidth of the optical back-to-back system is increased to about 175 MHz. This filter is inserted between the D/A converter and the RC-LED. Adding 50 m of commercial SI-POF (6.5 dB attenuation, 0.5 NA) reduces the

bandwidth of the entire system to values similar to the back-to-back case without pre-equalizing filter (see Fig. 6.5).

After transmission over 50 m of SI POF, a 0.8 mm diameter Si-photodiode with trans-impedance amplifier is used to detect the optical signal. The amplified received electrical signal is then captured by a real-time digital oscilloscope at a sampling rate of 1 GS/s and a nominal resolution of 8 bits. Its effective resolution is specified to be approximately 7.5 bits, which is enhanced to 8.5 bits due to the use of oversampling (two times with regard to the Nyquist sampling frequency of 500 MS/s). Using offline processing, the captured DMT data are demodulated and the bit-error ratio (BER) is evaluated.

Results and Discussion

As studied in Section 4.3, DMT time-domain signals are characterized by high crest factor values. In order to optimize performance, the digital DMT waveform should be limited in amplitude by digital clipping before D/A conversion. By measuring the performance for different clipping-limited crest factor values, the optimum is found at approximately 2.9. This value is different from the analytical optimum of approximately $\mu = 3.8$ at 50 m given in Fig. 4.12, because the analog peaking filter before the RC-LED enhances the crest factor of the analog DMT waveform. Derived from the analysis in Chapter 5.2, a larger number of subcarriers will result in better DMT performance. For this experiment, a relatively large number of 256 subcarriers was chosen without a specific reason for the upper limit. This number can certainly be increased to achieve better performance, but will require more hardware resources in practical realization. In order to put a realistic upper bound on the number of subcarriers, further investigation on hardware complexity with regard to the FFT size and target bit-rate should be performed, which is recommended in Chapter 9 as an important point for further work.

The previously chosen parameters are then used for the transmission experiment, where the QAM mapping per subcarrier is manually adapted to the SNR of the transmission channel, as given in Fig. 6.6. Of the 256 subcarriers, the first five are not used at all because of low SNR. Note that this method is a simple, non-optimum version of the more sophisticated Chow bit-loading algorithm, which is presented in Chapter 3.6. Using this adaptive scheme, a total capacity of 1133 bits
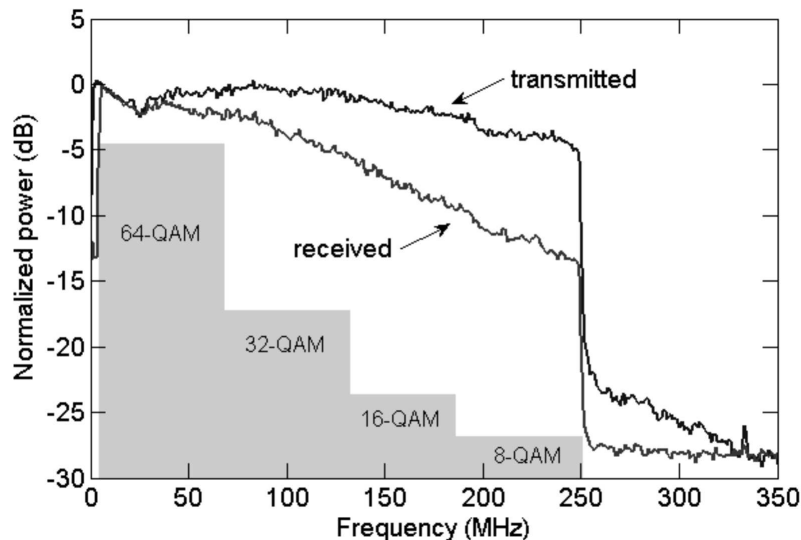
Figure 6.6: Transmitted and received (after 50 m SI-POF) electrical DMT spectra together with applied adaptive QAM mapping.

per DMT symbol is achieved. This corresponds to a transmit time of 1.024 μs per DMT symbol, resulting in a total transmission speed of 1133 bits / 1.024 μs = 1106 Mbit/s within a transmission bandwidth of 250 MHz. A spectral efficiency of $1106/250 = 4.4$ bit/s/Hz is hereby achieved.[1]

Fig. 6.6 shows the transmitted and received electrical DMT signal spectra. Although the -3 dB bandwidth of the system with 50 m of SI-POF is about 50 MHz, 1-Gbit/s transmission is realized using DMT. Fig. 6.7 shows the calculated BER per subcarrier for a total of 18000 received DMT symbols, which equals a total of 20 million bits. Because the serial input data before DMT is transmitted in parallel using subcarriers with DMT, the total BER of the received data should be weighted according to the number of bits transmitted per subcarrier and averaged from all subcarriers used and is calculated to be $4 \cdot 10^{-4}$. By employing standard Reed-Solomon FEC coding with an overhead of 7 %, BER values $\leq 10^{-12}$ can be achieved.

In Fig. 6.8, the received constellation diagrams after DMT demodulation are depicted, indicating the received signal quality. Every constellation diagram contains the superimposed results of all subcarriers with the same constellation. After deduc-

---

[1]For MMF systems, spectral efficiency is calculated this way because optical transmitter linewidths are practically ≥ 1 nm, so that it is considered as baseband transmission.
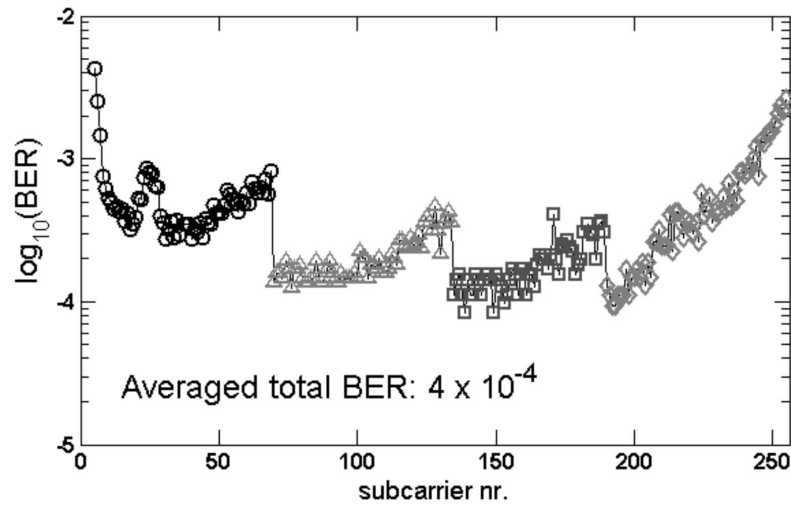
Figure 6.7: Calculated BER per subcarrier from measurement results after transmission over 50 m of SI-POF and DMT demodulation.
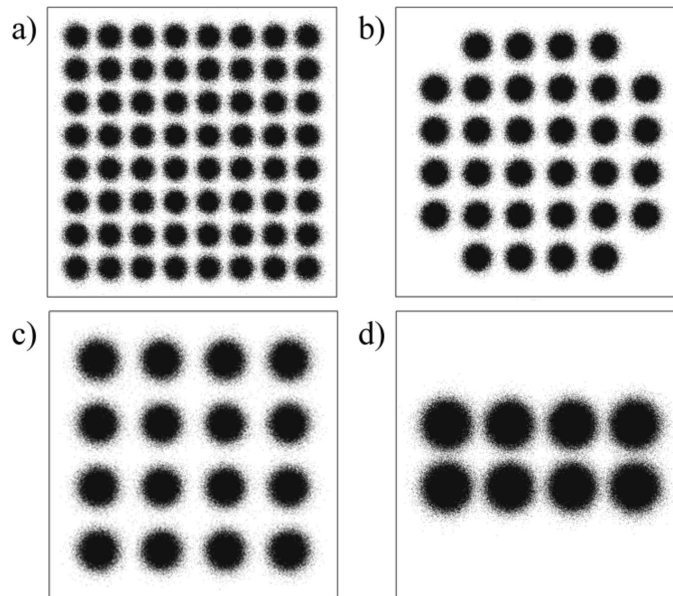

Figure 6.8: Superimposed plot of received constellation diagrams, containing all results from subcarrier nr. (a) 6 to 70, (c) 71 to 135, (d) 136 to 190, (e) 191 to 256.

tion of 3.125 % of cyclic prefix, 1 % of DMT preambles, and 7 % of FEC overhead, the net transmission bit rate equals 993 Mbit/s.

6.1.3   Beyond 1-Gbit/s Transmission

In the previous sections, experiments have shown that 1-Gbit/s DMT transmission is possible over up to 100 m of PMMA SI-POF. Using LEDs, 1 Gbit/s can also be achieved up to a length of 50 m by employing DMT. As the speed of electronics is increasing and the costs are reduced, multicarrier transmission such as OFDM and DMT have recently also been proposed for high speed optical communication systems, both for long-haul systems employing single mode silica optical fibers [32, 33, 34] as well as short-range systems with multimode silica fibers [66, 29]. In this section, experiments demonstrating the possibility of 10-Gbit/s transmission over PMMA POF with large core diameters (≥ 0.5 mm) are presented [67].

Applications are found in high-speed server interconnects, network switches, and short-range local area networks, where bit-rates of 1 Gbit/s are no longer sufficient. Unlike standard 10-Gbit/s optical systems that are available nowadays for such applications, the use of large-diameter POFs will allow the costs of such systems to be reduced substantially by employing cheap commercial DVD laser diodes (visible, red light) and large-area Si photodiodes. The challenge, however, is that all the aforementioned components have low -3 dB bandwidths of around 1 GHz. In order to achieve 10-Gbit/s transmission, a highly spectral-efficient modulation format such as DMT is proposed and investigated in this section. Three common types of PMMA POFs are hereby considered:

1. 1-mm core diameter PMMA SI-POF

2. 0.5-mm core diameter PMMA SI-POF

3. 1-mm core diameter PMMA graded-index POF (GI-POF).

Experimental Setup

The experimental setup of the transmission system is shown in Fig. 6.9. A Tektronix AWG7102 arbitrary waveform generator (AWG) is used to generate the DMT time signal, which is pre-computed offline and loaded into its memory. A total of 512 subcarriers are used for the DMT transmission, corresponding to an IFFT-length of 1024. The number of subcarriers used in this measurement is larger than the
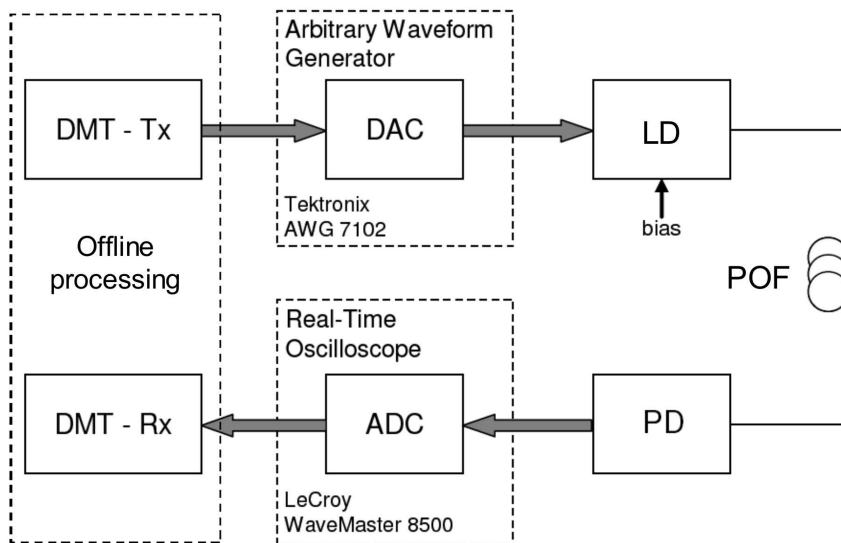
Figure 6.9: Experimental setup. Tx: transmitter, DAC: digital-to-analog converter, LD: laser diode, PD: photodetector, ADC: analog-to-digital converter, Rx: receiver.

256 used in the previous measurements because a larger DMT signal bandwidth is now used for achieving 10-Gbit/s transmission. Therefore, in order to achieve flat-frequency channel response per subcarrier, this larger frequency spectrum has to be divided among more subcarriers.

Of the 512 subcarriers, the last subcarrier is used as pilot tone while the first subcarrier at 0 Hz is not used at all. Unlike the previous measurements, this measurement makes use of selective mapping in order to reduce the crest factor in a distortion-less manner. The concept of selective mapping is to define two different QAM constellation mappings, that are different to each other [25, 36]. In this case, the 2 constellations are chosen to be the inverse of each other, so that a constellation point which is large in amplitude will be mapped onto a constellation point close to 0 in the inverse constellation mapping. Using the complex-valued IFFT operation as described in Chapter 7.1, two real-valued IFFT operations can be computed simultaneously. By giving the same data which are mapped onto 2 different inverse constellations as two different inputs C_n and D_n into the complexed-valued IFFT according to (7.2) given in Chapter 7.1, two DMT frames with different crest factor values (containing the same data) will result from the IFFT operation. The DMT frame which has the lowest crest factor value is then transmitted over the channel,

together with the pilot tone at the last subcarrier. This pilot tone contains binary information that denotes which constellation mapping was used to map the data before performing the IFFT operation. Therefore, this last subcarrier cannot be used to transport other data. Transmission parameters of the remaining 510 subcarriers are then adapted to the SNR of the channel in a simple way by using 64-QAM mapping for the first 250 subcarriers and 32-QAM mapping for the rest, which is not the same as Chow's rate-adaptive bit-loading described in Chapter 3.6.

With the AWG, the pre-computed DMT waveform is generated at a speed of 8 GS/s (four-fold oversampling) and a resolution of 10 bits, occupying a transmission bandwidth of 2 GHz (see Fig. 6.10a). For each DMT symbol, 3.3 % of cyclic prefix is added to increase the tolerance to inter-frame interference. Besides selective mapping, the crest factor of the DMT frames is reduced further by clipping. The output signal from the AWG is then used to directly modulate a low-cost, commercial 650-nm DVD laser diode (LD). The output light from the LD is launched into the three different types of POF, each with a length of 5 m. The optical signal after transmission is detected by a commercial 0.8-mm diameter Si PIN photodetector (PD) with a built-in coupling lens. Finally, the received electrical signal from the detector is captured by a LeCroy Wavemaster 8500 real time digital storage oscilloscope with an A/D converter of 8 bits nominal resolution and a sampling rate of 10 GS/s, corresponding to an oversampling factor of 2.5. The captured DMT data is then decoded to a binary sequence using a software implementation of a DMT demodulator and the BER is evaluated.

1-mm Core SI-POF Results

Fig. 6.10 and 6.11 show the experimental results for DMT transmission with 510 subcarriers over 5 m of standard 1 mm SI-POF, of the type Mitsubishi GH4001. The -3 dB electrical bandwidth of the system is about 1 GHz (see 6.10a). The two different QAM mappings used for the subcarriers can be observed from Fig. 6.10b. The same figure shows that the BER of the subcarriers at lower and higher frequencies are very high. The large BER at lower frequencies is caused by the low frequency cut off of the electrical components used while the degradation of the SNR causes the BER to worsen at higher frequencies. By leaving these subcarriers out and using only subcarriers 15 to 397 for actual data transmission, an aggregate
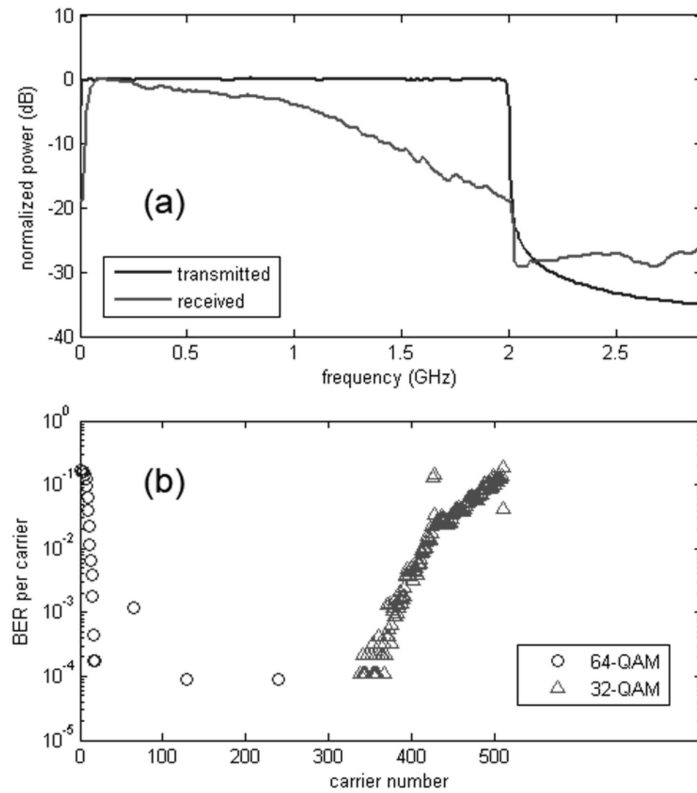
Figure 6.10: : (a) DMT spectra for 5 m of 1-mm SI-POF at 8.4 Gbit/s. (b) Measured BER per subcarrier (nr. 15 to 397 are used for actual data transmission).

Figure 6.11: : Received constellations after 5 m of 1-mm SI-POF for subcarriers (a) 15 to 250 (b) 251 to 397. Total BER $= 2 \cdot 10^{-4}$.

Figure 6.12: : (a) DMT spectra for 5 m of 0.5-mm SI-POF at 8.3 Gbit/s. (b) Measured BER per subcarrier (nr. 15 to 390 are used for actual data transmission).
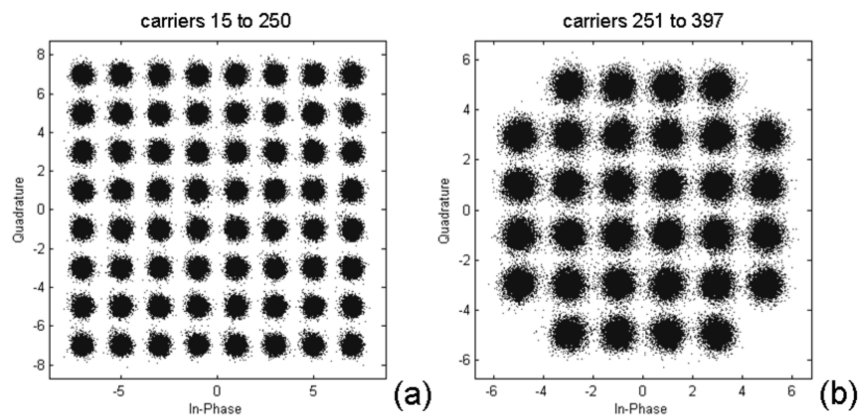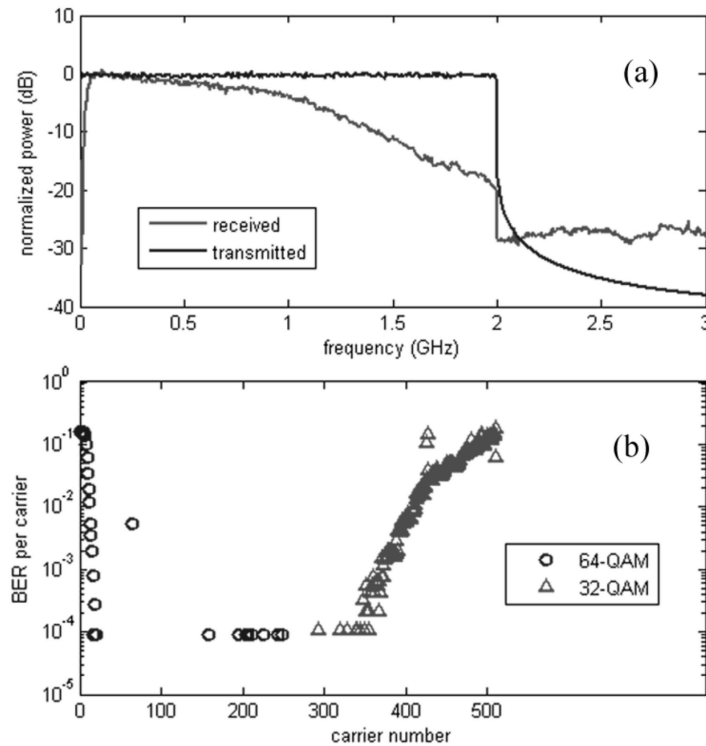
DMT transmission bit rate of 8.4 Gbit/s is achieved.

The total averaged BER of the received data is calculated to be $2 \cdot 10^{-4}$, which, by use of standard Reed-Solomon (255,239) FEC coding will reduce to values $< 10^{-12}$. After deduction of the overhead needed for DMT (pilot tones, cyclic prefix) and 7 % of FEC overhead, the net transmission bit rate equals 7.5 Gbit/s. This is achieved in a transmission bandwidth of 2 GHz, using only low cost transceivers and SI-POF. Fig. 6.11 shows the received constellations of the subcarriers 15 to 397, which are used for data transmission with DMT. Fig. 6.11a shows a superimposed constellation of all subcarriers employing 64-QAM mapping and Fig. 6.11b shows those for 32-QAM mapping.

0.5-mm Core SI-POF Results

In order to compare and check whether a smaller-core SI-POF can achieve better results, the same measurements are repeated for 5 m of 0.5-mm core diameter SI-
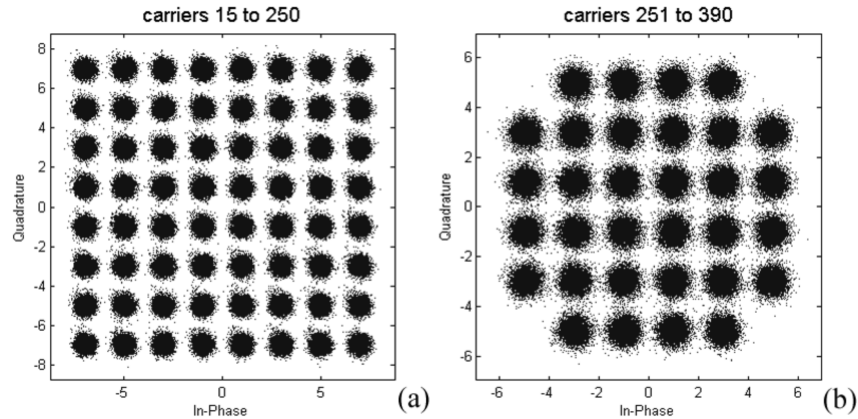
Figure 6.13: : Received constellations after 5 m of 0.5-mm SI-POF for subcarriers (a) 15 to 250 (b) 251 to 390. Total BER = $2 \cdot 10^{-4}$.

POF of the type Toray PFU-CD500. In Fig. 6.12 and 6.13, the results are shown. It can be seen that similar results are obtained in comparison to the 1 mm SI-POF. Using only subcarriers 15 to 390 for actual data transmission, an aggregate DMT transmission bit rate of 8.3 Gbit/s is achieved at a BER of $2 \cdot 10^{-4}$. This results in a net transmission bit rate of 7.4 Gbit/s after deduction of all transmission overhead including FEC.

1-mm Core GI-POF Results

Finally, the results for 5 m of 1-mm core diameter PMMA GI-POF are given in Fig. 6.14 and Fig. 6.15. An aggregate DMT transmission bit-rate of 8.6 Gbit/s is achieved at a BER of $2 \cdot 10^{-4}$, when subcarriers 15 to 408 are used for actual data transmission. After deduction of transmission overhead and FEC, a net transmission bit-rate of 7.7 Gbit/s is achieved. This slightly higher bit-rate is achieved due to the bandwidth of the GI-POF, which is better than that of the SI-POF as a result of the graded-index structure in the GI-POF. Although the GI-POF used (Optimedia OM-Giga) is specified to have a bandwidth larger than 1.5 GHz at 100 m, the results obtained are not significantly better than those of the SI-POFs. Therefore, it can be concluded that the limitation for 10 Gbit/s DMT transmission in these experiments originate from the transmitter and receiver bandwidths, and not from the plastic fibers. Further improvements in transmitter and receiver bandwidths and coupling efficiency should make 10 Gbit/s DMT transmission over large core diameter PMMA
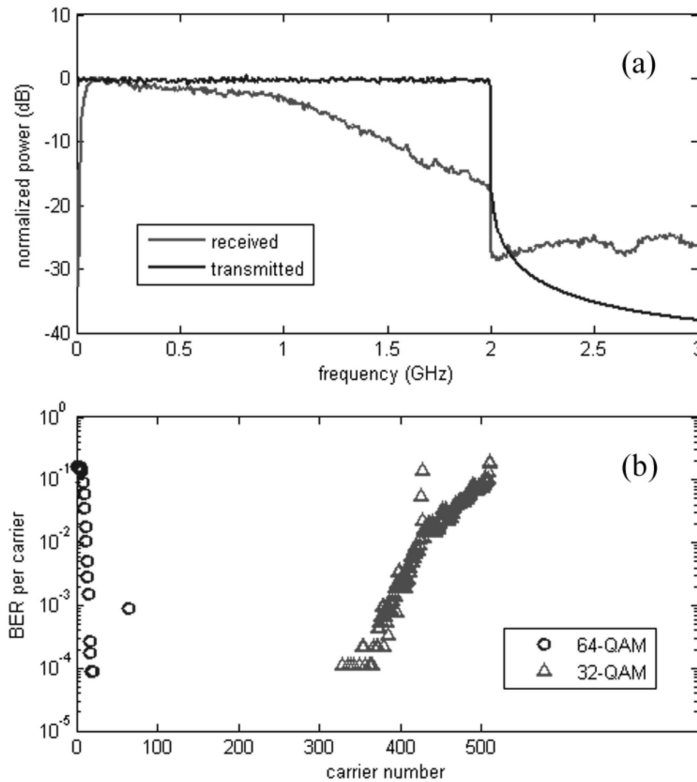
Figure 6.14: : (a) DMT spectra for 5 m of 1-mm GI-POF at 8.6 Gbit/s. (b) Measured BER per subcarrier (nr. 15 to 408 are used for actual data transmission).

POF possible.

Pre-equalized DMT for 1-mm SI-POF

Instead of using adaptive bit-allocation, one can also use pre-equalization with DMT to compensate for the low-pass channel frequency response. Fig. 6.16 shows an example of this, where the transmission parameters of the subcarriers are adapted to the SNR of the channel by digital pre-equalization in the frequency domain. This is easily accomplished by weighting the data sequences of each subcarrier with a factor that is inversely proportional to the SNR of the transmission channel, before passing the data to the IFFT for DMT modulation. The same experimental setup as in Fig. 6.9 is used.

A total of 128 subcarriers are used for the DMT transmission, where the last subcarrier is used as a pilot tone (for selective mapping) and the first 8 subcarriers
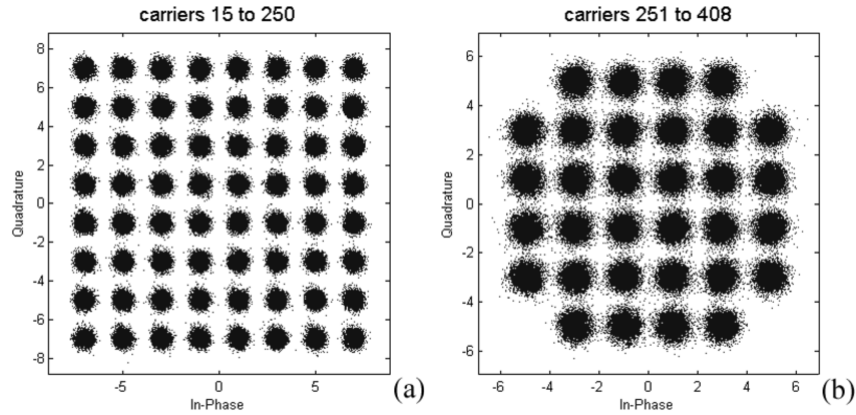
Figure 6.15: : Received constellations after 5 m of 1-mm GI-POF for subcarriers (a) 15 to 250 (b) 251 to 408. Total BER $= 2 \cdot 10^{-4}$.
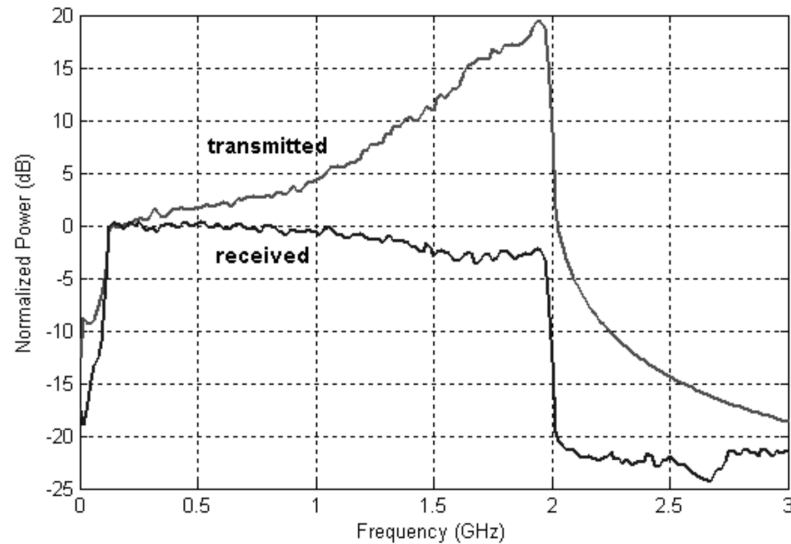

Figure 6.16: Frequency response before and after 10-Gbit/s transmission over 5 m of 1-mm SI-POF using DMT modulation and pre-equalization.

are not used at all because of the low-frequency cut-off of the electrical amplifiers used in the PD. The modulation mapping is fixed at 32-QAM for all subcarriers. For each DMT symbol, 3.9 % of cyclic prefix is added. Notice from Fig. 6.16 that an almost flat frequency response results after transmission over the channel. Fig. 6.17 shows the overall received constellation diagram containing a superposition of all received and demodulated constellation points from all subcarriers used. The BER is calculated to be $1.7 \cdot 10^{-3}$. FEC coding can be used to reduce this value to an
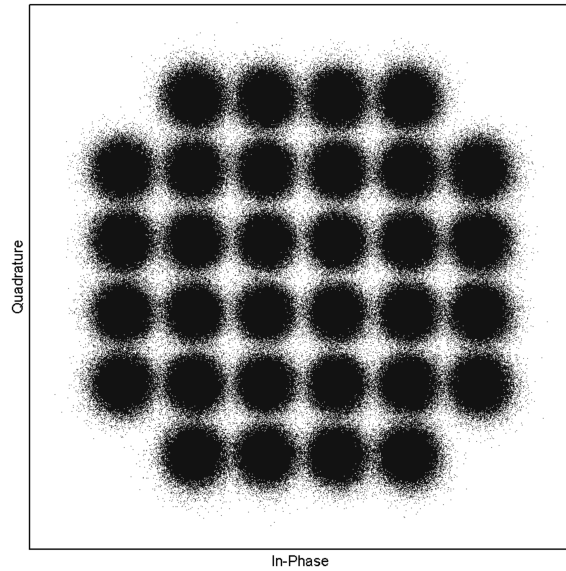
Figure 6.17: Superimposed received constellation diagram, containing results from all sub-carriers.

acceptable level.

By using 119 of the 128 subcarriers for data transmission (32-QAM), the aggregate transmission bit-rate equals 9.3 Gbit/s. After deduction of 3.9 % of cyclic prefix overhead and 7 % of FEC overhead, the net transmission bit rate is 8.3 Gbit/s. This is achieved using a transmission bandwidth of 2 GHz, with only low cost transceivers and SI-POF. The results demonstrate that DMT modulation is a promising solution for realization of 10 Gbit/s transmission over SI-POF.

6.1.4   Summary

In this section it was demonstrated that spectrally efficient multicarrier modulation schemes such as DMT can be used to compensate not only the bandwidth limitation of SI-POF, but also of SI-POF in combination with an LED-based transmitter. By making use of DMT, it was experimentally demonstrated that 993-Mbit/s transmission over 50 m of PMMA SI-POF is possible with an RC-LED as transmitter, achieved by combining the use of a simple passive high-pass filter and DMT modulation with adaptive QAM mapping of up to 64-QAM. Therefore, DMT is a promising solution for low-cost Gigabit transmission over SI-POF based on LED technology.

By using low-cost DVD laser diodes emitting visible red light at a wavelength of 655 nm, experiments demonstrated that up to 7.7 Gbit/s net data-rates can be achieved over 5 m of different large diameter ($\geq$ 0.5 mm) PMMA POFs, both step-index as well as graded-index. With digitally pre-equalized DMT, transmission rates of 8.3 Gbit/s can even be reached. The receiver used is a commercially available 0.8-mm diameter Si PIN photodiode. For such short distances, bandwidth limitation of transmitter and receiver dominate over that of the PMMA POF. Further improvements in transceiver bandwidth should be investigated in order to realize low-cost 10-Gbit/s transmission based on large-diameter PMMA POFs.

These results demonstrate the potential of low-cost PMMA-POF-based systems permitting bit-rates ranging from 1 Gbit/s to 8.3 Gbit/s at distances from 5 m up to 100 m. Together with their unique features (low-cost, robustness, easy handling, electromagnetic compatibility), the large diameter PMMA POF becomes a viable option for low-cost, high-speed applications in short-range optical communication networks.

6.2   Perfluorinated POF

In recent years, there has been increasing interest for using commercial perfluorinated graded-index plastic optical fiber (PF-GI-POF) for high-speed $\geq$10-Gb/s short-reach applications such as low-cost interconnects in data centers, local area networks (LAN), and supercomputers. For such applications, multimode fibers (MMF) are preferred above single-mode fiber (SMF) due to their large core diameter and numerical aperture. Especially the PF-GI-POF, available with core diameters of 50, 62.5, and 120 μm, is very attractive for such applications. Due to the large alignment tolerances in transceiver components and fiber splices, the PF-GI-POF is attractive for in-building networks as its installation is easy and low cost. In addition, when compared to silica MMF, PF-GI-POF offers further advantages such as smaller bending radius (5 mm), better tolerance to tensile load and stress, and simpler connectorization.

However, the large numerical aperture of PF-GI-POF also causes its bandwidth to decrease when compared to silica MMF and SMF. This section presents two experiments showing how DMT can be used to achieve bit-rates of 10 and 47 Gbit/s using standard commercially-available transceiver components made for conventional 10-Gbit/s on-off-keying operation. Using DMT, deployed systems can be upgraded to enable up to four or five-fold the initial transmission speed [25, 68].

6.2.1   10-Gbit/s DMT Transmission

Rapid increase of data traffic in data communication applications has pushed the demand for high-capacity and low-cost optical networks for use in LAN, such as enterprise or data center backbones. The use of 10 Gigabit Ethernet (10 GbE) in such cases will often require a new installation, because the commonly used CAT-5 copper cables are unsuitable for 10 GbE transmission over several tens of meters.

In this section, it is presented that only 2 GHz of bandwidth is needed for 10-Gbit/s transmission by using DMT [69]. This demonstrates the potential for larger cost reductions in optical 10 GbE, allowing the use of cheaper, low-bandwidth transceivers and large-area photodetectors in combination with large-core polymer optical fibers.
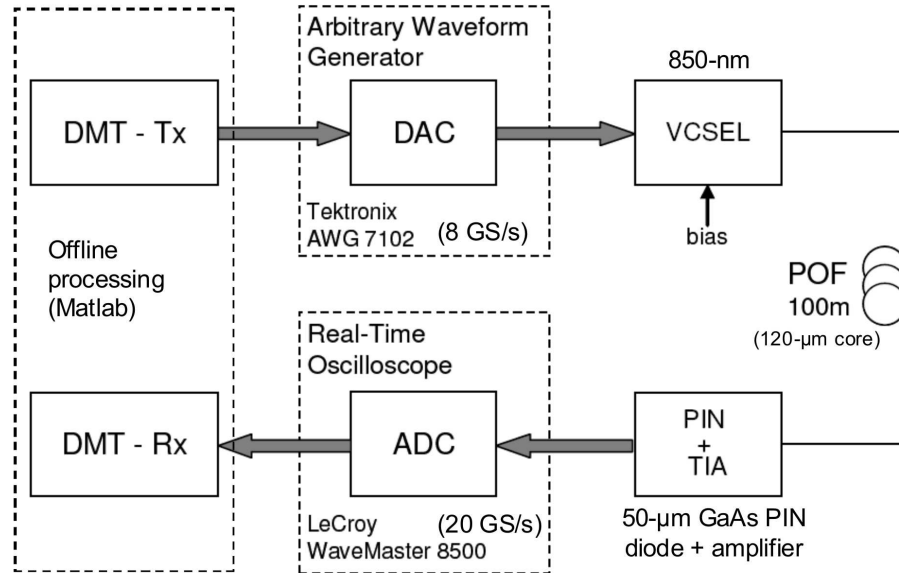
94

Figure 6.18: Schematic representation of the experimental setup for 10-Gbit/s DMT transmission over PF-GI-POF.

Experimental Setup

In Fig. 6.18, the experimental setup of the transmission system is shown. This is similar to the previous setup described in Section 6.1.3, except that an 850-nm multimode VCSEL and a GaAs PIN-detector with a silica multimode fiber pigtail with 50-μm core-diameter are used. Because the DMT signal bandwidth is the same as in Section 6.1.3, 512 subcarriers are used again for DMT transmission. Of the 512 subcarriers, only 508 are actually modulated with data. The first carrier at DC is not used at all while subcarrier number 64, 426, and 427 are switched off due to poor signal quality as a result of interference. Using a uniform 64-QAM mapping per subcarrier, a total capacity of $508 \cdot 6 = 3048$ bits per DMT frame is achieved. With an AWG sampling speed of 8 GS/s (four-fold oversampling), a DMT frame period of 256 ns is achieved, equaling to a total transmission speed of 3048 bits / 256 ns = 11.9 Gbit/s within a bandwidth of 2 GHz (see Fig. 6.19a).

For each DMT symbol, 3.3 % of cyclic prefix is added to increase the tolerance to inter-symbol interference. Similar to the case in Section 6.1.3, a combination of selective mapping and clipping is used to reduce the crest factor of the DMT signal. After deduction of the DMT transmission overhead and 7 % of FEC overhead,
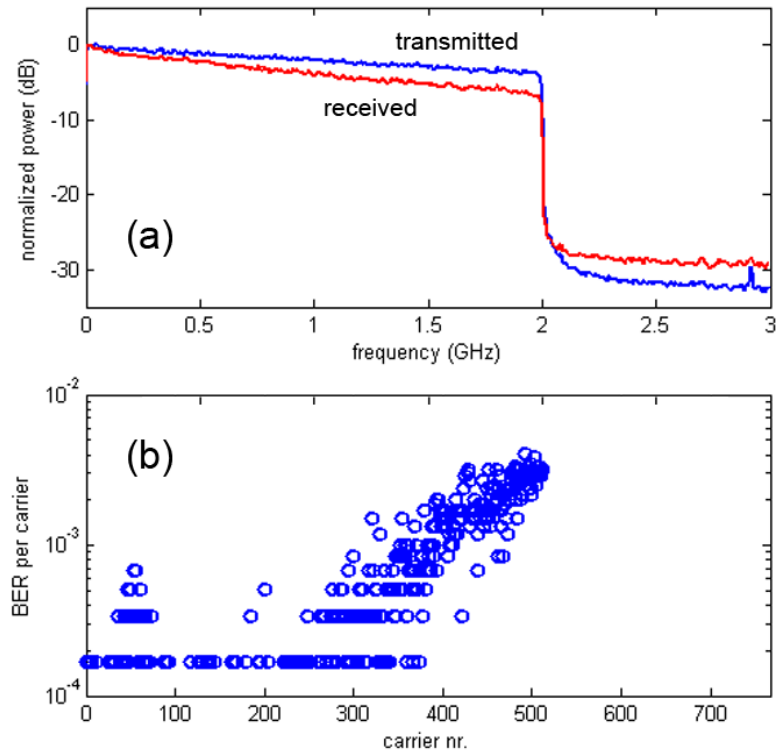
Figure 6.19: (a) Transmitted and received DMT signal spectra. (b) Measured BER for each subcarrier.

the net transmission bit-rate equals 10.6 Gbit/s. After transmission over 100 m of commercial PF-GI-POF with a core-diameter of 120 μm, the signal is received by a GaAs PIN-detector with trans-impedance amplifier. The received electrical signal is then captured at a sampling rate of 20 GS/s, and demodulated using offline processing.

Results

Fig. 6.19a shows the transmitted and received electrical DMT signal spectra. It can be seen that the -3 dB bandwidth of the system with PF-GI-POF is less than 1 GHz, emphasizing the potential of DMT. Fig. 6.19b shows the calculated BER per carrier for a total of 990 received DMT symbols, which equals a total of $3 \cdot 10^6$ bits. The total averaged BER of the received data is calculated to be $6.3 \cdot 10^{-4}$, resulting in values $< 10^{-9}$ if standard Reed-Solomon FEC with 7 % of overhead would be used.
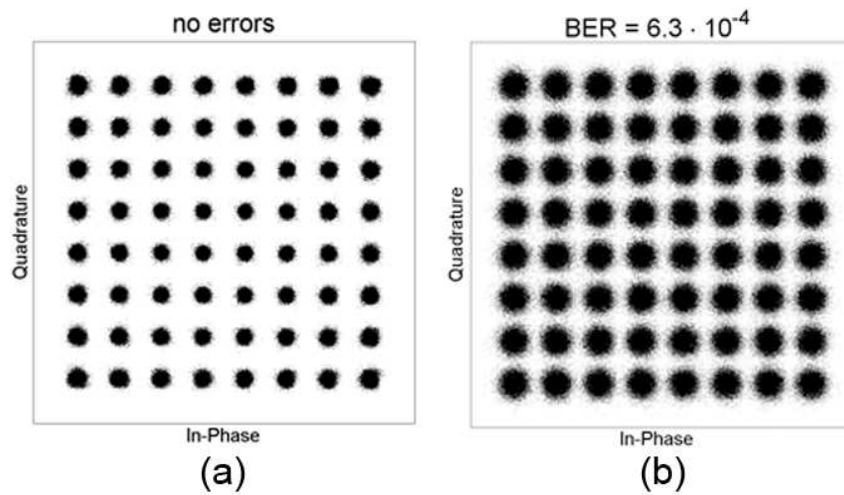
Figure 6.20: Superimposed received constellation diagrams of all 508 subcarriers (a) electrical back-to-back (b) after transmission over 100 m of PF-GI-POF.

In Fig. 6.20, the received and demodulated DMT symbols are shown for both the electrical back-to-back case and after transmission over 100 m of PF-GI-POF.

6.2.2 47-Gbit/s DMT Transmission

Recent developments in the standardization of higher-speed networking standards like 40 and 100 Gigabit Ethernet also include MMF as physical medium [70], thereby paving the way for low-cost optical networking at speeds beyond 10-Gbit/s. Although current proposals consider parallel transmission of multiple 10-Gbit/s MMF links with multiple fibers to achieve higher speeds, serial transmission using only one MMF is attractive because issues such as skew between parallel fibers, inter-channel crosstalk, and reduced reliability due to higher complexity can be avoided. Several research groups have demonstrated 40-Gbit/s serial transmission over GI-POF [71, 72, 73]. However, these results were obtained with expensive large-bandwidth (>25 GHz) single-mode fiber components such as external Mach-Zehnder modulators and small-area high-bandwidth detectors [72, 73], as well as optical fiber amplifiers [71], which are neither practical nor suitable for low-cost applications.

The experiment in this section demonstrates that by exploiting DMT with up to 64-state quadrature amplitude modulation (64-QAM), off-the-shelf and low-cost components such as standard 1300-nm directly-modulated distributed feedback (DFB) laser diode (with 12-GHz bandwidth) and an MMF-coupled 25-μm large diameter photodetector can be used to achieve more than 40-Gbit/s serial transmission over 100 m of 50-μm core diameter PF-GI-POF [74]. This demonstrates the potential of DMT for enabling highly spectral efficient transmission at high bit-rates over MMF, while overcoming the fiber's modal dispersion and allowing the use of conventional low-bandwidth transceivers [75, 76, 66]. It is therefore a promising solution for low-cost, robust, and high-capacity MMF and PF-GI-POF LAN links operating at data rates of 40 Gbit/s and beyond.

Experimental Setup

In order to realize 40-Gb/s transmission over PF-GI-POF, different system parameters have to be investigated and optimized. For this, the experimental setup depicted in Fig. 6.21 is used. Using an AWG (Tektronix AWG7122B) with a bandwidth of 10 GHz, a DFB laser is directly modulated (through an electrical variable attenuator and amplifier) at a sampling speed of 24 GS/s. To achieve this sampling speed, the two outputs of the AWG, both at 12 GS/s, are interleaved. The DFB laser, with a
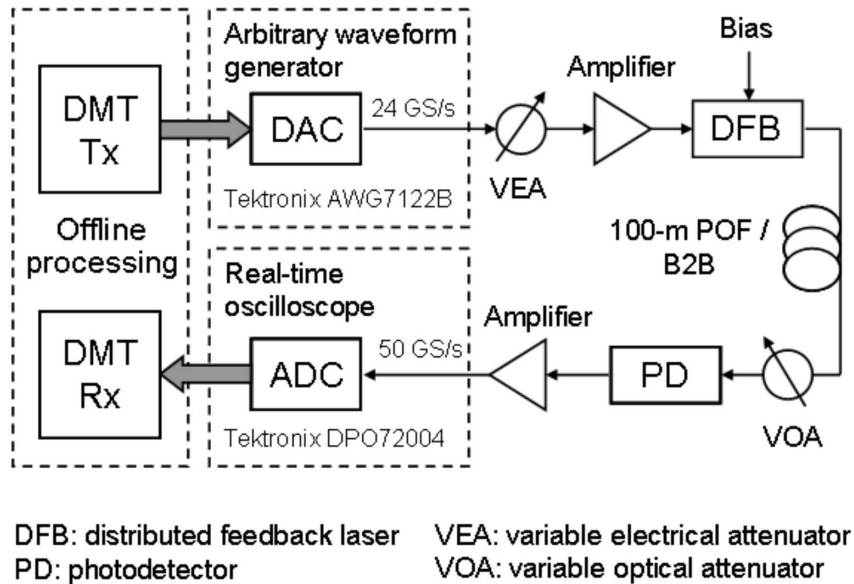
Figure 6.21: Measurement setup for DMT over PF-GI-POF transmission.

wavelength of 1302 nm, is specified for up to 10-Gbit/s on-off keying transmission and has an electrical small-signal modulation bandwidth of approximately 12 GHz. The resulting intensity-modulated optical signal is then either transmitted over 100 meters of 50-μm core perfluorinated PF-GI-POF, or directly coupled to the multimode variable optical attenuator in the back-to-back measurement case. After the multimode attenuator, the received optical signal is detected by a multimode-fiber-coupled photo-detector (PD) with a detection diameter of 25-μm and an integrated coupling lens. The resulting received electrical signal is then amplified and captured using a 16-GHz real-time Tektronix DPO72004 digital storage oscilloscope (DSO) running at a sampling rate of 50 GS/s for demodulation and evaluation.

For the DMT transmission, a computer is used to emulate the digital DMT modulator and demodulator, as shown in Fig. 6.21. This also includes evaluation of transmission performance parameters such as BER and SNR per subcarrier, and the computation of the bit-loading algorithm.

Influence of Laser Non-Linearity

The parameters of the DMT signal used for the laser non-linearity measurements are given in Table 6.1. It should be noted that the DMT signal is clipped in the
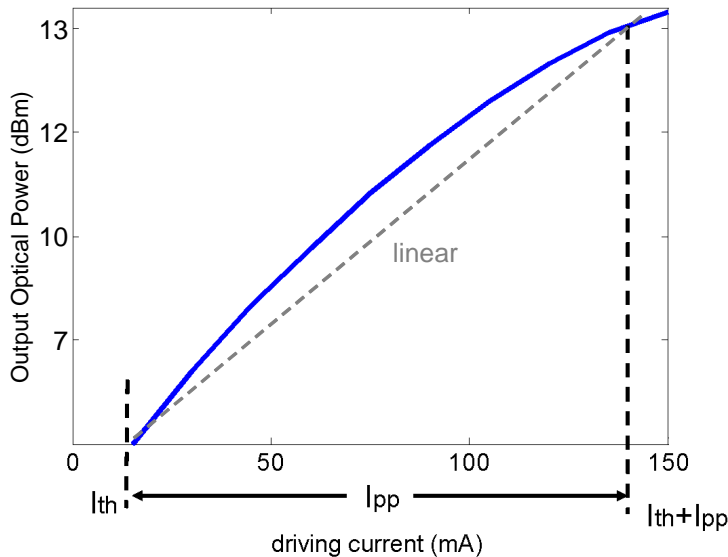
Figure 6.22: Measured static optical output power vs. static driving current for DFB laser used in the experiments. I_{th}: threshold current, I_{pp}: peak-to-peak driving current.

Table 6.1: DMT transmission signal parameters.

Nr. of subcarriers:	256 (254 used, first and last not used at all)
FFT points:	512
Cyclic prefix:	8 per 512 points
Preambles:	4 preambles per 200 DMT frames
DMT signal crest factor:	3.2 (limited by clipping)

electrical digital domain before D/A conversion due to reasons of dynamic range [29, 25]. As a result of this digital clipping, the analogue current I_{pp} after D/A conversion for driving the DFB laser will have a maximum clipping-limited crest factor μ as defined in (4.31). In [29] and [25], the optimum peak-to-average power ratio (PAPR) for DMT in an MMF channel was already investigated and found to be approximately 10 dB, which corresponds to a crest factor $\mu = 3.2$. Therefore, this value will be used for all measurements presented in this section.

Initially, all subcarriers are loaded with 3 information bits each, corresponding to a modulation format of 8-QAM. From the received and demodulated DMT signal, the SNR per subcarrier is estimated and used to compute bit-loading in or-
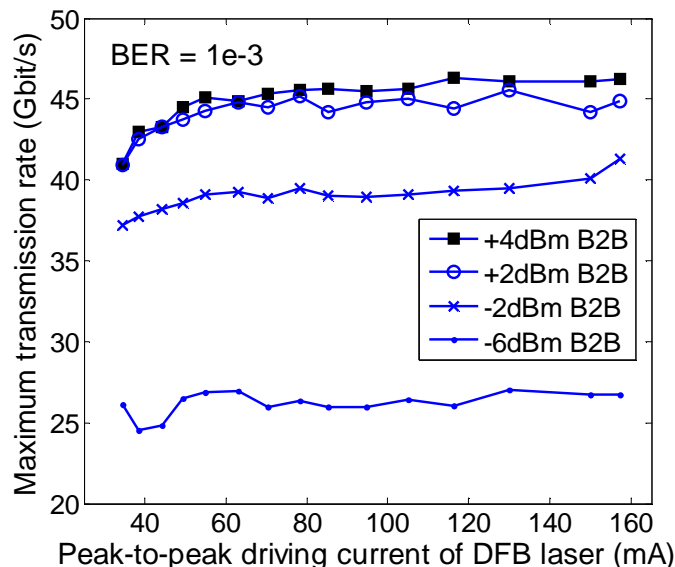
Figure 6.23: Maximum achievable transmission rate at BER $= 1 \cdot 10^{-3}$ for different peak-to-peak laser drive current I_{pp} and at different received optical powers.

der to maximize transmission performance. Due to the use of Chow's rate-adaptive bit-loading [48] in this experiment, system performance is characterized by the maximum achievable transmission rate at a fixed BER of $1 \cdot 10^{-3}$. It should be noted that all maximum transmission rates plotted are net transmission rates, after deduction of all DMT transmission overhead (cyclic prefix and preambles) including the standard 7 % of FEC overhead.

Fig. 6.22 shows schematically how the peak-to-peak driving current I_{pp} is varied for the DFB laser used in the experiment. The laser is always fully modulated starting from its threshold current I_{th}. The laser bias current, which is equal to $I_{pp}/2 + I_{th}$, is adjusted according to I_{pp} in order to ensure full modulation of the DFB laser. The mean received optical power is fixed to the same value with the variable optical attenuator when I_{pp} is increased. By this method, the influence of thermal noise (resulting mainly from the electrical amplifier at the receiver) is kept constant when I_{pp} is varied.

From the back-to-back measurement results of Fig. 6.23, notice that for a fixed driving current, the system performance increases for larger values of received optical power, which is apparent due to less influence of receiver (thermal) noise. However,

101

at +4 dBm received optical power, performance seems to be limited and the achievable transmission rate seems to saturate at its maximum value. Possible reasons for this limit are saturation effects of the photodetector at high received optical powers and the electrical DMT clipping noise resulting from clipping the electrical DMT signal in the digital domain before D/A conversion. Clipping is essential to limit the peak power of DMT signals because constructive phase addition of a large number of subcarriers can cause very high signal peaks, as discussed in Chapter 4.3.

It can also be observed that the maximum transmission rate saturates for increasing peak-to-peak driving current. The expected deterioration of transmission rate for increasing peak-to-peak driving current due to non-linearity in the electrical to optical power conversion is not observed. A possible reason for this is that non-linearity in the current to optical power conversion occurs mainly due to saturation effects because insufficient holes and electrons are able to recombine in a timely manner. This however, is a rather slow process and is more evident when periodic (or low crest factor) modulation signals are applied.

DMT, however, is characterized by large crest factor values. As a result of infrequent and irregular peaks, saturation effects are less likely to occur because sufficient holes and electrons are often present for recombination. Therefore, non-linearity issues in the electrical to optical conversion process of the laser are less pronounced. A more detailed description of this is given in Chapter 5.3.

The results from transmission experiments over 100 m PF-GI-POF is investigated and shown in Fig. 6.24. The corresponding back-to-back curves in Fig. 6.23 are included for reference. The maximum achievable bit-rate decreases for larger peak-to-peak laser drive currents in the case of transmission over 100 m PF-GI-POF. The reduced transmission rate can be attributed to the change in the shape of the frequency response at higher laser currents, as shown in Fig. 6.25. This can be attributed to differential modal attenuation (DMA) [77, 78], which is the effect that higher-order modes propagating through the GI-POF experience higher attenuation than the fundamental modes. At low peak-to-peak drive currents (and therefore low bias current) resulting in a low launch power, almost only the fundamental modes can be detected after 100 m GI-POF due to the DMA effect. However, for very high optical launch powers, the higher order modes are not attenuated enough at a distance of 100 m and are therefore also detected at the end of the GI-POF.

Figure 6.24: Maximum achievable transmission rate at BER $= 1 \cdot 10^{-3}$ for different peak-to-peak laser drive current I_{pp} and received optical powers with PF-GI-POF.

Figure 6.25: Measured frequency response of 100 m PF-GI-POF (without DMT modulation) at 60 and 80 mA laser bias current.

This difference in mode attenuation profile leads to constructive/destructive modal interference, and affects in this case the GI-POF bandwidth in a negative way (as can be observed in Fig. 6.25).
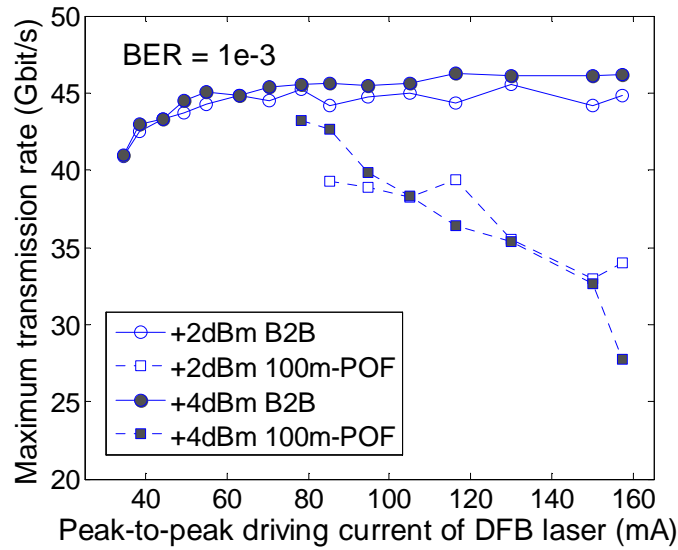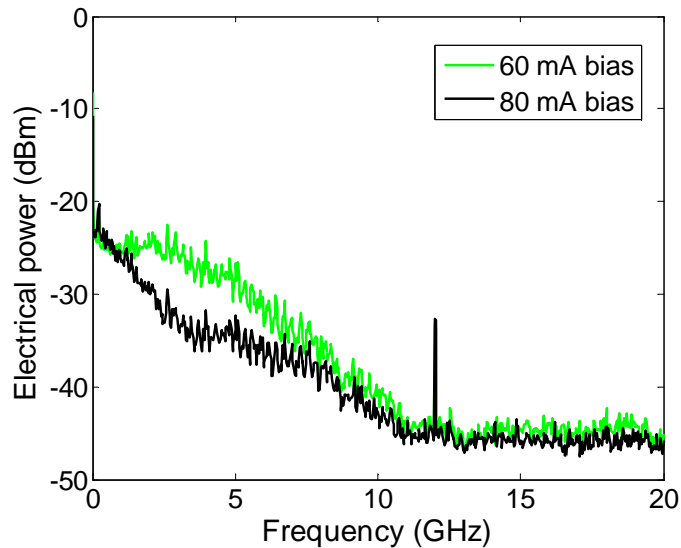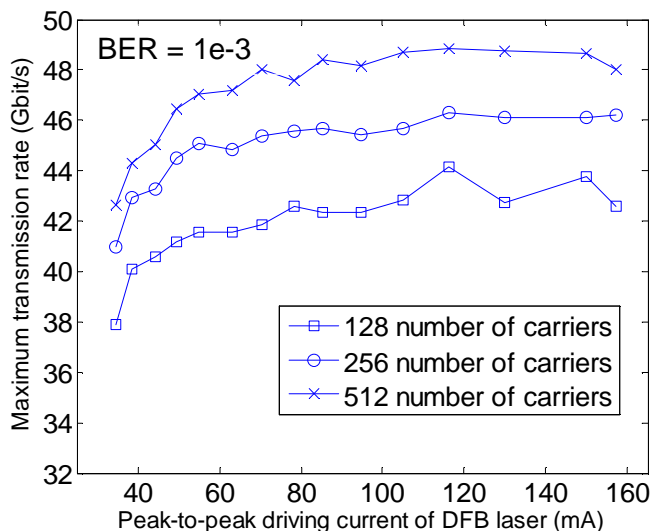
Figure 6.26: Maximum achievable transmission rate at BER $= 1 \cdot 10^{-3}$ for different peak-to-peak laser drive current I_{pp} and number of subcarriers. Cyclic prefix length is fixed to 8.

Additionally, the limitation due to clipping noise and saturation effects of the photodetector can be noticed again in the curves with 100 m PF-GI-POF as no significant improvement in transmission rate is observed between $+2$ dBm and $+4$ dBm.

Influence of Number of Subcarriers

In addition to the impact of laser non-linearity, the influence of the number of subcarriers used for DMT transmission is also investigated experimentally. The same DMT transmission parameters as in Table 6.1 are used, except that the total number of subcarriers is now varied from 128 to 512 (with a fixed cyclic prefix of 8). The received optical power is fixed at $+4$ dBm. Again, with rate-adaptive bit-loading, the power and bit-allocation per subcarrier is adapted to the transmission channel, thereby maximizing the transmission rate to a fixed BER of $1 \cdot 10^{-3}$.

Fig. 6.26 shows the experimental results for the back-to-back case without PF-GI-POF. As observed in Fig. 6.26, the system performance improves when the number of subcarriers used for DMT transmission is increased. To further investigate this, the total number of DMT subcarriers is varied over a larger range at the same
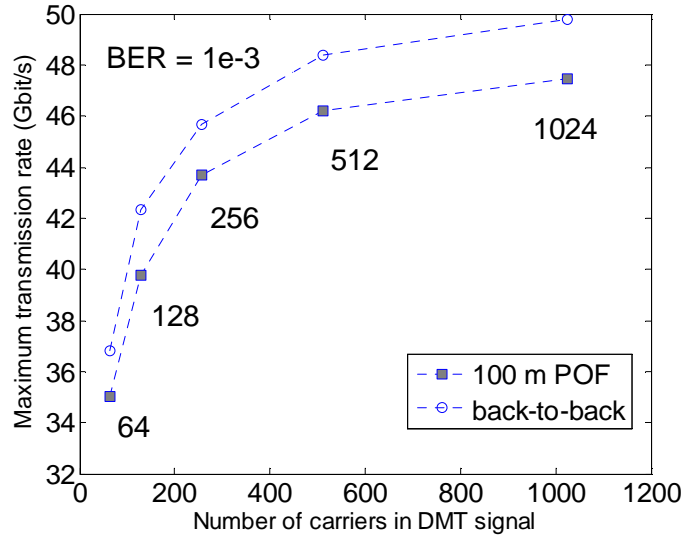
Figure 6.27: Maximum achievable transmission rate at BER $= 1 \cdot 10^{-3}$ for different number of subcarriers. Received optical power is fixed at $+4$ dBm and cyclic prefix length is fixed to 8.

received optical power of $+4$ dBm and the peak-to-peak driving current I_{pp} of the DFB laser is fixed to 85 mA. The measurement results are plotted in Fig. 6.27, for the case of back-to-back and 100 m of PF-GI-POF.

Shown in Fig. 6.27 is the transmission performance improving with the increase in the number of subcarriers used for DMT. This is true for both back-to-back transmission and with 100 m of PF-GI-POF. The most probable conclusion is that with a larger number of subcarriers, the frequency response of the transmission channel can be divided into a larger amount of finer subchannels, making the channel response of each subcarrier flatter. Consequently, every subcarrier experiences a better channel response and performance increases.

The performance gap between 100 m PF-GI-POF and the back-to-back case is due to the extra bandwidth limitation of the PF-GI-POF. The attenuation of PF-GI-POF is not significant in Fig. 6.27 because the received optical power and peak-to-peak laser driving current are both fixed to the same values for all measurements. It can also be noticed that the number of subcarriers cannot be increased infinitely to increase transmission performance, as this already shows signs of saturation at a value of 1024 subcarriers. In conclusion, a net transmission bit-rate of 47 Gbit/s is

achieved over 100 m of PF-GI-POF using DMT based on a total of 1024 subcarriers.

Influence of Modal Noise

Up to an I_{pp} of 85 mA, modal noise is not observed. This is because light of a single-mode DFB laser with single mode pigtail (small launching area) is launched into the GI-POF, thereby exciting only lower order modes. Due to mode coupling in the GI-POF, higher order modes can still exist but most are suppressed by DMA. Additionally, a commercial photodetector with integrated coupling lens is used to couple most of the light from the end of the GI-POF into the detector. (The effective detector diameter is 21 μm.) For I_{pp} larger than 85 mA, beginning signs of modal noise can be observed, because of high laser launch power. Due to such high launching power (up to +10 dBm), DMA in the GI-POF is not large enough to suppress the higher order modes resulting from mode coupling in the GI-POF. Therefore, higher-order modes are present at the GI-POF end-face and some are not detected by the photodetector, leading to beginning signs of modal noise. As the results are obtained at I_{pp} of 85 mA, these results do not suffer from modal noise.

47-Gbit/s Transmission over 100 m PF-GI-POF

In this section, details of the transmission performance of DMT for a net bit-rate of 47 Gbit/s over 100 m PF-GI-POF are presented. In the experiment, 1024 subcarriers are used for the DMT transmission, ranging from a frequency of 0 to 12 GHz. Fig. 6.28a shows the measured SNR per subcarrier in the initialization stage, prior to applying Chow's rate-adaptive bit-loading algorithm, after transmission over 100 m PF-GI-POF. The channel response is clearly adapted by the large amount of subcarriers in detail. The bit and power allocation per subcarrier, after applying rate-adaptive bit-loading, is depicted in Fig. 6.29. For subcarriers with the highest SNR, 6 bits are allocated for DMT transmission, which is realized by 64-QAM. The number of allocated bits per subcarrier decreases to 2, for those subcarriers with the lowest SNR. This is equivalent to a modulation format of 4-QAM. By allocating a different amount of power to each individual subcarrier, the SNR per subcarrier can be fine-tuned to a fixed value, which is just enough to achieve a BER of $1 \cdot 10^{-3}$ for the specific modulation format.
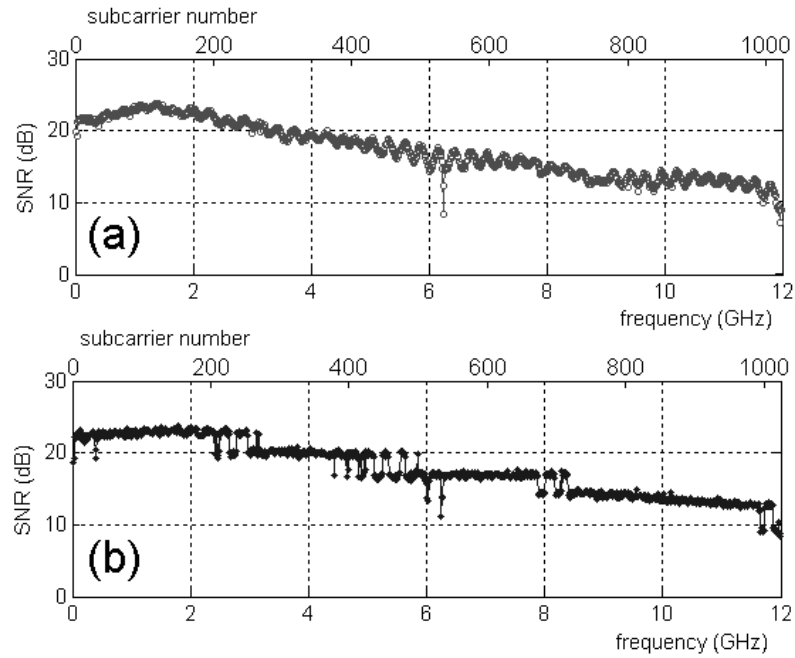
Figure 6.28: Measured SNR per subcarrier for DMT transmission over 100 m PF-GI-POF, (a) before (b) after rate-adaptive bit-loading.
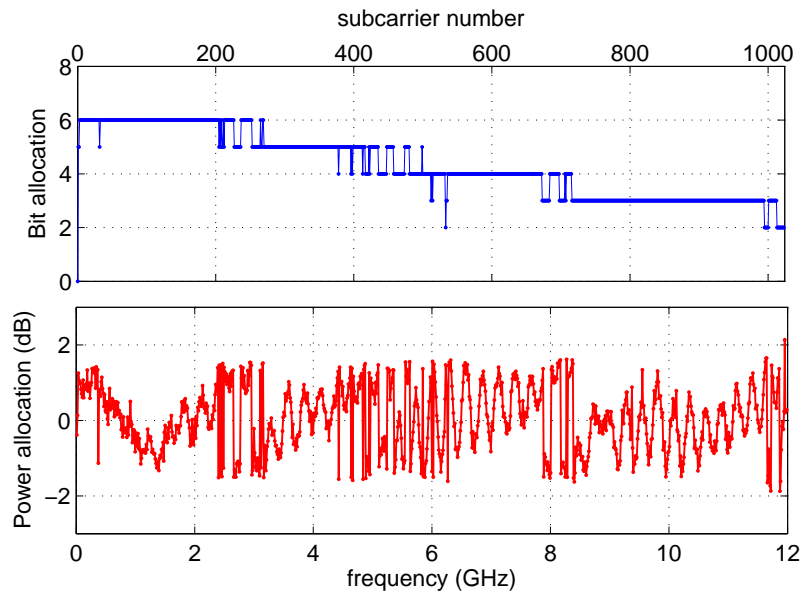

Figure 6.29: Chow's rate-adaptive bit-loading [48] parameters for DMT transmission over 100 m PF-GI-POF using a total of 1024 subcarriers.
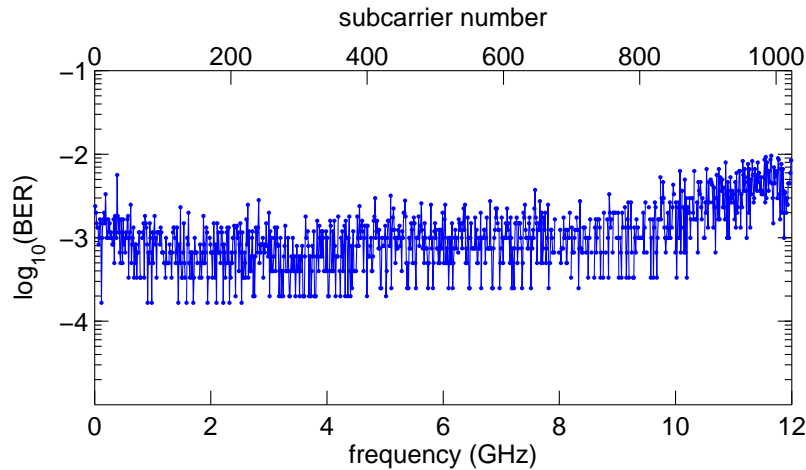
107

Figure 6.30: Measured and evaluated BER performance per subcarrier after DMT transmission over 100 m PF-GI-POF.

The resulting SNR per subcarrier after rate-adaptive bit-loading is shown in Fig. 6.28b. Notice that the SNR per subcarrier is stair-case-shaped, as a result of the bit-loading algorithm. A total of 4421 bits are allocated per DMT frame. Fig. 6.30 presents the measured BER values as a function of the subcarrier index for the received 47 Gbit/s DMT signal. In the DMT transmission scheme, the signal is not demodulated per subcarrier but as an entire frame. This provides the benefit that even if some subcarriers have BER values larger than $1 \cdot 10^{-3}$, the signal quality is still good enough to achieve a total average BER of $1 \cdot 10^{-3}$. This value is under the FEC limit for reliable operation. Notice from Fig. 6.30 that the individual subcarrier BER values are higher than $1 \cdot 10^{-3}$ at higher frequencies. This however, corresponds to a low number of bits allocated per subcarrier. Therefore, the total average BER can still be $1 \cdot 10^{-3}$ because the majority of transmitted bits are allocated to frequencies closer to 0 Hz.

In Fig. 6.31, the electrical spectra of the signal as observed before and after 100-m transmission are depicted. The available bandwidth for data transmission is seen as less than 12 GHz, taking into account the bandwidth of the AWG and the DFB laser. However, the DMT scheme and the bit-loading algorithm allow us to successfully transmit 47-Gbit/s data through such narrow bandwidths. Additionally, the spectrum without data modulation which indicates the noise floor of the system is also depicted.
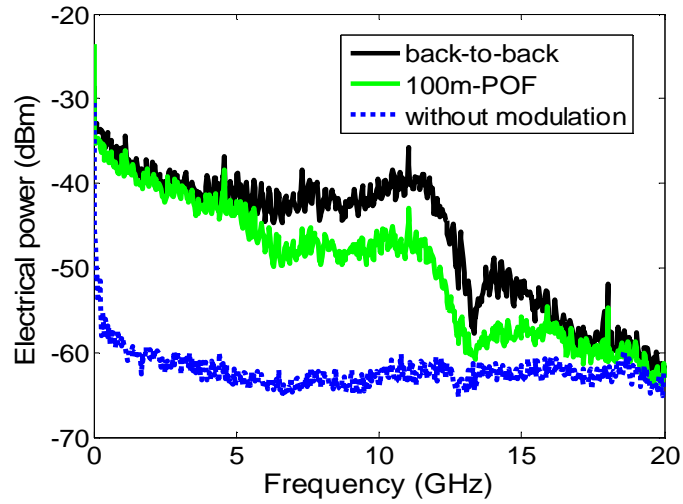
Figure 6.31: Received DMT signal spectrum after 100 m PF-GI-POF, compared with back-to-back transmission and spectrum without modulation.
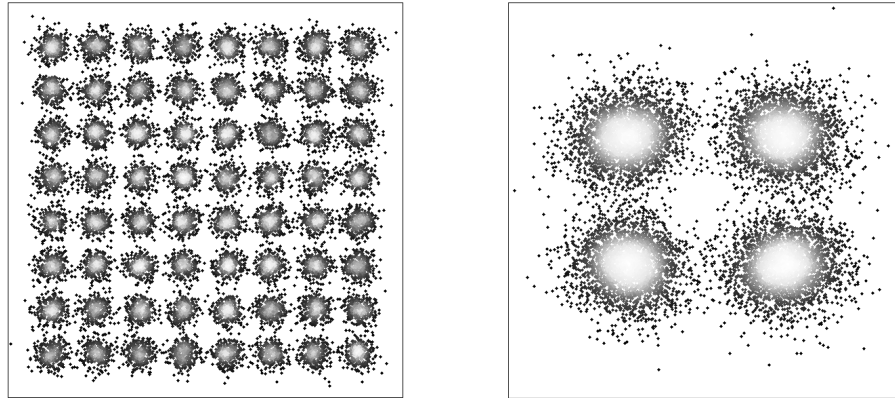
Figure 6.32: Plots of the highest (64-QAM) and lowest (4-QAM) constellations used in 47-Gbit/s DMT transmission over 100 m PF-GI-POF.

In Fig. 6.32, the superimposed constellation diagrams of the first 20 subcarriers with 64-QAM and the last 10 subcarriers with 4-QAM are shown. These constellations are respectively the largest and smallest of the DMT transmission system over 100 m PF-GI-POF. The clearly distinguishable constellation points indicate that the received signal quality is sufficiently good and that the one-tap channel equalizers in the DMT demodulator are working as expected.

6.2.3 Summary

First DMT experiments over PF-GI-POF (120 μm core diameter) demonstrated that 10.6-Gbit/s transmission is easily achievable over a distance of 100 m. This was accomplished by direct modulation of an 850-nm multimode VCSEL and direct detection with an MMF-coupled receiver, using a uniform 64-QAM mapping within a bandwidth of 2 GHz.

By characterizing the influence of laser current to optical power non-linearity and the number of subcarriers on DMT transmission performance over PF-GI-POF using experimental results, optimum parameters for best system performance were determined. The maximum achievable transmission rate with optimum transmission parameters is improved to 47-Gbit/s over 100 m PF-GI-POF (50 μm core diameter), using only a bandwidth of 12 GHz. Instead of uniform QAM constellations for all subcarriers, Chow's rate-adaptive bit-loading algorithm (described in Chapter 3.6) is now exploited with DMT transmission. This indicates that DMT can also be a promising solution for enabling high-capacity serial transmission of 40 Gbit/s and beyond over MMF and PF-GI-POF links.

Although current 40 and 100 Gigabit Ethernet proposals regard only parallel transmission of multiple 10-Gbit/s links in order to achieve higher speeds, the proposed idea of serial transmission at similar bandwidth requirements by use of DMT can result in even lower-cost systems. While one might argue that digital signal processing will increase power consumption, significant power savings resulting from using less transceivers and the inherently reduced complexity can offer a good trade-off to make DMT a viable solution for high-speed, low-power, and low-cost serial optical networking operating at bit-rates of 40 Gbit/s and beyond. Moreover, DMT has proven to be a robust technique to adaptively compensate the modal dispersion of multimode PF-GI-POF links, and in this way counteracting the dispersion variations which may occur due to changing fiber launching and bending conditions.

6.3 Silica Multimode Fiber

Next to POF, silica mulitmode fiber (MMF) with core diameters of 50 and 62.5 μm are attractive for use as high-capacity and low-cost optical fiber-based links in local area networks (LAN), such as enterprise in-building and datacenter backbones, but also short-distance server/computer interconnects. Nowadays, silica MMF is used for the vast majority of the optical LAN links [18]. This is due to the large core diameter of the MMF, which allows large alignment and dimensional tolerances in transceiver components, thereby lowering installation, maintenance, and component costs. Therefore, high-speed networking standards like Gigabit Ethernet, Fiber Channel, 10 Gigabit Ethernet, and 40/100 Gigabit Ethernet all include the silica MMF as a transmission medium. Additionally, silica MMF has attenuation values of typically 1 to 3.5 dB/km, which is lower than that of POF. This makes the silica MMF attractive for distances up to a few kilometers.

With the further growth of bandwidth-intensive applications like IPTV and HDTV as well as data processing in the medical industry, a further increase of the capacity in LAN backbones and server interconnects has to be considered. Investigations on transmission speeds higher than 10 Gbit/s over MMF have already been reported [79, 80, 81, 82, 83, 84], but these are either based on novel high-bandwidth components (29 GHz) and external modulation [79, 80, 81] or the use of single mode components [82, 83, 84], which is not practical and can cause modal noise due to spatial filtering.

In this section, experiments showing two applications of DMT over silica MMF are presented. The first experiment demonstrates how DMT is used to combat modal dispersion in such fibers. Additionally, by using highly spectral-efficient quadrature amplitude modulation (QAM), the available bandwidth can be used efficiently, allowing the use of conventional low-bandwidth transceivers to achieve up to 24-Gbit/s DMT transmission. The second experiment deals with relative intensity noise (RIN) [85, 86, 87], which is often present in low-cost multimode vertical cavity surface emitting lasers (VCSELs) used in short-reach optical applications. In this experiment, it is demonstrated how DMT with bit-loading can be used to adapt to the frequency-dependent RIN, enabling optimum performance up to 30 Gbit/s with a low-cost multimode VCSEL.

6.3.1   24-Gbit/s DMT Transmission

Until recently, the problem of arrival time delays due to multiple paths traversed by different modes (modal dispersion) in MMF was a major limiting factor for 10-Gbit/s transmission at distances up to 300 m. In 2001, the OM3 type silica MMF was introduced and made it possible to reliably support 10-Gbit/s transmission over 300 m of MMF. Recent advances have even resulted in OM4 type MMF in 2008, where 10-Gbit/s transmission is possible for distances of 500 m and beyond.

However, even though the OM4 MMF has enough bandwidth (5 GHz·km at 850 nm) to support data rates higher than 10 Gbit/s over a few hundred meters, the limiting factor nowadays are the transceiver components. Due to cost reasons, high-speed >10-Gbit/s transceivers are not commercially viable for short-reach applications. Therefore, it is a big challenge to support bit-rates beyond 10 Gbit/s for short-reach optical communications at reasonable costs.

The experiment presented here demonstrates the possibility of 24-Gbit/s DMT transmission over 730 m of OM-3 silica MMF using direct modulation of a commercial 850-nm multimode vertical cavity surface emitting laser (VCSEL) and direct detection with a standard multimode PIN photodetector [66]. By using 730 m of OM-3 type MMF, it is shown that DMT can compensate for modal dispersion of the fiber. Additionally, the use of a commercial VCSEL and photodetector (both designed for 10-Gbit/s binary transmission) proves that highly spectral-efficient DMT transmission can make use of conventional transceivers for enabling bit-rates beyond 10 Gbit/s.

Experimental setup

Fig. 6.33 shows the experimental setup of the transmission system, which is similar to the ones presented in Sections 6.1.3, 6.2.1, and 6.2.2. A total of 512 carriers are used for the DMT transmission, corresponding to an IFFT-length of 1024. 3.125 % of cyclic prefix is used, corresponding to a length of 32 points. Of the 512 subcarriers, the last subcarrier ($n = 511$) is used as a pilot tone while the first subcarrier ($n = 0$) at 0 Hz is not used at all. The pilot tone is necessary because of the use of selective mapping (as described in Section 6.1.3) to decrease the DMT signal's crest factor. Additionally, the digital DMT waveform is clipped to obtain a crest factor μ of 2.8
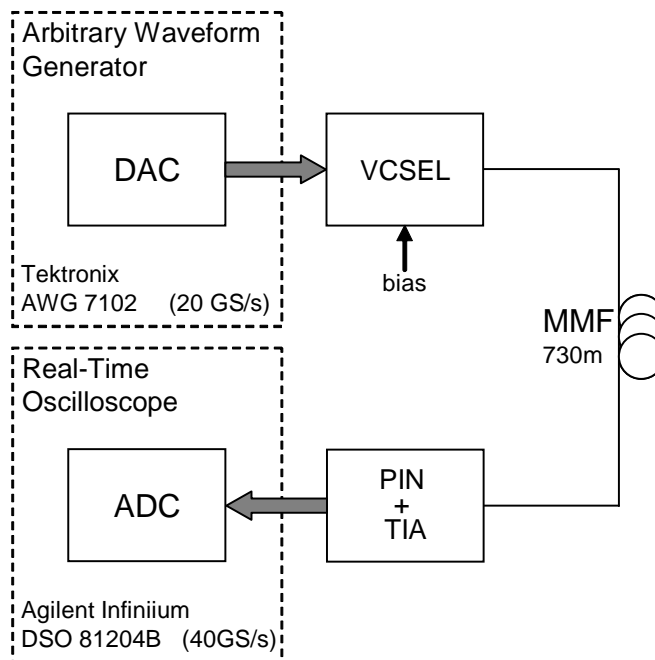
Figure 6.33: Experimental setup. DAC: digital-to-analog converter; ADC: analog-to-digital converter; PIN + TIA: MMF-coupled PIN photodiode with trans-impedance amplifier.

(see equation (4.31)) before being generated by the D/A converter. Phase offset and amplitude estimation is done by means of a known pilot frame, transmitted once every 100 DMT frames.

The software-generated DMT transmit sequence, which is stored in the memory of the AWG, is output at a four-fold oversampling speed of 20 GS/s and a resolution of 10 bits. By using adaptive QAM-mapping ranging from 16-QAM to 64-QAM, transmission parameters are adapted to the SNR of the MMF channel as depicted in Fig. 6.34. Note that this adaptive QAM-mapping, which is optimized manually, is a simple version of the more sophisticated bit-loading algorithm described in Chapter 3.6. In total, 110 subcarriers are modulated with 64-QAM, 200 with 32-QAM, and the final 200 with 16-QAM, corresponding to a capacity of 2460 bits per DMT frame. With a transmit time of 102 ns per DMT frame (2048 points per frame at 20 GS/s), a transmission speed of 2460 bits / 102 ns = 24.1 Gbit/s is achieved in a transmission bandwidth of only 5 GHz (see Fig. 6.35). With deduction of 3.125 % of cyclic prefix, 7 % of standard FEC overhead, and 1 % of preambles, the net
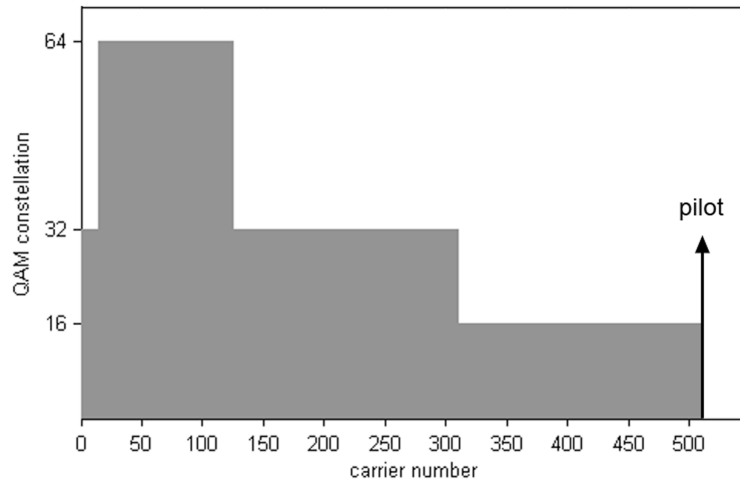
Figure 6.34: Adaptive QAM constellation mapping per subcarrier and location of pilot tone at the last subcarrier.
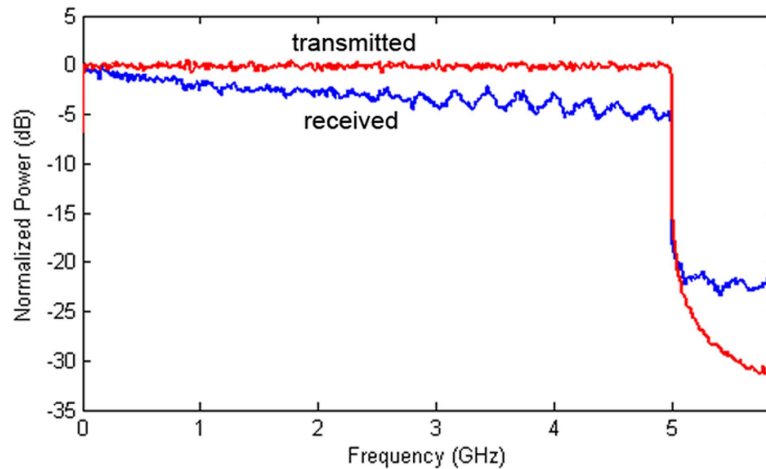
Figure 6.35: Transmitted and received (after 730 m of MMF) electrical DMT signal spectra.

transmission bit-rate equals 21.6 Gbit/s. In total, 2500 DMT frames are loaded in the AWG and output cyclically.

This output signal is then used to directly modulate a commercial 850 nm multimode VCSEL. The measured optical spectrum of the VCSEL is depicted in Fig. 6.36. It can be seen that the VCSEL has a typical broad optical spectrum which is larger than 1 nm. With a mean optical power of -3.2 dBm, the output light from the VCSEL is launched into 730 m of high quality OM3 graded-index multimode fiber

Figure 6.36: Measured optical spectrum of VCSEL used in transmission experiment with 0.05 nm resolution bandwidth.

with a core diameter of 50 μm.

The signal after transmission (-4.5 dBm mean received optical power) is received by an MMF PIN-detector with a trans-impedance amplifier. The frequency response of the transmission system is shown in Fig. 6.37. The received electrical signal 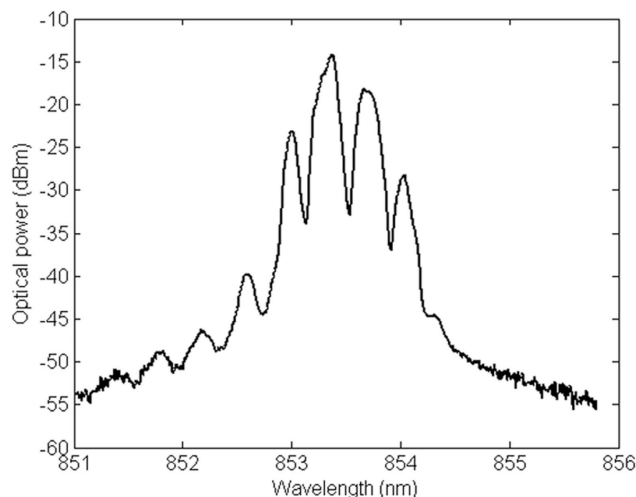from the photodetector is captured by an Agilent Infiniium DSO 81204B real-time digital storage oscilloscope with an A/D converter of 8 bits resolution and a sampling rate of 40 GS/s, corresponding to a sampling rate of four-fold the Nyquist frequency. A software implementation of a DMT receiver is then used to demodulate the captured DMT time signal. Finally, the demodulated data sequence is compared to the sent sequence and the BER is evaluated.

Results

Fig. 6.35 shows the transmitted and received electrical DMT spectra for the IM/DD transmission system with 730 m of silica MMF. It should be noted that although the frequency response of the system (see Fig. 6.37) deteriorates rapidly for frequencies beyond 3 GHz, DMT transmission is nevertheless possible. In a typical baseband transmission system using on-off-keying modulation, it would have been impossible
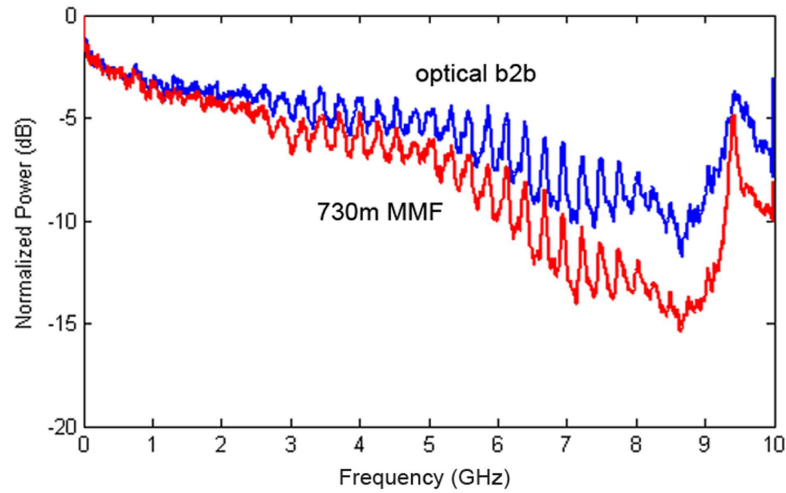
Figure 6.37: Frequency response of the transmission system for the optical back-to back case and with 730 m of MMF.
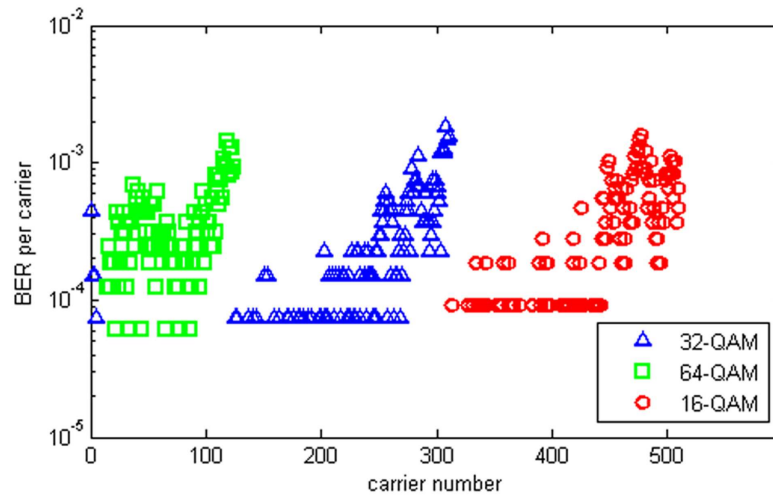
Figure 6.38: Measured bit-error ratio of each individual subcarrier. No errors are detected at those subcarriers where no markers are depicted. In total, 510 subcarriers are used for data transmission.

to achieve such high data rates of up to 24 Gbit/s over a channel with such a frequency response. The poor frequency response of the system is due to the hardware used in the experiment.

In Fig. 6.38, the calculated BER values per subcarrier are depicted for a total of 2700 received DMT frames, which equal $6.6 \cdot 10^6$ bits. The influence of adaptive

116
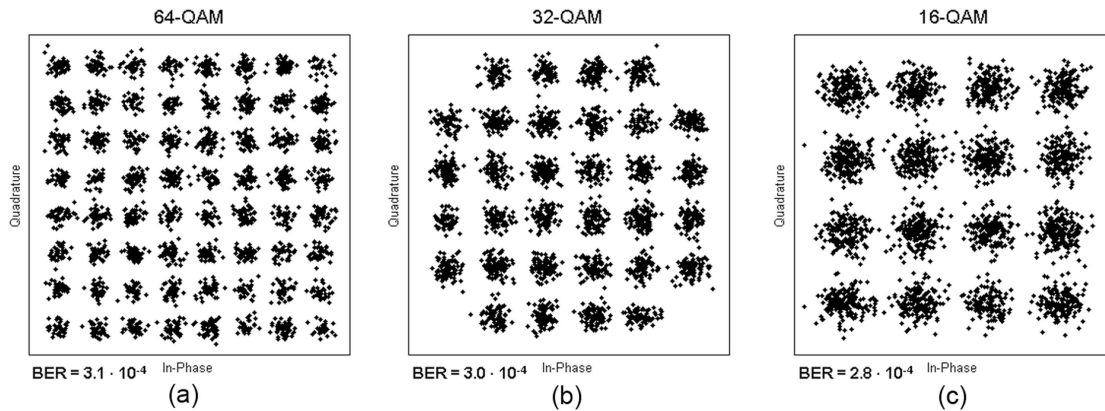
Figure 6.39: Received constellation diagrams after DMT demodulation for (a) subcarrier nr. 64 (b) subcarrier nr. 250 (c) subcarrier nr. 447.

QAM constellation mapping can clearly be seen from the figure. The BER values per subcarrier drop steeply to a lower level after transition from a higher order QAM mapping to a lower order one. The total averaged BER from all 510 subcarriers and is calculated to be $2.6 \cdot 10^{-4}$, which, by making use of standard Reed-Solomon (255,239) FEC code, will reduce to $< 10^{-10}$. As an indication of the received signal quality, the received and demodulated DMT frames are shown for subcarriers n = 64, 250, and 447 in Fig. 6.39, with BER values of approximately $3 \cdot 10^{-4}$. The constellations can be clearly recognized.

6.3.2 DMT and Relative Intensity Noise

Multimode VCSEL and Modal Noise in MMF

When mode selective losses such as poor connectors or splitters, misaligned fiber joints, or poor coupling from fiber to photodiode occur in an MMF link, the use of coherent lasers is known to cause modal noise, resulting in a BER penalty [88]. When coherent light is launched into an MMF, a speckle pattern is created at the fiber end-face that is caused by the interference of the different modes traversing in the MMF [89]. The time-fluctuating behavior of the speckle pattern in the presence of mode selective loss in the optical link causes a power variation in the received signal and a corresponding BER penalty [90, 91]. For practical application, MMF links therefore need to be tolerant to modal noise caused by mode selective losses.

Low coherence sources such as LEDs can be used to avoid modal noise in MMF optical links, but their bandwidths are limited to < 1 GHz and the coupling efficiency to silica MMF can be very low. In most cases, multimode vertical cavity surface emitting lasers (VCSELs) are used to prevent the occurrence of modal noise in MMF links. The logical choice for VCSELs is due to their low threshold currents, high bandwidths (up to 10 GHz), efficient coupling to fibers, and the low production costs.

Bit-loading and Relative Intensity Noise

Commercially available VCSELs for short-range optical links usually have a large active-area diameter allowing for multiple transverse modes. When supplying a current slightly above threshold, the fundamental mode will start lasing in most cases. Then more and more transverse modes will be excited with increasing current. Although the use of a low-coherence multimode source reduces the effect of modal noise, the existence of multiple modes in VCSELs gives rise to relative intensity noise (RIN), resulting from the interaction/competition of the different modes in the VCSEL [85, 86, 87].

Moreover, the frequency spectrum of RIN is not flat but varies for different frequencies at different bias currents [85, 87], which can result in a BER penalty when fixed modulation formats are used. By employing DMT with bit-loading, which adapts transmission rates to the frequency response of the channel, a first
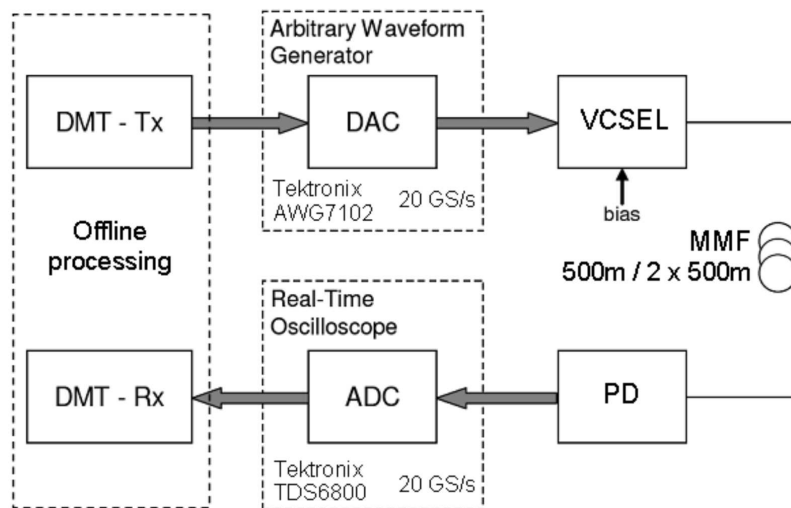
Figure 6.40: Measurement setup for DMT over MMF transmission. Tx: transmitter, Rx: receiver, DAC: digital-to-analog converter, ADC: analog-to-digital converter, PD: photodetector.

attempt is made to adapt to the effects of RIN in order to maximize transmission rate [75].

Although RIN can be a time-varying process, this experiment only shows the results for a particular spectral distribution of RIN as a proof of concept. Because offline processing is used in the experiment for modulation and demodulation of DMT waveforms as well as computation of bit-loading, a real-time adaptive system cannot be implemented. For the VCSEL used, it was observed that RIN varied very slowly in time (interval of minutes), with only abrupt changes when the bias current is changed (abruptly). Therefore, the experiment serves as a good starting point for further investigation of using DMT with bit-loading to adapt to RIN in VCSELs. This makes DMT an interesting solution to consider for short-range optical communication links, which usually need to be robust and adaptive to changes in the environment.

Experimental setup

Fig. 6.40 shows the setup of the DMT transmission system. The optical transmitter used is a commercial, analog-driven, 850-nm multimode VCSEL, specified for up to 10-Gbit/s operation with on-off keying modulation. Two 500 m spools of MMF
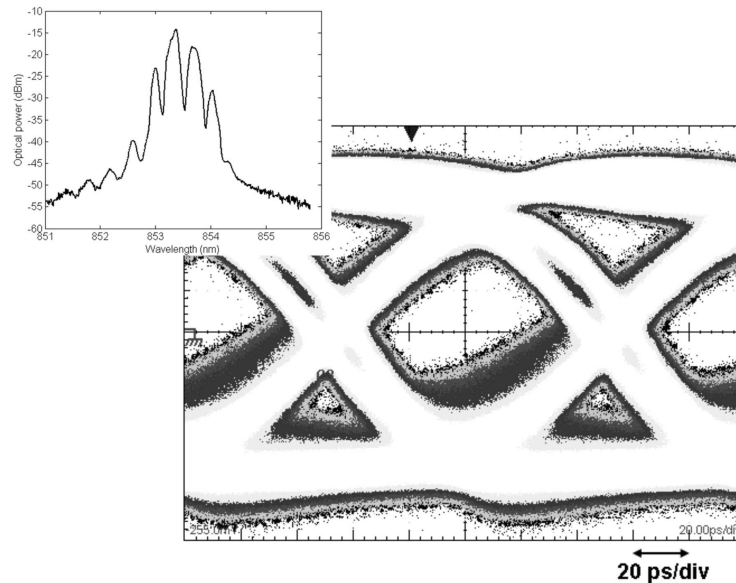
Figure 6.41: Measured 10-Gbit/s eye diagram after transmission over 1000 m of MMF using 850-nm VCSEL. Inset: Measured optical spectrum of VCSEL from 851 nm to 856 nm.

(Draka MaxCap550, OM4, 4700 MHz·km effective bandwidth at 850 nm) were used for the experiment. The two spools are connected together in the case of transmission over a distance of 1000 m. The photodetector (PD) with integrated trans-impedance amplifier consists of a 25-μm GaAs PIN diode, pigtailed to a 62.5 μm MMF via a graded-index (GRIN) lens. The optical output power of the VCSEL is fixed at -0.7 dBm and the detected power levels after 500 m and 1000 m of MMF are -1.9 dBm and -3.1 dBm respectively. Fig. 6.41 depicts the measured 10-Gbit/s eye diagram using the setup with 1000 m of MMF. The optical spectrum (from 851 to 856 nm) of the VCSEL is shown in the inset, where the different transverse modes of the VCSEL can be clearly distinguished.

Similar to all previous experiments, a computer is used to emulate the digital DMT modulator and demodulator by pre-computing the waveform to be transmitted and post-processing the received waveform. An AWG is used to generate the corresponding analog DMT waveform at a sampling speed of 20 GS/s and a real-time storage oscilloscope used to capture the received analog DMT signal after the PD at 20 GS/s. The received data are demodulated and evaluated offline with a computer.

A total of 256 subcarriers are available for DMT transmission, ranging from 0 to 10 GHz. Prior to bit-loading, a pilot DMT signal (all subcarriers with 16-QAM constellation, first at DC not modulated) is sent over the system to determine the available signal-to-noise ratio per subcarrier, as shown in Fig. 6.42a. It is apparent that the system bandwidth limits the transmission bandwidth to approximately 6 GHz.

Results

Fig. 6.42c and d show the results from Chow's bit-loading algorithm [48], for transmission over respectively 500 m and 1000 m of MMF. The desired bit-error-ratio (BER) is set to $1 \cdot 10^{-3}$, which corresponds to an SNR gap of approximately 7.2 dB. The bit-loading results show that only 150 out of a total of 256 subcarriers should be used to achieve maximum bit-rate, where some subcarriers are allocated up to 7 bits of information (128-QAM modulation). Due to the power allocation, the measured SNR per subcarrier after bit-loading are stair-case-shaped as depicted in Fig. 6.42b.

Fig. 6.43 shows the transmitted and received electrical DMT signal spectra for transmission over 1000 m of MMF. The curve in Fig. 6.43c is obtained when the VCSEL is turned on with a fixed bias, without any modulation. This shows the relative intensity noise (RIN) spectrum of the transmission system, resulting from the competition of different modes of the VCSEL [85, 86, 87]. This RIN also affects the channel SNR, which can be noticed as a dip at approximately 3.5 GHz in the evaluated SNR curves in Fig. 6.42a. Nevertheless, DMT with bit-loading adapts well to this loss of SNR. Fig. 6.44a and b show the BER per subcarrier after evaluation of 23000 received DMT symbols, equaling a total of 16 million bits. The total average BER for 500 m and 1000 m transmission are $7 \cdot 10^{-4}$ and $1 \cdot 10^{-3}$ respectively. From the bit-loading parameters, it can be calculated that 30 Gbit/s is achieved over 500 m and 28 Gbit/s over 1000 m of MMF using DMT with bit-loading. After deduction of 1.5 % of cyclic prefix, 2 % of pilot symbols, and 7 % of FEC overhead, the net transmission bit rate equals 27.2 Gb/s over 500 m and 25.4 Gb/s over 1000 m of MMF. Fig. 6.44c and d depict the highest received constellation diagrams employing 128-QAM after transmission over MMF, as an indication of the received signal quality.
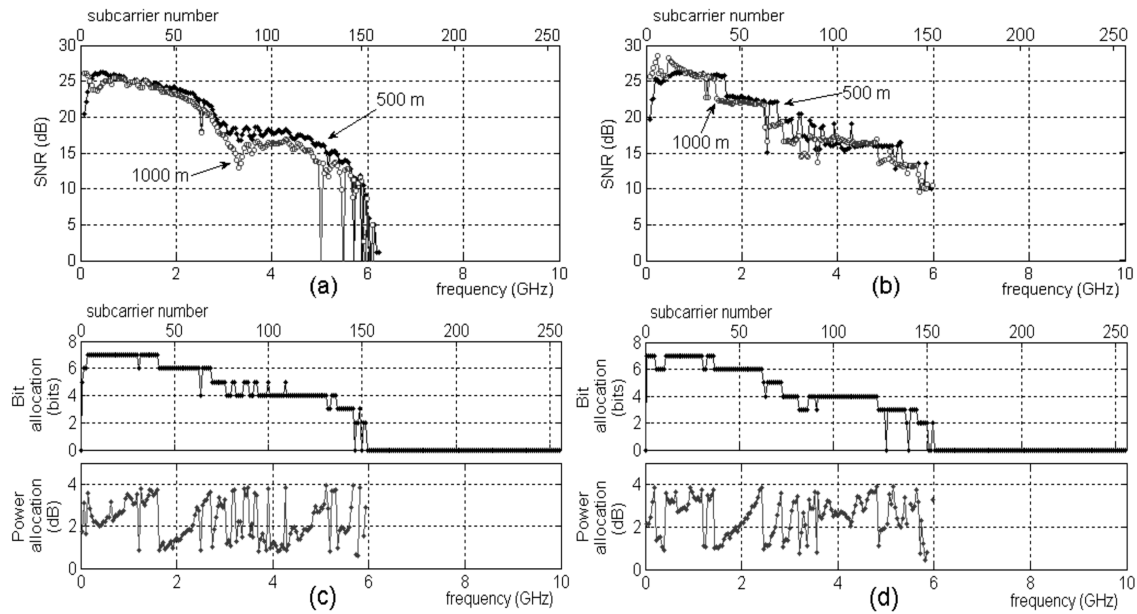
Figure 6.42: (a) Evaluated SNR per subcarrier (all with 16-QAM, first subcarrier at DC not modulated) after transmission over 500 m and 1000 m of MMF, prior to bit-loading. (b) Resulting SNR per subcarrier, after bit-loading. (c) Bit-loading parameters for 500 m MMF. (d) Bit-loading parameters for 1000 m MMF.
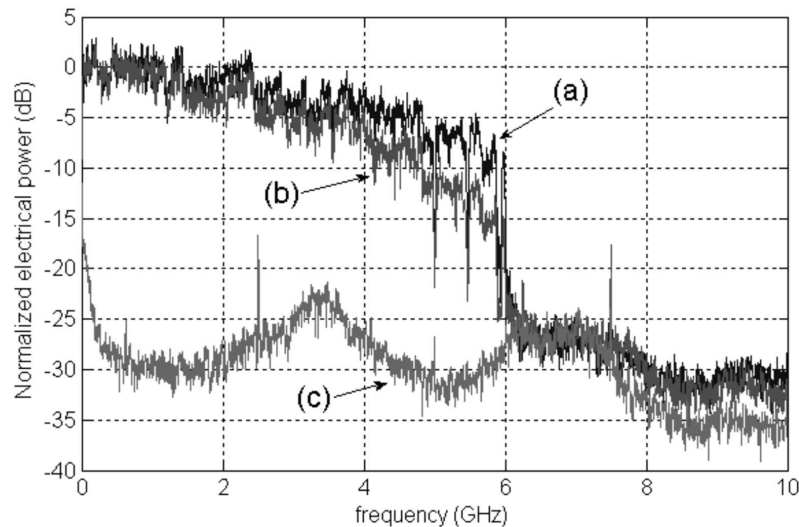
Figure 6.43: Measured electrical spectra for (a) sent DMT signal, electrical back-to-back; (b) received DMT signal, after 1000 m MMF; (c) relative intensity noise of VCSEL.
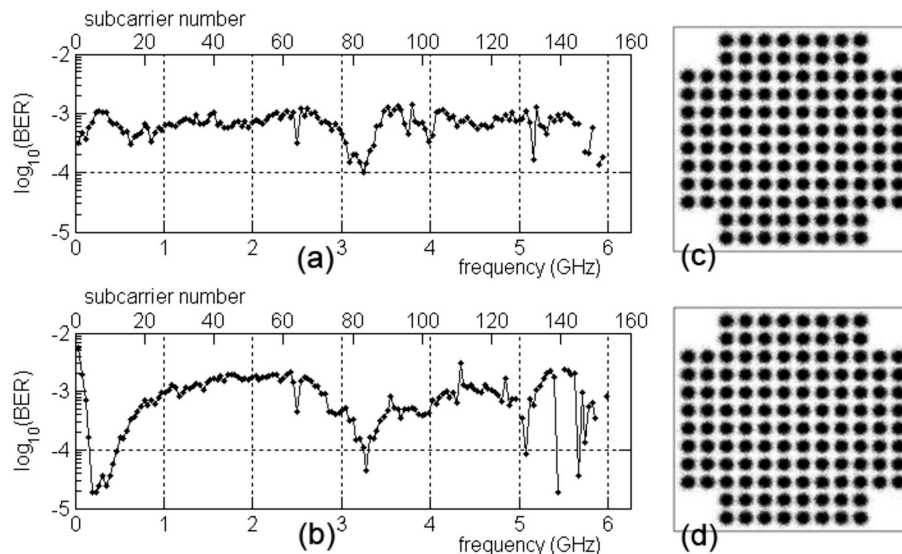
Figure 6.44: Measured BER per subcarrier for: (a) 500 m MMF, total averaged BER = $7 \cdot 10^{-4}$, (b) 1000 m MMF, total averaged BER = $1 \cdot 10^{-3}$. (c) Received 128-QAM constellations after 500 m MMF (d) 1000 m MMF.

6.3.3   Summary

In the first DMT experiment for silica MMF, a net transmission bit-rate of 21.6 Gbit/s was demonstrated over 730 m of silica MMF with direct modulation of an 850 nm VCSEL and direct detection with an MMF-coupled receiver. This bit-rate was achieved within a bandwidth of 5 GHz, resulting in a spectral efficiency of 4.3 bit/s/Hz. Standard on-off-keying modulation is not able to achieve such high bit-rates, due to both modal dispersion in the fiber as well as limited bandwidth of transceivers. The results show that DMT is an effective way for compensating modal dispersion in MMF and can enhance bit-rates while still using conventional low-cost transceivers due to the high spectral efficiency. It is therefore a promising solution for low-cost next-generation MMF LAN links operating beyond 10 Gbit/s.

Furthermore, a proof-of-concept experiment was demonstrated to use Chow's rate-adaptive bit-loading algorithm to adapt to the frequency-dependent RIN of the multimode VCSEL used, thereby maximizing the bit-rates (net) to 27.2-Gbit/s over 500 m and 25.4-Gbit/s over 1000 m of silica MMF. Therefore, also in the case of silica MMF, DMT with bit-loading seems to be an attractive solution to consider.

6.4 Optical Wireless

White-light LEDs are expected to become a major player in the future lighting market. So far, the opportunity of modulating their light emission for communication purposes remains untapped. Available modulation bandwidths lie in the MHz range [21, 22] and white-light LEDs might thus serve for illumination and data transmission simultaneously, as illustrated in Fig. 6.45. Advantages would be the inherent low investment and maintenance cost due to the dual-use scenario of illumination and communication, virtually zero interference with radio frequency wireless communication, the potential to spatially recycle the modulation bandwidth in pico- and femto-cells (due to the pronounced directivity of light and the highly efficient shielding by opaque surfaces), and secured information transfer by confining the light to a certain spot.

In this section, experiments present such investigations for phosphorescent white-light LEDs. This type of LEDs are chosen in contrast to the triple-chip RGB type due the market dominance of the former. As observed in [21], the disadvantageously small modulation bandwidth of phosphorescent white-light LEDs can be increased from 3 to 20 MHz when only the blue part of the emitted optical spectrum is detected. This is because a phosphorescent white-light LED consists of a fast blue LED, which excites the phosphorous layer of the LED to emit white light. This
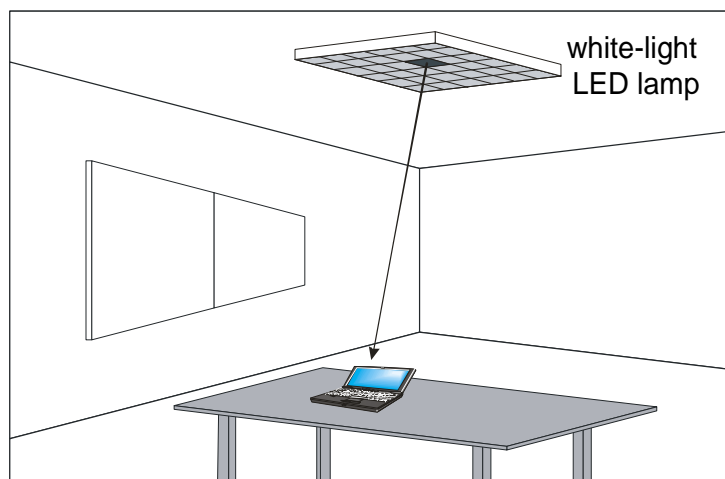
Figure 6.45: Data transmission and illumination scenario.
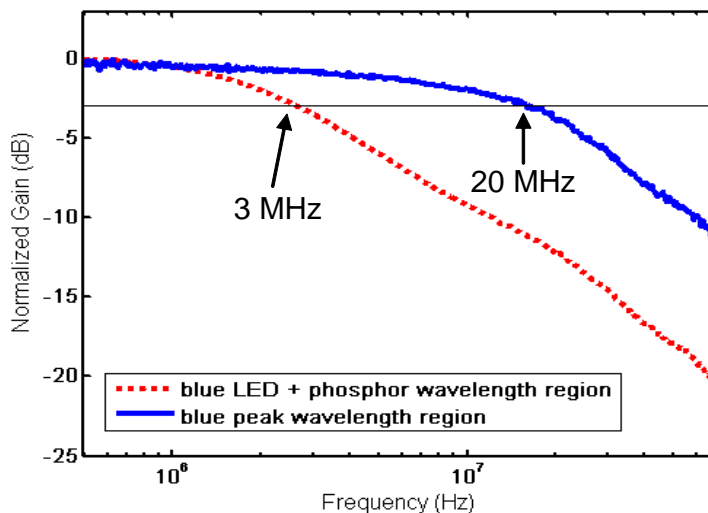
Figure 6.46: Frequency response of phosphorescent white-light LED with and without blue filtering.

phosphorous emission is a relatively slow process, when compared to the blue light emission. This potential of blue filtering is verified as depicted in Fig. 6.46. From the figure, the positive impact of blue filtering on the -3 dB bandwidth of the phosphorescent white-light LED can be observed.

6.4.1 Transmission Performance of a Single LED

Firstly, the transmission performance of a single LED is investigated [22]. The experimental setup is shown in Fig. 6.47. A single white-light LED with a luminous intensity of 18 cd and a 15° full opening angle at 50 % maximum intensity was used. The distance between LED and detector was chosen to be 1 cm, so that the illuminance in front of the blue transmission filter (passband 300–500 nm) was approximately 700 lux (corresponding to an irradiance of 3 W/m^2). This lies well within the range of 200–800 lux for office areas, as stipulated by standard [92]. In a lighting scenario, this distance would naturally be much larger (some meters) due to the higher total luminous intensity rendered through a multitude of chips (as in Fig. 6.45).

A DC-bias is added to the AC-coupled DMT modulation signal generated by an AWG. In order to provide sufficient modulation power, the output of the AWG

Figure 6.47: Experimental setup for visible light communication. DAC: Digital-to-analog converter, PD: Si-photodiode with trans-impedance amplifier, ADC: analog-to-digital converter.

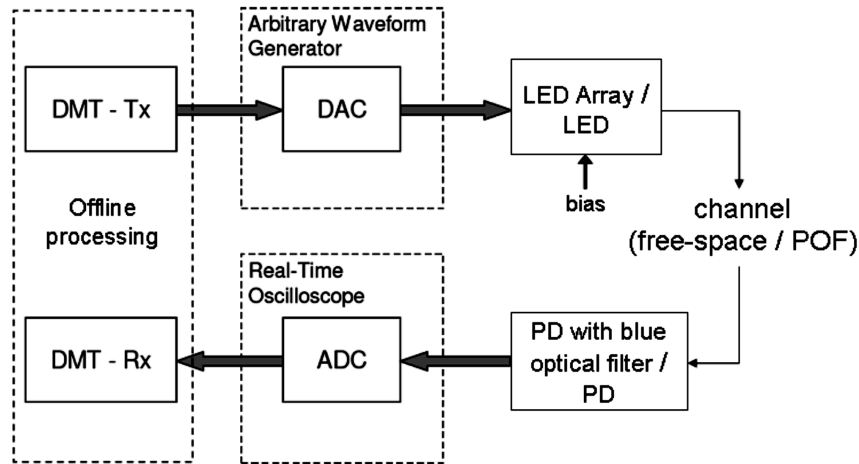was additionally amplified and low-pass filtered before being combined with the DC-bias. As detector served a PIN diode with an integrated trans-impedance amplifier, and the output from this detector was additionally amplified and low-pass filtered (30 MHz) before being captured with a real-time digital storage oscilloscope (DSO) at a sampling speed of 100 MS/s).

For reference, on-off-keying modulation consisting of $2^9 - 1$ pseudo-random bit sequence (PRBS-9) produced by a pattern generator was used to modulate the single phosphorescent LED at a bit-rate of 40 Mbit/s, and the transmitted light was detected without and with the blue optical filter. Such fairly short PRBS sequences are appropriate for line-coded transmission, like e.g. Fast Ethernet. The modulation depth of the optical signal was 25 % and was limited by the maximum output power of the pattern generator. Without the filter (Fig. 6.48a), and therefore detecting the entire optical spectrum, the signals were completely distorted due to the low modulation bandwidth of the emitted light ($\approx$ 3 MHz). In contrast, when only the blue optical spectrum is detected using the blue filter, clearly visible eye openings (Fig. 6.48b) can be observed. The prevalent high SNR ($>$ 20 dB) ensures a clear visibility of the partially closed eye. This opening could of course be further improved by increasing the modulation depth.

For DMT transmission, software-generated random sequences were used for 32-
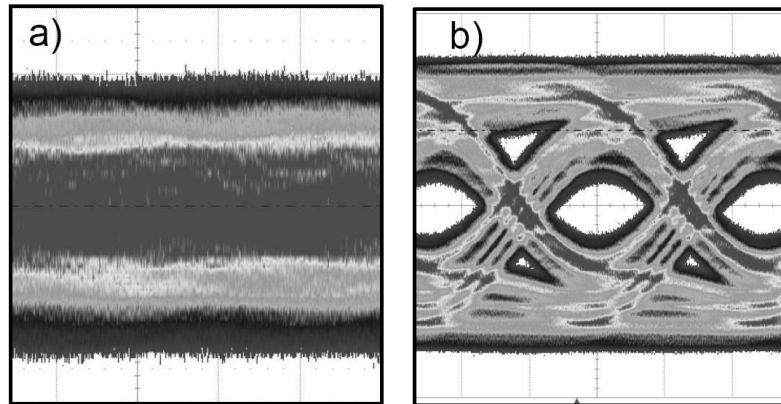
Figure 6.48: Persistence plot of eye diagrams for the received PRBS-9 sequences at 40 Mbit/s (abscissa: 10 ns/div); (a) without and (b) with blue filter.

QAM modulation on a 32-subcarrier DMT signal. The time-domain waveforms were then loaded into and output by the AWG. DMT is chosen as modulation format since it offers high spectral efficiency and since the signal spectrum can be adapted to minimize potential interference from e.g. fluorescent light bulbs. Of the total 32 available subcarriers, the first (at DC) and the last (poor SNR) one were not modulated. The carrier spacing was 0.78 MHz, the used transmission bandwidth 24 MHz, and the aggregate data-rate 117 Mbit/s. The rather strong attenuation of carriers at higher frequencies was compensated by pre-equalization, as can be seen in Fig. 6.49a. Fig. 6.49b depicts the superimposed received constellation diagram of all subcarriers. The individual constellation points can clearly be distinguished, which is reflected in the overall low BER values per subcarrier, as displayed in Fig. 6.49c. For this, 200000 DMT frames were transmitted and received, equaling to 30 million bits in total. The total averaged BER of the DMT transmission system is calculated to be $8 \cdot 10^{-5}$. Using a standard Reed-Solomon (255,239) FEC code will result in a total system BER below 10^{-14}. From the aggregate data-rate, one needs to subtract the following overheads: 7 % for FEC, 6.3 % for the cyclic prefix and 2 % for pilot symbols, which results in a net data-rate of 101 Mbit/s for a single phosphorescent white-light LED.
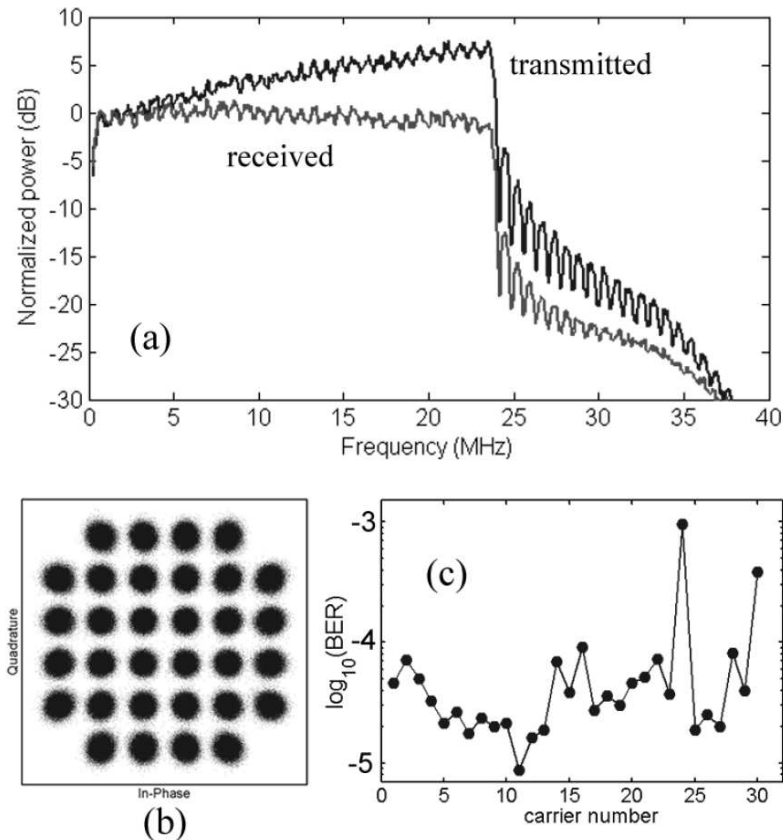
Figure 6.49: Experimental results for 32-QAM DMT modulation. (a) Electrical spectrum of the signal supplied to the LED and of the received signal. (b) Constellation diagram of all sub-carriers superimposed on each other. (c) Bit-error ratio (BER) for the individual sub-carriers (circles).

6.4.2 Transmission Performance of an LED-Array

In order to investigate the DMT performance of a white-light LED lamp in a more realistic scenario, a further experiment is carried out using an LED-array consisting of 40 white-light phosphorescent LEDs [93]. The same experimental setup depicted in Fig. 6.47 is used. Similar to the single-LED case, the AWG is used to generate a pre-computed, random DMT sequence consisting of 32 subcarriers. After addition of a DC-bias, this electrical signal is used to directly modulate the LED-array. A photodetector (1-mm active diameter, with blue optical filter), equipped with a coupling lens, is placed at a distance of 0.75 m from the transmitting LED-array. The illuminance at the photodetector, measured before the coupling lens and optical
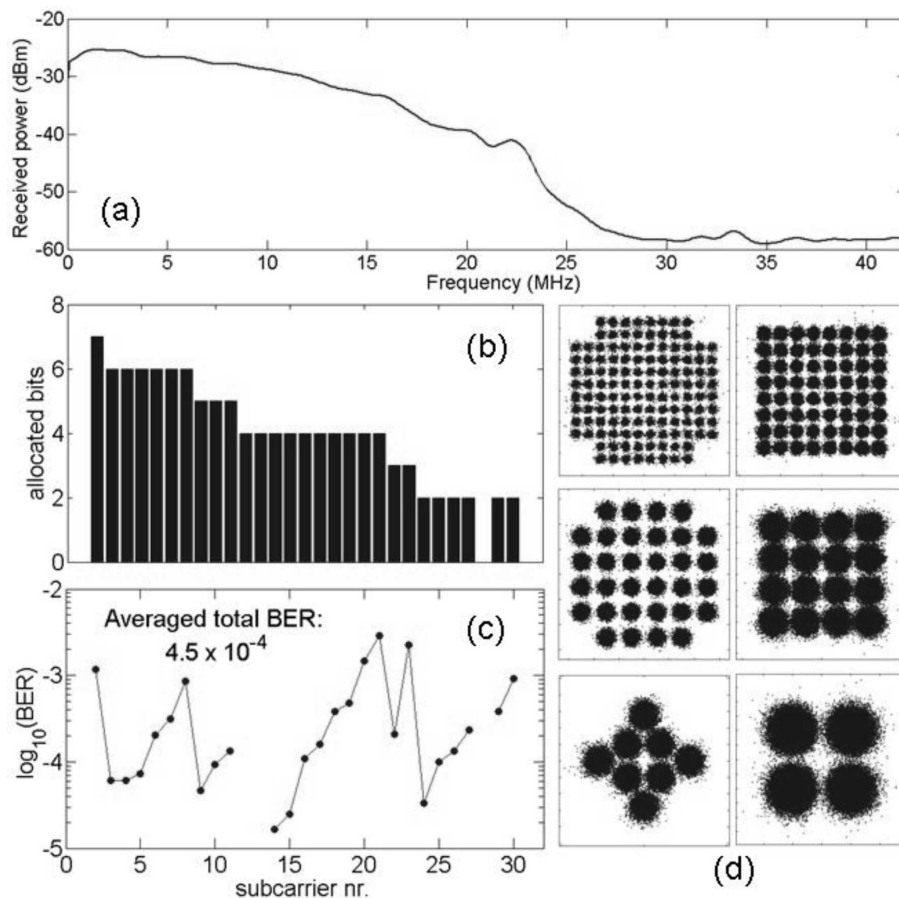
Figure 6.50: Measurement results for white-light LED lamp (40 LEDs) at a distance of 0.75 m. (a) Received electrical DMT signal spectrum. (b) Allocated number of bits per subcarrier. (c) Evaluated BER per subcarrier, no errors detected for subcarriers without dots. (d) Received constellations of all subcarriers.

filter, is approximately 200 lux. This value lies at the bottom range of 200–800 lux for office areas [92]. The received electrical DMT signal from the photodetector is then captured with a DSO and demodulated using offline processing. The sampling rates of the AWG and DSO are both set at 100 MS/s (four-fold oversampling), equaling to a transmission rate of 90 Mbit/s. After deduction of 6.25 % of cyclic prefix, 5 % of pilot symbols, and 7 % of FEC, the net transmission rate equals 74 Mbit/s.

The measurement results are depicted in Fig. 6.50. In Fig. 6.50a, the received DMT signal spectrum is shown. It can be seen that the signal bandwidth is 25 MHz. The −3 dB bandwidth of the entire transmission system is 12 MHz. Fig. 6.50b de-

picts the allocated number of bits per subcarrier, as a result of bit-loading. This adapts the constellation size of each subcarrier to the signal-to-noise ratio at the corresponding subcarrier frequency, thereby maximizing system throughput. Fig. 6.50c shows the BER results per subcarrier. Because serial data is transmitted in parallel using subcarriers with DMT, the total BER of the received data should be averaged from all subcarriers used and is calculated to be $4.5 \cdot 10^{-4}$. By employing FEC coding, BER values below 10^{-12} can be achieved. Finally, the received constellation diagrams are shown in Fig. 6.50d. In this case, constellations ranging from 4 to 128-QAM are used.

6.4.3 Summary

As white-light LEDs are expected to become a major player in the future lighting market, the combination of illumination and optical wireless information communication with such systems can be envisaged. The experiments presented here demonstrate the feasibility of high-speed optical wireless data transmission. This is achieved by directly modulating and detecting the output from both a single phosphorescent white-light LED as well as an LED-array in a lighting-like scenario. Due to an increase in modulation bandwidth when detecting only the blue part of the emitted optical spectrum and a prevailing high optical SNR, data-rates up to 100 Mbit/s for a single LED and 74 Mbit/s for an LED-array was shown by employing spectral-efficient and adaptive multi-level modulation on DMT subcarriers. Lower data-rates were achieved for the LED-array due to the higher current that was needed to drive the array, consisting of 40 individual LEDs. This, in turn, results in lower rise and fall times and therefore less modulation bandwidth. In conclusion, the combination of DMT and optical wireless is an interesting approach for future wireless in-home information networks, making use of illumination for information transfer.

CHAPTER 7

REAL-TIME IMPLEMENTATION OF DMT

In the previous sections, it has been shown that potentially high bit rates can be achieved over the optical IM/DD channel using DMT. However, all presented experimental results were performed using offline processing, which involves the process of using software to modulate and demodulate stored sequences that were transmitted and received over a real physical channel. Although this is useful for evaluating the performance of a specific modulation and demodulation technique including digital signal processing, there is no constraint on the practicability of such algorithms.

In order to understand more clearly and identify where the major differences between offline and real-time signal processing are, an approach is made to implement a real-time DMT system and investigate its performance. This chapter first presents a method for efficient implementation of a real-valued DMT modulator and demodulator by dual-use of a complex-valued FFT-core. Following this, details and measurement results regarding the implementation of a real-time 1.25-Gbit/s DMT modulator are presented and discussed.

7.1 Efficient Hardware Implementation of DMT

In this section, an efficient method for the implementation of a DMT modulator and demodulator (modem) is presented, by dual-use of a complex FFT-core. This is based on the method proposed in [28] to compute two real-valued FFTs using a complex-valued FFT. Usually, when implementing a DMT modem in hardware, a standard FFT-core is used which performs a complex-valued IFFT/FFT operation. From (3.1) and (3.3), it can be seen that for an N-carrier DMT system, a $2N$-point IFFT/FFT operation is needed to implement the modem. This will result in a real-valued baseband output, which is typical for DMT.

When compared to OFDM, where an N-point IFFT/FFT is needed for an N-carrier based system, one might conclude that DMT requires two times the resources of OFDM, and is therefore not as efficient to implement. This, however, is not true. By dual use of the real and imaginary parts of a complex IFFT/FFT operation, it is possible to use one single $2N$-point IFFT/FFT operation to simultaneously compute two different DMT frames. This is because of the real-valued DMT output signal based on the property of Hermitian symmetry given by (3.1).

In (3.3), it was shown that the output of a $2N$-point IFFT is real-valued when the symmetry property given in (3.1) is satisfied. However, it is also possible for the IFFT to produce a purely imaginary-valued output without any real values. This can be considered as an additional orthogonal output. By defining a second input with complex values D_n $(n = 0, 1, \ldots, N-1)$ for the $2N$-point IFFT, modifying the symmetry property given in (3.1) will yield the following property

$$D_{2N-n} = -D_n^*　\tag{7.1}$$

where $n = 1, 2, \ldots, N-1$ and $\text{Im}\{D_0\} = \text{Im}\{D_N\} = 0$. This will result in a purely imaginary-valued output from the $2N$-point IFFT. If we combine the two different inputs C_n and D_n $(n = 0, 1, \ldots, N-1)$ and pass them orthogonally as a new complex value $X_n = C_n + jD_n$ into the IFFT following properties (3.1) and (7.1), the resulting

output will be

$$s_k = \frac{1}{\sqrt{2N}} \sum_{n=0}^{2N-1} X_n \exp\left(j2\pi k \frac{n}{2N}\right) \tag{7.2a}$$

$$= \frac{1}{\sqrt{2N}} \sum_{n=0}^{2N-1} (C_n + jD_n) \cdot \exp\left(j2\pi k \frac{n}{2N}\right) \tag{7.2b}$$

$$= \frac{1}{\sqrt{2N}} \left[\sum_{n=0}^{2N-1} C_n \exp\left(j2\pi k \frac{n}{2N}\right) + j \sum_{n=0}^{2N-1} D_n \exp\left(j2\pi k \frac{n}{2N}\right) \right] \tag{7.2c}$$

$$= s_k^{C_n} + js_k^{D_n} \tag{7.2d}$$

where $s_k^{C_n}$ and $s_k^{D_n}$ are both real-valued DMT time frames resulting from C_n and D_n respectively and $k = 0, 1, \ldots, 2N - 1$. As a result, a two-input, two-output DMT modulator is created with a single $2N$-point IFFT, using both the real and imaginary in- and outputs.

With this method, a single $2N$-point IFFT/FFT can be used to compute two DMT frames simultaneously, resulting in the same amount of resources required when compared to OFDM.

7.2   Real-Time Gigabit DMT Transmission

This section focuses on the use of DMT in SI-POF systems based on 650-nm resonant-cavity LEDs. In order to investigate the feasibility of real-time Gbit/s transmission with DMT, a 1.25-Gbit/s DMT transmitter is implemented in a Field Programmable Gate Array (FPGA) and the results are reported in this section. For application in automotive networks, a commercial resonant-cavity LED (RC-LED) and a standard PIN photodiode with a large active-area diameter of 540 μm are used for optical transmission and reception respectively.

7.2.1   System Implementation

Fig. 7.1 shows a functional block diagram of the implementation of the DMT transmitter in an FPGA (Xilinx Virtex-4 FX100, with clock speed up to 450 MHz). A $2^{24} - 1$ pseudo-random binary sequence (PRBS) is generated as input source to the
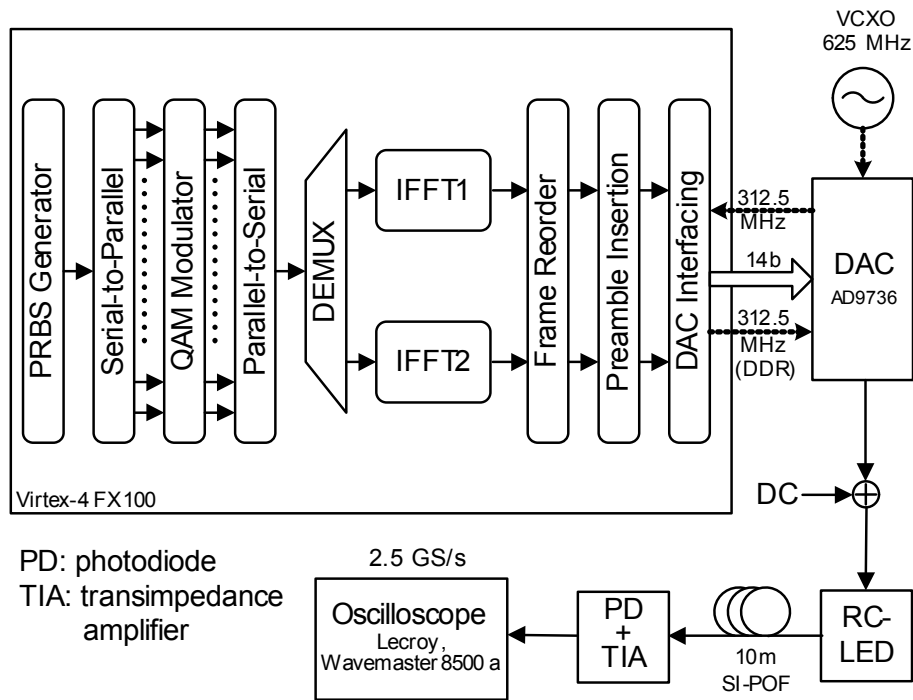
Figure 7.1: FPGA implementation of DMT transmitter and experimental setup for performance evaluation.

DMT modulator. This input sequence is serial-to-parallel converted and mapped onto different quadrature amplitude modulation (QAM) constellation points, implemented using read-only memory cells.

After this, the parallel QAM symbols are serialized because the pipelined IFFT-core needs serial input data. A demultiplexer (DEMUX) is needed to split the serial data into two parallel processing streams clocked at 312.5 MHz each because the FPGA cannot support a clock frequency as high as 625 MHz. As a result, two IFFT-cores (clocked at 312.5 MHz each) are needed to process the data which is sent to the D/A converter at double data rate after reordering of the DMT frames and insertion of training preambles. The DAC samples at a speed of 625 MSamples/s.

Fig. 7.2 depicts the relative amount of resources needed for each of the functional blocks when all functions are to be implemented using only FPGA slices. A Virtex-4 slice consists of two flip-flops and two 4-input look-up-tables. In the actual implementation, FPGA-specific hardware such as embedded multipliers and block RAMs are used so that full performance can be achieved. As expected, it can be
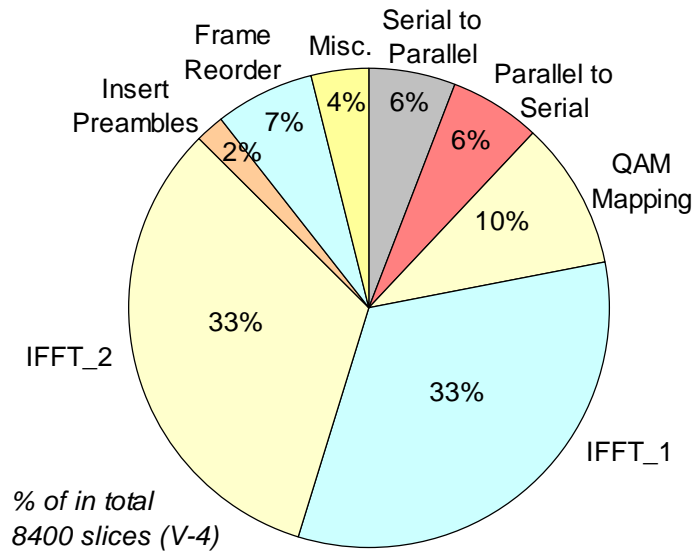
Figure 7.2: Virtex-4 FPGA slices utilized in DMT transmitter according to functionality (normalized).

seen from Fig. 7.2 that the IFFT core demands most resources. Depending on the bandwidth of the DMT signal and the sampling speed of the DAC, parallelization is needed because of the limited FPGA chip rate. For a bit-rate of 1.25 Gbit/s, implementation in an application-specific integrated circuit (ASIC) will allow higher chip rates and may discard the need for parallelization. However, for higher-bit-rate OFDM/DMT systems at speeds of for example 10 Gbit/s, parallelization will nevertheless be needed because the speed of ASICs will not be sufficient. Therefore, for such applications, more resources for IFFT processing will be required due to the need for (several orders of) parallelization. This is an important issue which should be considered when implementation complexity of digital signal processing techniques in high-speed fiber-optic transmission systems is studied.

7.2.2 Experimental Results

The experimental setup for evaluating the performance of the DMT modulator is shown in Fig. 7.1. The DMT sequence generated by the DAC (at 625 MSamples/s) is used to drive an RC-LED for transmission over 10 m of SI-POF. Such distances are typical for automotive networks and the main limitation originates from the low bandwidth of the LED-based transmitter. The received optical power after
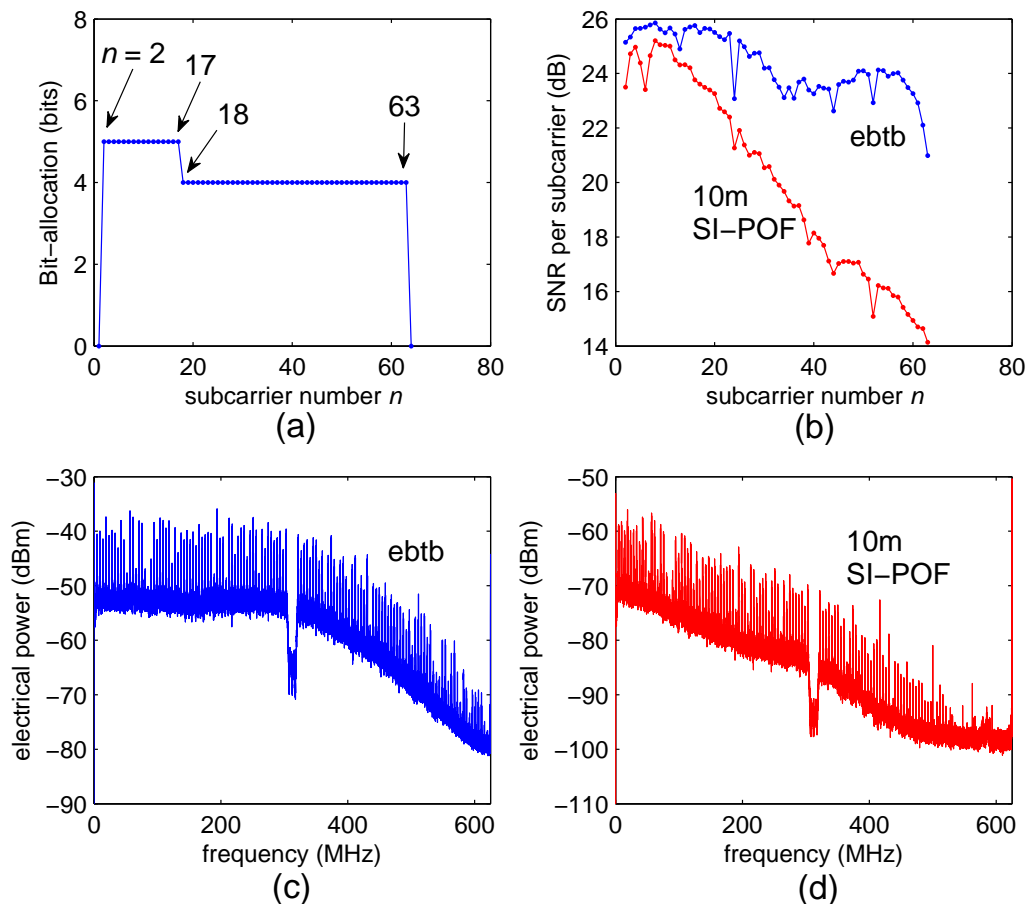
Figure 7.3: (a) Bit-allocation per subcarrier. (b) Measured SNR per subcarrier for electrical back-to-back and after transmission over 10 m SI-POF. (c) Spectrum of DMT signal measured for electrical back-to-back and (d) after 10 m SI-POF.

10 m SI-POF is -3 dBm and the modulation index is approximately 0.6. An Si-photodiode with a large-diameter (540 μm) active area followed by an integrated trans-impedance amplifier is used to receive the optical signal and a digital storage oscilloscope sampling at 2.5 GSamples/s is used for demodulation and evaluation of the received DMT sequence. Fig. 7.3 shows the results of the real-time DMT transmitter. A 128-point IFFT is used for the DMT modulator where the first and last subcarriers are set to 0. Therefore, a total of 62 subcarriers is available and used for information transmission.

Furthermore, a 4-point cyclic prefix is used to guard against inter-frame interference due to channel dispersion and 10 preambles per 100 DMT frames are

transmitted for training and channel estimation purposes. All preambles are exact copies of a single preamble, which is generated by DMT modulation of a particular data sequence in order to minimize its crest factor.

A simple fixed bit-loading scheme is applied by allocating the number of bits per subcarrier as depicted in Fig. 7.3a. By summing up the allocated bits of all subcarriers, a total of 264 allocated bits per DMT frame is found. With a DAC sampling rate of 625 MSamples/s and a 128-point DMT frame plus 4 points of cyclic prefix, the DMT frame rate (also known as symbol rate) is calculated to be $(128 + 4)/625 \cdot 10^6 \approx 0.2$ μs. This results in an aggregate bit-rate of 1.25 Gbit/s, which reduces to 1.125 Gbit/s after deduction of preamble overhead.

The signal-to-noise ratio (SNR) per subcarrier of the DMT transmitter is measured and plotted in Fig. 7.3b for both electrical back-to-back and transmission over 10 m SI-POF. The bandwidth limitation of the SI-POF channel can clearly be seen. Fig. 7.3c depicts the measured electrical back-to-back spectrum of the DMT signal, where the desired signal spectrum (from 0 to 312.5 MHz) including its mirrored replica (beyond 312.5 MHz) due to conversion from digital (discrete) to analog (continuous) domain can be seen. Unlike wireless communications, this mirrored spectrum does not need to be removed by filtering before transmission over SI-POF because it does not interfere with other communication bands.

In Fig. 7.3d, the influence of the low-pass SI-POF channel bandwidth on the measured received electrical DMT spectrum can be observed. Notice also the frequency spikes occurring in the spectra of both Fig. 7.3c and d, which is a result of the preambles (10 out of every 100 DMT frames). These preambles have been assigned twice the power of a standard DMT data frame, which is allowed due to their minimized crest factor. In Fig. 7.4a-d, the received constellation diagrams (after 10 m SI-POF) are plotted for the subcarriers indicated by the arrows in Fig. 7.3a.

7.2.3 Summary

An analysis of hardware resources needed for implementing Gigabit DMT transmission shows that parallelization of signal processing functions plays an important role in defining hardware complexity when operating at high bit-rates. Experimental results show successful implementation of a real-time 1.25-Gbit/s DMT transmitter
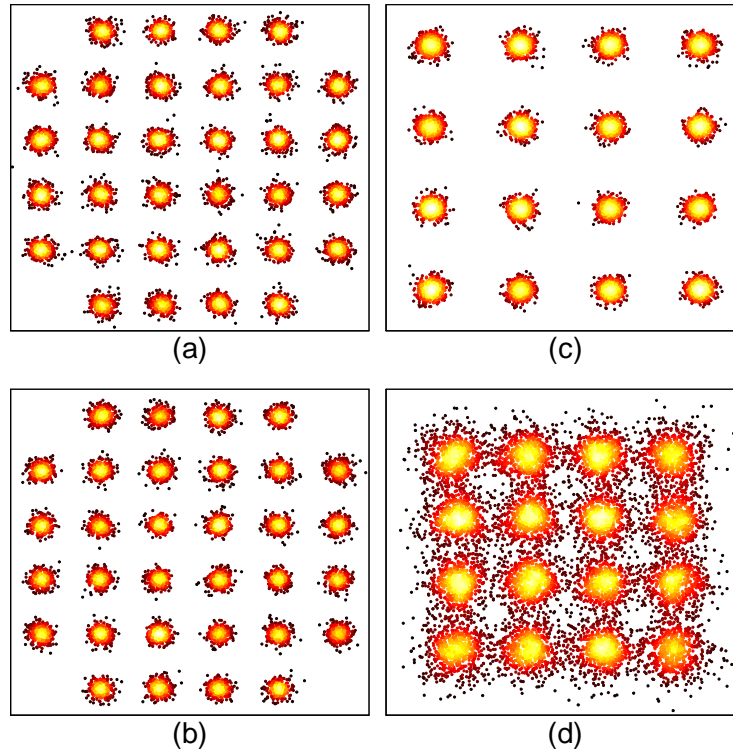
Figure 7.4: Received constellation diagrams after 10 m SI-POF for subcarriers indicated by the arrows shown in Fig. 7.3a; (a) subcarrier number $n = 2$ (b) $n = 17$ (c) $n = 18$ (d) $n = 63$.

using an RC-LED over 10 m of SI-POF. The results prove that DMT is a promising candidate for upgrading conventional LED-based SI-POF links to enable Gigabit transmission.

Chapter 8

Pulse Amplitude Modulated DMT

In low-cost optical communication systems such as multimode fiber and optical wireless, IM/DD is employed where only the intensity of light is modulated. Application of DMT over such an optical IM/DD channel is different from standard electrical systems, because the bipolar baseband signal is used to modulate the intensity of the optical source, which can only have positive values. In IM/DD DMT systems, this problem is commonly solved by adding a DC bias to the bipolar DMT signal to make it unipolar, referred to as DC-biased DMT, which has been the topic of this thesis in all previous chapters. However, it has also been shown by [94, 30] that it is possible to clip the negative parts of a DMT signal to zero and to transmit only the positive parts of the DMT waveform as in asymmetrically clipped optical OFDM (ACO-OFDM).

In [30], it was shown that ACO-OFDM can offer better performance than DC-biased DMT due to asymmetric clipping. The idea is to modulate only the odd-numbered subcarriers to transmit information whereas the even-numbered ones are used to accommodate distortion resulting from asymmetric clipping of the negative values of the ACO-OFDM waveform. Although this is not a problem for a channel with flat frequency response, the restriction to use only odd-numbered subcarriers can degrade performance in a frequency-selective channel. Especially when bit-

loading is employed, where the allocation of bits and power per subcarrier is adapted to the signal-to-noise ratio (SNR) of the frequency-selective channel [24, 9], the restriction to modulate only odd-numbered subcarriers will result in a non-optimal adaption to the channel response, causing a loss in system performance.

This section presents a novel concept of pulse-amplitude-modulated DMT (PAM-DMT), which also allows asymmetric clipping at zero value and transmission of only the positive parts of the DMT signal as in ACO-OFDM [95]. In contrary to ACO-OFDM, all subcarriers can be used to transmit information, so that bit-loading can be used to fully adapt the waveform to the system's channel response and achieve optimum performance.

8.1   Concept of PAM-DMT

For a standard DMT system, the multicarrier DMT discrete time-domain sequence $x(k)$ generated with a $2N$-point IFFT can be written as:

$$x(k) = \frac{1}{\sqrt{2N}} \sum_{n=0}^{2N-1} C_n \exp\left(j2\pi k \frac{n}{2N}\right), \tag{8.1}$$

for $k = 0, 1, \ldots, 2N - 1$. C_n $(n = 1, 2, \ldots, 2N - 1)$ are complex-valued information symbols. In order to achieve a real-valued output signal after the $2N$-point IFFT for baseband transmission, only $N - 1$ symbols, i.e. C_n for $n = 1, 2, \ldots, N - 1$, can be modulated with useful data, because the Hermitian symmetry $C_{2N-n} = C_n^*$ has to be satisfied. For DC-biased DMT over optical IM/DD channels, $C_0 = C_N = 0$ because it is more practical to add an analog DC-bias after digital-to-analog (DA) conversion of $x(k)$. The resulting time-continuous DMT waveform $x(t)$ after D/A conversion is given by:

$$x(t) = \sum_{k=0}^{2N-1} x(k)\delta(t - k) \otimes h(t),$$

where $\otimes$ is the convolution operator, $\delta(t)$ is the Dirac impulse, and $h(t)$ is the interpolation filter of the DAC. $h(t)$ is chosen here to be a rectangular pulse, representing the DAC sample-and-hold function.

In the case of PAM-DMT, the real parts of C_n are set to zero and only the imaginary parts are pulse-amplitude modulated, resulting in: $C_n = jB_n$, where B_n $(n = 1, 2, \ldots, N-1)$ are the PAM symbols containing useful data. Taking into account the Hermitian symmetry, where $B_{2N-n} = -B_n$, (8.1) can be rewritten as:

$$
\begin{aligned}
x(k) &= \frac{1}{\sqrt{2N}} \sum_{n=0}^{2N-1} C_n \left(\cos \left(2\pi k \frac{n}{2N} \right) + j \sin \left(2\pi k \frac{n}{2N} \right) \right) \\
&= \frac{-2}{\sqrt{2N}} \sum_{n=0}^{N-1} B_n \sin \left(2\pi k \frac{n}{2N} \right)
\end{aligned}
\tag{8.2}
$$

for $k = 0, 1, \ldots, 2N-1$, the values $C_n = jB_n$, and $B_0 = B_N = 0$, in the case of PAM-DMT. Fig. 8.1a depicts an example of the resulting time-discrete PAM-DMT waveform for $N = 32$. Notice that the positive and negative parts of the waveform are anti-symmetrical along the zero-valued axis because it consists of only $\sin(2\pi k \frac{n}{2N})$ terms as derived in (8.2). As a result, clipping away the negative values (see Fig. 8.1b) will not discard any useful information, as the same information is again contained in the positive parts of the waveform. Fig. 8.2a shows the corresponding demodulated 4-PAM constellation for a PAM-DMT waveform without asymmetrical clipping and Fig. 8.2b shows the same for a PAM-DMT waveform with asymmetrical clipping, where all negative waveform values are clipped to zero and only the positive parts of the waveform are transmitted and received. Observe that the distortion resulting from asymmetric clipping falls orthogonally onto the real-valued parts of the PAM signal, without influencing the imaginary parts modulated with information.

8.2 Performance Comparison by Simulations

In order to investigate the performance of PAM-DMT in comparison to DC-biased DMT and ACO-OFDM, simulations regarding the three modulation schemes have been performed.
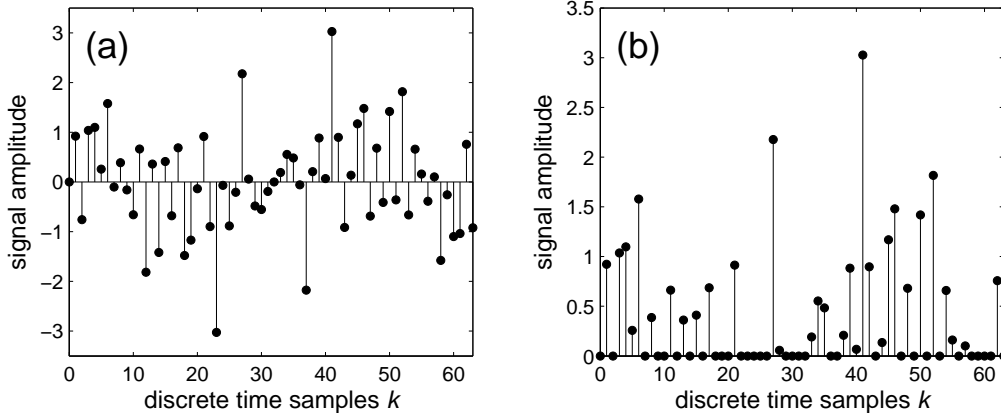
Figure 8.1: PAM-DMT discrete time-domain waveform (a) before and (b) after asymmetric clipping of negative values.
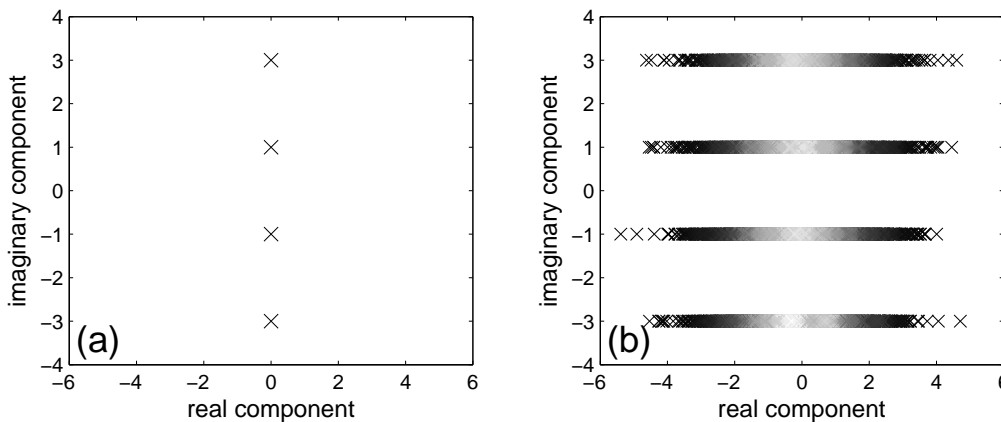
Figure 8.2: Demodulated 4-PAM-DMT constellation (a) without and (b) with asymmetric clipping of negative values.

8.2.1 Simulation Parameters

In DC-biased DMT, the value of the bias depends on the peak amplitude of the waveform. Due to incidental constructive in-phase addition of a large number of subcarriers, instantaneous peak amplitude values can get very large and should therefore be limited. The most straightforward way is to clip the signal. The resulting unipolar, DC-biased DMT signal $s_{DMT}(t)$ is given by:

$$s_{DMT}(t) = \underbrace{\mu\sqrt{\langle x^2(t)\rangle}}_{\text{DC-bias}} + \hat{x}(t), \qquad (8.3)$$

where μ is the clipping factor, $\sqrt{\langle x^2(t) \rangle}$ is the root-mean-square value of the DMT signal $x(t)$ before clipping, and $\hat{x}(t)$ is the clipped time-continuous DMT signal with peak amplitude values limited to $\mu\sqrt{\langle x^2(t) \rangle}$. When $s_{DMT}(t)$ is used to modulate the intensity of an optical source, the resulting mean optical power P_{opt} is proportional to the DC-bias given by $\mu\sqrt{\langle x^2(t) \rangle}$, as derived in [9] and [30].

In the case of ACO-OFDM and PAM-DMT, no DC-bias is needed because negative parts of the waveforms are clipped to a value of zero, resulting in a waveform $s(t)$ given by:

$$s(t) = \begin{cases} \mu\sqrt{\langle x^2(t) \rangle} & \text{for } x(t) > \mu\sqrt{\langle x^2(t) \rangle} \\ x(t) & \text{for } 0 \leq x(t) \leq \mu\sqrt{\langle x^2(t) \rangle} \\ 0 & \text{for } x(t) < 0 \end{cases} \tag{8.4}$$

where $s(t)$ can be represented as either $s_{ACO-OFDM}(t)$ or $s_{PAM-DMT}(t)$ and $x(t)$ is the corresponding ACO-OFDM or PAM-DMT waveform before asymmetric clipping with peak amplitude values limited to $\mu\sqrt{\langle x^2(t) \rangle}$. Unlike DC-biased DMT, the resulting mean optical power P_{opt} when $s_{ACO-OFDM}(t)$ or $s_{PAM-DMT}(t)$ is used to modulate the intensity of an optical source is proportional to $\sqrt{\langle x^2(t) \rangle}$, which is independent of the peak amplitude value and the clipping factor μ. This is the performance gain that is achieved when compared to DC-biased DMT.

8.2.2 Mean Power Limited System

Fig. 8.3 depicts simulation results where the system performances of the three modulation schemes are compared for an IM/DD optical channel. In the simulation model, $s_{DMT}(t)$, $s_{ACO-OFDM}(t)$, and $s_{PAM-DMT}(t)$ are alternately used to modulate the intensity of an optical source, transmitted over a channel with flat frequency response, and detected by a photodetector with additive white Gaussian noise. The number of subcarriers N is 256 and a noise equivalent power (NEP) of $16 \cdot 10^{-12}$ W/Hz is assumed, which was shown in [9] to be realistic for a photodetector with an integrated transimpedance amplifier. For different values of μ and modulation level M, the required mean received optical power (receiver sensitivity) for a system BER of 10^{-3} is plotted. Because ACO-OFDM uses only half of the total number of subcarriers N for transmitting useful information, the M-QAM and M-PAM modulation levels of respectively DC-biased DMT and PAM-DMT should be compared
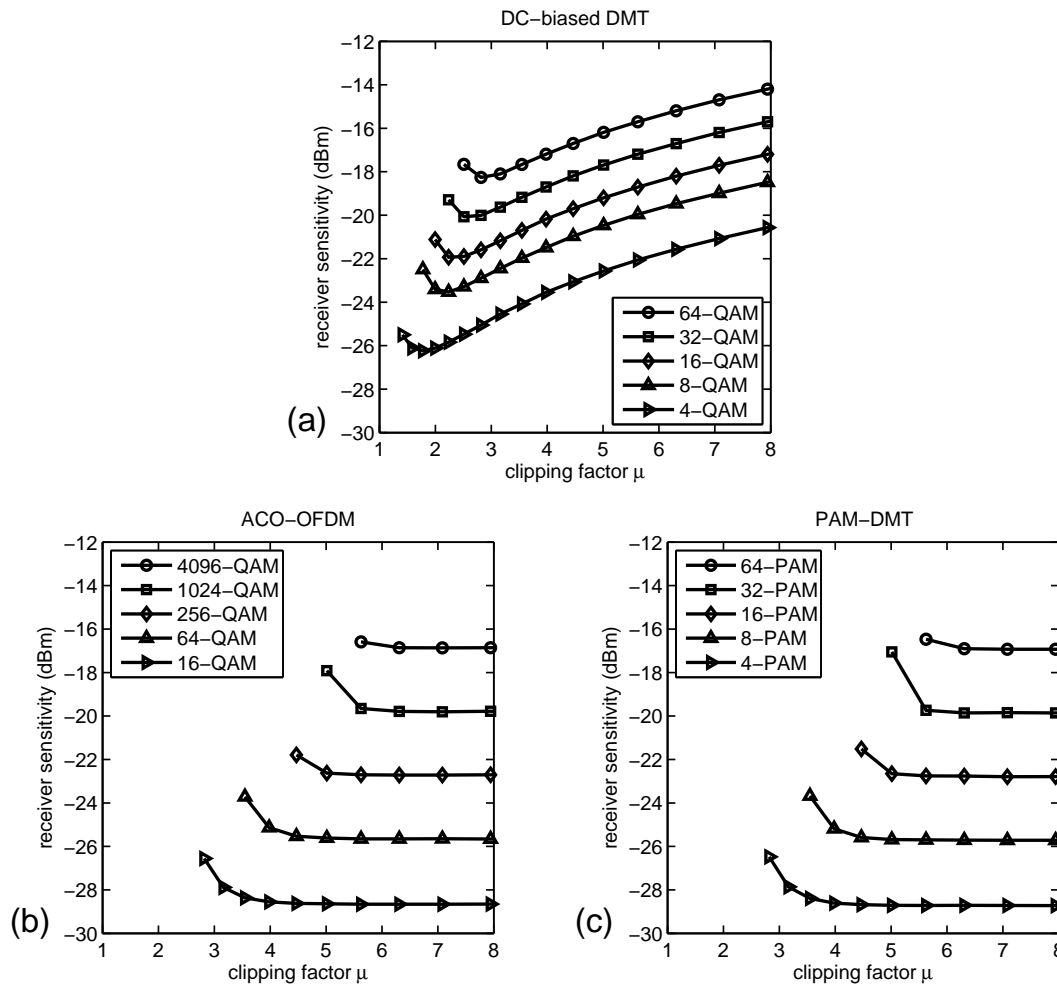
Figure 8.3: Receiver sensitivity (optical dBm) for a system BER of 10^{-3} vs. clipping level for (a) DC-biased DMT (b) ACO-OFDM (c) PAM-DMT.

to M^2-QAM of ACO-OFDM. In Fig. 8.3a, performance degradation is observed for large values of μ in DC-biased DMT due to the effect of photodetector noise. For small values of μ, clipping noise dominates and causes also performance loss. ACO-OFDM and PAM-DMT exhibit only significant performance degradation for small values of μ (see Fig. 8.3b-c), because the mean optical power P_{opt} does not depend on μ for large values.

Fig. 8.4 summarizes the results of Fig. 8.3 by plotting the optical receiver sensitivity for a system BER of 10^{-3} at the optimum values of μ against the normalized bandwidth/bit-rate. These optimum values of μ correspond to the minimum re-

Figure 8.4: Receiver sensitivity (optical dBm) against normalized bandwidth/bit-rate for a system BER $= 10^{-3}$.

quired receiver sensitivity values given in Fig. 8.3. The parameters for normalizing bandwidth/bit-rate are chosen as in [30], for comparison purposes. For values larger than 0.2, ACO-OFDM and PAM-DMT perform better than DC-biased DMT, confirming the results shown in [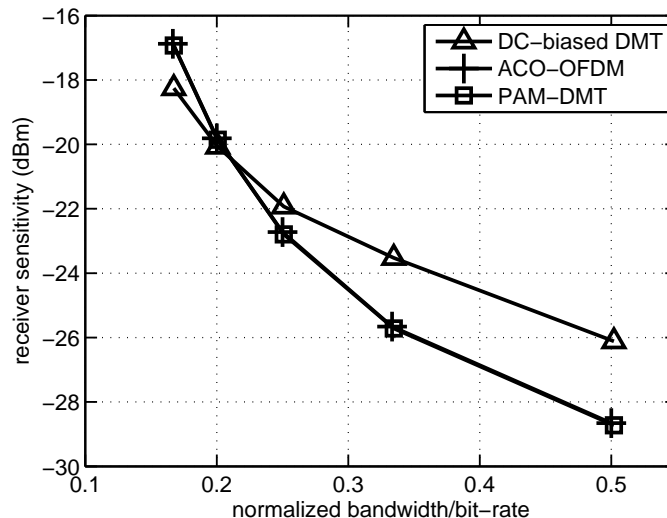30] for ACO-OFDM. It should be noted that these results do not take the non-linearity in the current to optical power conversion process into account. Finally, notice that both PAM-DMT and ACO-OFDM show identical performance. This is because in ACO-OFDM, half of the subcarriers are filled, but in PAM-DMT half of the quadrature is filled. Therefore, the same performance is obtained when a flat frequency response is considered.

8.2.3 Comparison of PAM-DMT and ACO-OFDM

An important advantage of OFDM and DMT is the ability to adapt the modulation format of each subcarrier to the SNR of the channel, commonly known as bit-loading. In Fig. 8.5, a comparison between PAM-DMT and ACO-OFDM is made for an IM/DD channel with Gaussian low-pass response, where its -3 dB bandwidth is set to 0.5 times the signal bandwidth (see Fig. 8.5a). Rate-adaptive bit-loading as in [9] is performed for both PAM-DMT and ACO-OFDM, where a slightly modified power allocation algorithm is employed for PAM-DMT due to the

Chapter 8. Pulse Amplitude Modulated DMT

use of PAM instead of QAM symbols. Observe from Fig. 8.5a ($N = 32$ subcarriers) that ACO-OFDM cannot adapt as well to the Gaussian channel response as PAM-DMT because only half of the subcarriers in ACO-OFDM are used. Consider e.g. subcarriers 1 and 2, where 7 bits are allocated for ACO-OFDM and 2×4 bits are allocated for PAM-DMT, resulting in a lower total number of bits allocated in case of ACO-OFDM. This effect is more significant for small values of N, as shown Fig. 8.5b, where the ratio of maximum achievable bit-rate at BER $= 10^{-3}$ for PAM-DMT to ACO-OFDM $b_{PAM-DMT}/b_{ACO-OFDM}$ is plotted for different number of subcarriers N used. The mean received optical power and clipping factor μ are set to -22 dBm and 8 respectively. For $N = 32$, 1.21 times higher bit-rates can be achieved with bit-loading for PAM-DMT compared to ACO-OFDM.
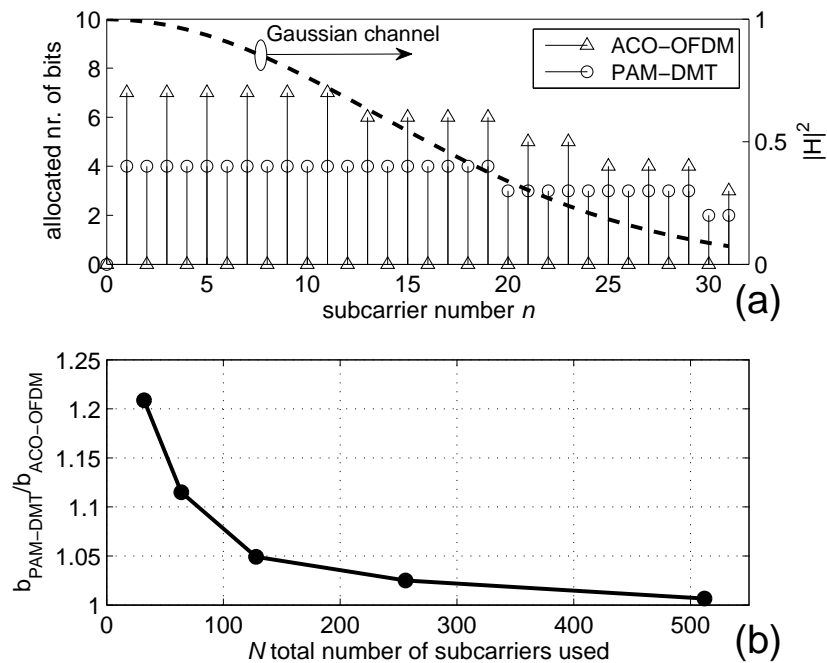
Figure 8.5: Influence of Gaussian channel response on (a) the bit-allocation per subcarrier for a 32-subcarrier system with bit-loading; (b) achievable bit-rate of PAM-DMT over ACO-OFDM for different number of subcarriers used.

146

8.3   Summary

Simulation results show that for an IM/DD channel with a flat frequency response, PAM-DMT and ACO-OFDM employing asymmetrical clipping achieve identical performance and are better than DC-biased DMT for normalized bandwidth/bitrate values larger than 0.2. For a Gaussian low-pass channel response, ACO-OFDM with bit-loading does not adapt as well to the channel as PAM-DMT due to the use of only odd-numbered subcarriers, resulting in better performance for PAM-DMT especially when a small number of subcarriers are used. Finally, it is important to note that multi-path dispersion can break the symmetry at zero for both ACO-OFDM and PAM-DMT and should be further investigated in detail. However, since the symbol period is always chosen to be much longer than the value of dispersion, this effect is reduced to a minimum.

CHAPTER 9
CONCLUSIONS AND
RECOMMENDATIONS

The application of DMT modulation in an optical IM/DD channel for short-range optical communications was proposed and investigated in this thesis. The communication channels considered include POF, silica MMF, and optical wireless (based on white-light LEDs). The reason to investigate the use of DMT is because of its advantages such as high spectral efficiency, the ability to adapt to channel conditions with bit-loading, and the use of cyclic prefix for compensating dispersion. Naturally, DMT also have disadvantages such as high crest factor values and high implementation complexity, which were also investigated in this thesis.

First, the principle of DMT was explained and it was shown that the combination of a long DMT frame length and a cyclic prefix can be used to guard against inter-frame interference resulting from dispersion. Dispersion in IM/DD short-range optical communications can be characterized as modal dispersion resulting from the use of multimode fibers, slow rise and fall times of transmitter and receiver components (bandwidth limitation), and in the case of optical wireless, also from reflections from walls and other objects.

Furthermore, the channel capacity of an optical IM/DD channel was investigated in Chapter 4 by use of the water-filling method. This resulted in an analytical model that can be used to calculate the capacity of a general IM/DD channel, divided into

two parts:

- a channel frequency response dependent part, which is a function of SNR_{norm}, and

- a noise dependent part given by SNR_{norm} (see equation (4.22)).

Besides standard parameters of channel attenuation, signal bandwidth, mean transmitted optical power, and receiver noise given by NEP, it was noticed that the normalized signal-to-noise ratio SNR_{norm} of an optical IM/DD channel is also defined by the crest factor μ of the transmit signal. This important result characterizes the maximum achievable capacity in an optical IM/DD channel. It was found that in the presence of only receiver noise, lower crest factor values (with a minimum of 1) will result in larger capacity in an optical IM/DD channel.

In the case of DMT transmission, SNR_{norm} does not only depend on receiver thermal noise, but is also dependent on quantization noise and clipping distortion, which are both modeled as white noise. Due to the large crest factor of DMT signals, clipping is unavoidable. When a DMT signal is clipped to achieve lower crest factor values, the amount of clipping distortion will increase, which is considered as noise. Therefore, lower crest factor values (as a result of symmetrical clipping) do not naturally lead to larger capacity with DMT in an optical IM/DD channel. In the presence of clipping, an optimum value for μ exists, that optimizes the relation of receiver, quantization, and clipping noise, achieving highest capacity for DMT over an optical IM/DD channel.

It should be noted that the capacity analysis of DMT over an optical IM/DD channel is based on the assumption that the crest factor of the DMT signal is reduced by clipping, and that the resulting distortion is regarded as noise. However, if it is possible to employ distortion-less crest factor reduction techniques, or retrieve information from clipping distortion so that crest factor is reduced without adding noise, the maximum achievable capacity of DMT transmission over an optical IM/DD channel can be increased. Naturally, such solutions come at the cost of higher implementation complexity and the question remains whether these can be realized in practice.

Next to channel capacity analysis, the analytical modeling of DMT clipping noise was also demonstrated to correspond well to simulation results employing clipping.

Given the system parameters, optimum clipping-limited crest factor values for best DMT performance over an optical IM/DD channel can be predicted analytically by making use of this model. A direction for further work might be to validate this model with experimental results.

Furthermore, in Chapter 5, it was shown (both by simulations and experiments) that DMT performance gets better for larger number of subcarriers. The most important reason is that for a larger number of subcarriers, the frequency-selective transmission channel can be better decomposed into frequency-flat subchannels so that zero-forcing equalization at the DMT demodulator can be more effective. Additionally, when combined with bit-loading, the constellation size (number of allocated bits) and power per subchannel can be more finely adapted to its corresponding SNR in order to achieve maximum transmission rate.

An interesting observation from Chapter 5 is that when a DMT signal is used to modulate an optical transmitter such as a DFB laser, a large dynamic range (and modulation index) can be used for the driving current without significant signs of laser non-linearity effects (measured at a BER of 10^{-3}). One possible reason for this is that non-linearity in the current-to-optical power conversion process mainly occurs due to saturation effects because insufficient holes and electrons are able to recombine in a timely manner. This however, is a relatively slow process and is more evident not only for slow-varying, but also for non-dynamic, periodic (low crest factor) modulation signals.

Multi-carrier waveforms such as DMT, however, are characterized by their highly dynamic amplitude values, leading to large crest factors. Statistically, large peaks do not occur very often and are random in nature (non-periodic). Due to these infrequent and irregular peaks, saturation effects are less likely to take place in the current-to-optical conversion process because sufficient holes and electrons are often present for recombination. Therefore, non-linearity issues are less pronounced and might be less critical for DMT transmission, when compared to other modulation formats. More detailed investigation of this issue is recommended for further work, and might lead to an additional advantage of using DMT in optical IM/DD channels.

In Chapter 6, experiments regarding the application of DMT in POF, silica MMF, and optical wireless channels were presented and system performance limits were investigated. One of the most interesting results is the ability to use an RC-

LED to transmit data at a rate of 1 Gbit/s over 50 m of SI-POF, which is severely limited in bandwidth. Bit-rates >1 Gbit/s were also achieved for shorter distances of 5 m to demonstrate the high spectral efficiency of DMT to achieve up to almost 10 Gbit/s transmission using transmission bandwidths of 2 to 3 GHz. For PF-GI-POF, optimum DMT transmission parameters were experimentally investigated, resulting in bit-rates of up to 47 Gbit/s over a distance of 100 m.

For silica MMF, it was shown that DMT in combination with bit-loading can compensate for relative intensity noise in low-cost multimode VCSELs. However, this was only done statically, as a proof of concept. Further work on showing real-time adaptation to such time-varying impairments with bit-loading is recommended. Additionally, it is also interesting to investigate the possibility to use bit-loading to adapt to physical variations in the link, such as fiber bending, launching offset, connector misalignment, modal noise, etc. Moreover, demodulation of DMT waveforms results in a lot of information over the transmission channel, so that performance monitoring can also be a very interesting topic to investigate. Based on channel parameters, one might be able to associate variations of these parameters with certain physical impairments so that the user can be notified when a link is not functioning correctly and where the problem might be.

A further interesting topic is optical wireless, where experimental investigations showed that bit-rates of up to 100 Mbit/s can be possible with phosphorescent white-light LEDs. Such LEDs are nowadays gaining tremendous popularity for illumination purposes due to advantages such as high efficiency, long life time expectancy, and potentially low costs. The dual use of such LEDs for illumination and information transfer proves to be an interesting application.

In Chapter 7, an approach to implement a real-time 1.25 Gbit/s DMT transmitter was presented. Its transmission performance results were evaluated in terms of received signal quality. This was done as a first step to understand and investigate underlying issues of DMT concerning hardware design and complexity. One important issue to solve in further work is to define the maximum number of subcarriers (or FFT size) that can be implemented in a realistic DMT system. It will be interesting to know how this number scales with regard to the desired bit-rate/processing speed. Another recommendation for further work is to characterize the complexity of various offline processing algorithms and to find out what implications the desired

bit-rate/processing speed has on the practical realization of such algorithms. Moreover, most software used for offline processing do not take into account the impact of fixed-point implementation, so that precise floating-point arithmetic operations are used to perform signal modulation and demodulation. This results often in very optimistic performance values. Further work should study this issue and find a way to relate performance degradation to the precision of fixed-point arithmetic used.

Last but not least, in Chapter 8, the idea of PAM-DMT was proposed with regard to transmission over an optical IM/DD channel and its performance was investigated with simulations. The results showed that for a channel with flat-frequency response, PAM-DMT achieves identical performance results with ACO-OFDM. This is because in ACO-OFDM, half of the subcarriers are filled, but in PAM-DMT half of the quadrature is filled. For the same channel, when small constellations of up to 32-QAM are used, the optical receiver sensitivity required by PAM-DMT and ACO-OFDM to achieve a BER of $1 \cdot 10^{-3}$ is lower than the standard DC-biased DMT in an optical IM/DD channel. In this case, this means that PAM-DMT and ACO-OFDM achieve better performance. It should be noted that this conclusion results from the assumption that the transmission channel is limited by the mean optical power, i.e. high peak optical power values do not saturate. Further study is required and recommended to verify if this is an appropriate assumption for the optical IM/DD channel, taking into account the conclusions in Chapter 5.3.

In the case of a frequency-selective channel, PAM-DMT using bit-loading allows more accurate allocation of bits (and power) per subcarrier due to the fact that all subcarriers can be modulated with data, in comparison with ACO-OFDM. However, this effect is only significant when a low number of subcarriers is used. Finally, the effects of channel impulse response should be studied for PAM-DMT (and ACO-OFDM) to see if the symmetry property (which allows clipping of negative values) can be broken so that degradation in signal quality occurs.

In conclusion, short-range optical communications is an exciting alternative field for optical telecommunications, which is traditionally dominated by long-haul single-mode fiber transmission. However, the biggest hurdle for short-range optical communications is the (fierce) competition with traditional transmission media such as copper cables and wireless communications, which have already established themselves for decades and have found wide adoption in the market, resulting in large

economies of scale. The addition of digital signal processing schemes like DMT in order to make short-range optical systems more robust and achieve higher bit-rates might from a research point of view be very interesting, but does drive the costs of such systems up.

In a highly (price-) competitive market such as mass-consumer applications, the complexity (and therefore price) of such digital signal processing techniques should be well-chosen to optimize certain key factors such as price, energy-efficiency, ease of use, quality of service, transmission speed, novel application scenarios, which in the end will determine the success of short-range optical communications.

Appendix A
Shannon Capacity Calculations

This appendix shows the main mathematical passages that lead to the optical IM/DD channel capacity results for the Gaussian and first-order low-pass channel responses given in Chapter 4 by equations (4.24) and (4.29) respectively.

A.1 Gaussian Low-Pass Channel Response

This section shows the mathematical passages that lead to the Gaussian low-pass channel capacity result as shown in (4.24). First, an analytical expression for the capacity in terms of the parameter ξ is found. Starting from (4.9) and combining it with (4.11), (4.19) and (4.20), the following is obtained:

$$C = \int_{-\xi}^{\xi} \frac{1}{2} \log_2 \left[1 + \frac{\nu - G_n(f)}{G_n(f)} \right] df \qquad \text{(A.1a)}$$

$$= \int_{-\xi}^{\xi} \frac{1}{2} \log_2 \frac{\nu}{G_n(f)} df \qquad \text{(A.1b)}$$

$$= \int_{-\xi}^{\xi} \frac{1}{2} \log_2 \frac{e^{\left(\frac{\xi}{f_0}\right)^2}}{e^{\left(\frac{f}{f_0}\right)^2}} df \qquad \text{(A.1c)}$$

$$= \frac{1}{2\ln(2)} \int_{-\xi}^{\xi} \left(\frac{\xi^2 - f^2}{f_0^2} \right) df \qquad \text{(A.1d)}$$

$$= \frac{2}{3\ln(2)} \frac{\xi^3}{f_0^2} . \qquad \text{(A.1e)}$$

Chapter A. Shannon Capacity Calculations

By introducing $\eta = \xi/f_0$, the expression for the capacity can be written as:

$$
\begin{aligned}
C &= \frac{2}{3\ln(2)} f_0 \cdot \eta^3 \\
&= \frac{2}{3\ln(2)\sqrt{\ln(2)}} f_{3dB} \cdot \eta^3 .
\end{aligned}
\tag{A.2}
$$

The only remaining point is the evaluation of the quantity η. Starting from (4.21) and rewriting it introducing the parameter η results in:

$$
\frac{\text{NEP}^2}{2\alpha^2} \int_{-\xi}^{+\xi} \left[e^{\left(\frac{\xi}{f_0}\right)^2} - e^{\left(\frac{f}{f_0}\right)^2} \right] df = \left(\frac{P_{mean}}{\mu} \right)^2
\tag{A.3a}
$$

$$
\frac{\text{NEP}^2}{2\alpha^2} \left(2 f_0 \eta e^{\eta^2} - f_0 \int_{-\eta}^{+\eta} e^{w^2} dw \right) = \left(\frac{P_{mean}}{\mu} \right)^2
\tag{A.3b}
$$

$$
\frac{\text{NEP}^2}{2\alpha^2} \cdot 2 f_0 \left(\eta e^{\eta^2} - \frac{1}{2} \int_{-\eta}^{+\eta} e^{w^2} dw \right) = \left(\frac{P_{mean}}{\mu} \right)^2
\tag{A.3c}
$$

$$
\eta e^{\eta^2} - \frac{1}{2} \int_{-\eta}^{+\eta} e^{w^2} dw = \frac{\alpha^2 \cdot P_{mean}^2}{\text{NEP}^2 \cdot f_0 \cdot \mu^2}
\tag{A.3d}
$$

$$
\eta e^{\eta^2} - \frac{1}{2} \int_{-\eta}^{+\eta} e^{w^2} dw = \text{SNR}_{\text{norm}} .
\tag{A.3e}
$$

This last equation is the key equation for calculating the Shannon capacity of a Gaussian low-pass optical IM/DD channel. It is to be meant as an equation in the unknown η. The only input to this equation is SNR_{norm}, so that in the end η is simply a given function of SNR_{norm}, i.e., $\eta = g(\text{SNR}_{\text{norm}})$. This function $g(\cdot)$ does not have a closed-form expression, but involving very smooth and regular functions can be very easily evaluated numerically.

A.2 First-Order Low-Pass Channel Response

This section shows the mathematical passages that lead to the first-order low-pass channel capacity result as shown in (4.29). Starting again from (4.9), the analytical expression for the capacity in terms of the parameter ξ is found by combining

it with (4.26b), resulting in:

$$C = \int_{-\xi}^{\xi} \frac{1}{2} \log_2 \left[1 + \frac{\nu - G_n(f)}{G_n(f)} \right] df \tag{A.4a}$$

$$= \int_{-\xi}^{\xi} \frac{1}{2} \log_2 \frac{\nu}{G_n(f)} df \tag{A.4b}$$

$$= \int_{-\xi}^{\xi} \frac{1}{2} \log_2 \frac{1 + \left(\frac{\xi}{f_0} \right)^2}{1 + \left(\frac{f}{f_0} \right)^2} df \tag{A.4c}$$

$$= \frac{1}{2 \ln(2)} \int_{-\xi}^{\xi} \ln \left[1 + \left(\frac{\xi}{f_0} \right)^2 \right] - \ln \left[1 + \left(\frac{f}{f_0} \right)^2 \right] df \tag{A.4d}$$

$$= \frac{1}{2 \ln(2)} \left[\ln \left(\frac{\xi^2 + f_0{}^2}{f^2 + f_0{}^2} \right) f + 2f - 2f_0 \arctan \left(\frac{f}{f_0} \right) \right]_{-\xi}^{\xi} \tag{A.4e}$$

$$= \frac{2}{\ln(2)} \left[\xi - f_0 \arctan \left(\frac{\xi}{f_0} \right) \right]. \tag{A.4f}$$

The value of ξ is found by evaluating (4.27):

$$\frac{\text{NEP}^2}{2\alpha^2} \int_{-\xi}^{+\xi} \left[\left(\frac{\xi}{f_0} \right)^2 - \left(\frac{f}{f_0} \right)^2 \right] df = \left(\frac{P_{mean}}{\mu} \right)^2 \tag{A.5a}$$

$$\frac{\text{NEP}^2}{2\alpha^2} \left[\left(\frac{\xi}{f_0} \right)^2 f - \frac{f_0}{3} \left(\frac{f}{f_0} \right)^3 \right]_{-\xi}^{\xi} = \left(\frac{P_{mean}}{\mu} \right)^2 \tag{A.5b}$$

$$\frac{4}{3} \frac{\xi^3}{f_0^2} = \frac{\alpha^2 \cdot P_{mean}^2}{\text{NEP}^2 \cdot f_0 \cdot \mu^2} \cdot 2f_0 \tag{A.5c}$$

$$\frac{2}{3} \frac{\xi^3}{f_0^3} = \text{SNR}_{\text{norm}} \tag{A.5d}$$

$$\frac{\xi}{f_0} = \sqrt[3]{\frac{3}{2} \text{SNR}_{\text{norm}}}. \tag{A.5e}$$

Substituting (A.5e) in (A.4f) gives:

$$C = \frac{2}{\ln(2)} \left[\xi - f_0 \arctan \left(\frac{\xi}{f_0} \right) \right]$$

$$= \frac{2}{\ln(2)} \left(f_0 \sqrt[3]{\frac{3}{2} \text{SNR}_{\text{norm}}} - f_0 \arctan \sqrt[3]{\frac{3}{2} \text{SNR}_{\text{norm}}} \right) \tag{A.6}$$

$$= f_0 \frac{2}{\ln(2)} \left(\sqrt[3]{\frac{3}{2} \text{SNR}_{\text{norm}}} - \arctan \sqrt[3]{\frac{3}{2} \text{SNR}_{\text{norm}}} \right)$$

which is a closed-form expression for the capacity of a first-order low-pass optical IM/DD channel, given again as a function of SNR_{norm}.

Appendix B
Modulation Index and Optical Modulation Amplitude

This appendix presents the definition of modulation index (MI) and optical modulation amplitude (OMA) as used to describe the properties of DMT modulation in the optical IM/DD channel.
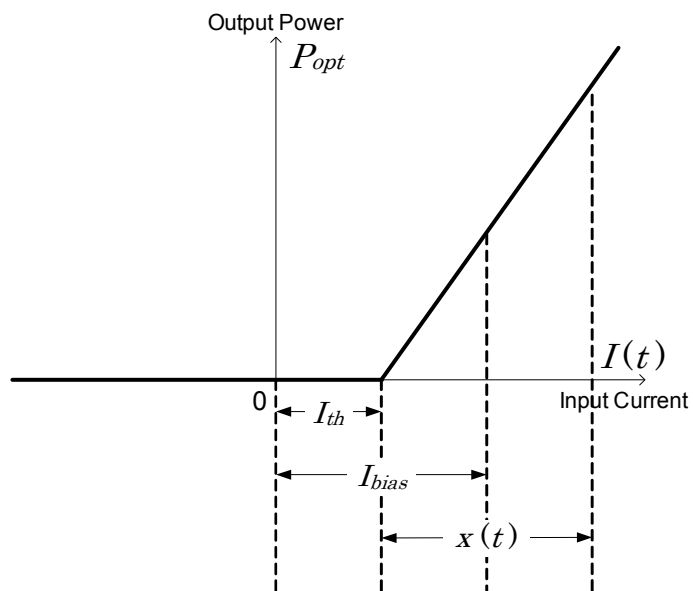

Figure B.1: Ideal optical intensity modulator model.

Chapter B. Modulation Index and Optical Modulation Amplitude

B.1 Modulation Index

The model of an ideal linear optical intensity modulator is depicted in Fig. B.1. This model assumes that no optical power is emitted when the driving current is below the threshold value I_{th}, and the optical power emission is linearly proportional to the driving current when this current is above I_{th}. Moreover, there is no saturation effect for infinite values of the driving current. Based on this model, the instantaneous transmitted optical power $P_{opt}(t)$ in $[\text{W}_\text{o}]$ can be written as a function of its driving current by

$$P_{opt}(t) = \beta \left[I_{bias} + x(t) \right] \tag{B.1}$$

where β is the quantum efficiency of the electrical current-to-optical power conversion given in $[\text{W}_\text{o}/\text{A}]$ and $x(t)$ is the time-varying modulation current in $[\text{A}]$ which is assumed to be zero-mean and bipolar. I_{bias} is the bias current given in $[\text{A}]$. When x_{peak} is defined to be the peak amplitude of $x(t)$, the modulation index is written as

$$\text{MI} = \frac{x_{peak}}{I_{bias} - I_{th}} \tag{B.2}$$

which is the definition of modulation index used in this thesis.

B.2 Optical Modulation Amplitude

Typically, the optical modulation amplitude (OMA) is used for characterizing binary on-off keying modulation systems in optical IM/DD channels. It is defined as [56, 57] the difference in optical power between the high P_1 and the low level P_0, given by

$$\text{OMA} = P_1 - P_0 \tag{B.3}$$

where OMA, P_1, and P_0 are given in $[\text{mW}_\text{o}]$. Because it is a wide-spread and commonly-used parameter, it is also adopted in this thesis to characterize the application of DMT over an optical IM/DD channel. In the case of the optical intensity modulator model given in Fig. B.1, the following is defined for

$$P_1 = \beta \left\{ I_{bias} + \max \left[x(t) \right] \right\} \tag{B.4a}$$
$$= \beta \left(I_{bias} + x_{peak} \right) \tag{B.4b}$$

and

$$P_0 = \beta \left\{ I_{bias} + \min \left[x(t) \right] \right\} \tag{B.5a}$$

$$= \beta \left(I_{bias} - x_{peak} \right) . \tag{B.5b}$$

The calculation of OMA remains the same as given in (B.3). If the mean optical power of the IM/DD channel is also known, the modulation index can be calculated from the OMA. The advantage of using OMA is that all parameters that define how the intensity modulator is driven are related to the optical power in the IM/DD channel, which can be easily measured. It is also possible to define OMA given in optical [dBm], with

$$\text{OMA [dBm]} = 10 \log_{10} \left(\text{OMA [mW}_\text{o}] \right) . \tag{B.6}$$

List of Abbreviations

AC:	Alternating current
ACO-OFDM:	Asymmetrically-clipped optical OFDM
AMOOFDM:	Adaptively-modulated optical OFDM
A/D:	Analog-to-digital
ADC:	Analog-to-digital converter
ADSL:	Asymmetric Digital Subscriber Line
AMGDM:	Angular mode group diversity multiplexing
ASIC:	Application-specific integrated circuit
AWG:	Arbitrary waveform generator
AWGN:	Additive white Gaussian noise
BER:	Bit-error ratio
CATV:	Cable television
CP:	Cyclic prefix
D/A:	Digital-to-analog
DAC:	Digital-to-analog converter
DC:	Direct current
DD:	Direct detection
DEMUX:	Demultiplexer
DFB:	Distributed feedback (laser)
DMA:	Differential mode attenuation
DMT:	Discrete multitone
DSL:	Digital Subscriber Line
DSO:	Digital storage oscilloscope
DVB-T:	Terrestrial Digital Video Broadcasting
DVD:	Digital video disc
EMD:	Equilibrium mode distribution
FEC:	Forward error correction
FFT:	Fast Fourier transform
FPGA:	Field programmable gate array
GI-POF:	Graded-index plastic optical fiber
GRIN:	Graded-index
HDMI:	High-Definition Multimedia Interface
HDTV:	High-definition television
IEEE:	Institute of Electrical and Electronics Engineers
IFFT:	Inverse fast Fourier transform
IM:	Intensity modulation

List of Abbreviations

IM/DD:	Intensity modulation and direct detection
IPTV:	Internet Protocol television
IrDA:	Infrared Data Association
ISI:	Inter-symbol interference
IQ:	In-phase and quadrature-phase
LAN:	Local area network
LD:	Laser diode
LED:	Light-emitting diode
MI:	Modulation index
MIMO:	Multiple input multiple output
MLSE:	Maximum likelihood sequence estimation
MMF:	Multimode fiber
MOST:	Multimedia-Oriented System Transport
NA:	Numerical aperture
NEP:	Noise equivalent power
NRZ:	Non-return-to-zero
OFDM:	Orthogonal frequency division multiplexing
OMA:	Optical modulation amplitude
PAM:	Pulse-amplitude modulation
PAM-DMT:	Pulse-amplitude-modulated discrete multitone
PAPR:	Peak-to-average power ratio
PD:	Photodetector
PF-GI-POF:	Perfluorinated graded-index plastic optical fiber
PIN:	Positive-intrinsic-negative (diode)
PMMA:	Poly-methyl-methacrylate
POF:	Plastic optical fiber
PRBS:	Pseudo-random binary sequence
PROFINET:	Process Field Network
QAM:	Quadrature amplitude modulation
RC-LED:	Resonant-cavity light-emitting diode
RIN:	Relative intensity noise
rms:	Root-mean-square
Rx:	Receiver
SI-POF:	Step-index plastic optical fiber
SMF:	Single-mode fiber
SNR:	Signal-to-noise ratio
TIA:	Trans-impedance amplifier
Tx:	Transmitter
USB:	Universal Serial Bus
UTP:	Unshielded twisted pair
VCSEL:	Vertical-cavity surface-emitting lasers

VDSL: Very high-speed Digital Subscriber Line
VoIP: Voice over Internet Protocol
VSA: Vector-signal analyzer
VSG: Vector-signal generator
WiFi: Wireless Fidelity
WiMAX: Worldwide Interoperability for Microwave Access
WLAN: Wireless local area network

Bibliography

[1] R. van Nee and R. Prasad, *OFDM for Wireless Multimedia Communications.* Artech House, 2000.

[2] Y. Li and G. L. Stuber, Eds., *Orthogonal Frequency Division Multiplexing for Wireless Communications.* Springer, 2006.

[3] *Asymmetric Digital Subscriber Line (ADSL) Transceivers*, ITU Std. G.992.1, July 1999.

[4] J. M. Cioffi. (2008, June) Advanced Digital Communication (Course Reader). [Online]. Available: http://www.stanford.edu/class/ee379c

[5] D. J. G. Mestdagh, P. M. P. Spruyt, and B. Biran, "Effect of Amplitude Clipping in DMT-ADSL Transceivers," *Electronics Letters*, vol. 29, no. 15, pp. 1354–1355, July 1993.

[6] Intel Corp. (2007, September) Industry Leaders Develop Superspeed USB Interconnect. [Online]. Available: http://www.usb.org/home

[7] Lightwave online. (2006, 17th May) Infineon unveils POF to Ethernet transceiver reference design for home networking. [Online]. Available: http://lw.pennnet.com/articles

[8] S. Randel, S. C. J. Lee, B. Spinnler, F. Breyer, H. Rohde, J. Walewski, A. M. J. Koonen, and A. Kirstdter, "1 Gbit/s Transmission with 6.3 bit/s/Hz Spectral Efficiency in a 100 m Standard 1 mm Step-Index Plastic Optical Fiber Link Using Adaptive Multiple Sub-Carrier Modulation," in *European Conference on Optical Communications*, September 2006.

[9] S. C. J. Lee, F. Breyer, S. Randel, R. Gaudino, G. Bosco, A. Bluschke, M. Matthews, P. Rietzsch, R. Steglich, H. P. A. van den Boom, and A. M. J. Koonen, "Discrete Multitone Modulation for Maximizing Transmission Rate in Step-Index Plastic Optical Fibers," *IEEE/OSA Journal of Lightwave Technology*, vol. 27, no. 11, pp. 1503–1513, June1, 2009.

BIBLIOGRAPHY

[10] F. Breyer, S. C. J. Lee, S. Randel, and N. Hanik, "1.25 Gbit/s Transmission over up to 100 m Standard 1 mm Step-Index Polymer Optical Fibre using FFE or DFE Equalisation Schemes," in *European Conference on Optical Communications*, September 2007.

[11] D. Delbeke, R. Bockstaele, P. Bienstman, R. Baets, and H. Benisty, "High-Efficiency Semiconductor Resonant-Cavity Light-Emitting Diodes: A Review," *IEEE Journal of Selected Topics in Quantum Electronics*, vol. 8, no. 2, pp. 189–206, Mar/Apr 2002.

[12] [Online]. Available: http://www.firecomms.com/tech-RCLED.html

[13] T. Wipiejewski, T. Moriarty, V. Hung, P. Doyle, G. Duggan, D. Barrow, B. Mc-Garvey, M. O'Gorman, T. Calvert, M. Maute, V. Gerhardt, and J. D. Lambkin, "Gigabit/s in the Home with Plugless Plastic Optical Fiber (POF) Interconnects," in *Electronics System-Integration Technology Conference, 2008. ESTC 2008. 2nd*, Sept. 2008, pp. 1263–1266.

[14] O. Kwon and C.-W. Park, "Modification of RI profile for the Reduction of Bending Loss of a PMMA GI-POF," in *International Conference on Polymer Optical Fiber*, August 2008.

[15] K. Koike and Y. Koike, "Design of Low-Loss Graded-Index Plastic Optical Fiber Based on Partially Fluorinated Methacrylate Polymer," *IEEE/OSA Journal of Lightwave Technology*, vol. 27, no. 1, pp. 41–46, Jan.1, 2009.

[16] T. Ishigure, E. Nihei, Y. Koike, C. E. Forbes, L. LaNieve, R. Straff, and H. A. Deckers, "Large-Core, High-Bandwidth Polymer Optical Fiber for Near Infrared Use," *IEEE Photonics Technology Letters*, vol. 7, no. 4, pp. 403–405, Apr 1995.

[17] [Online]. Available: http://www.hdmi.org/

[18] A. Flatman. (2004, March) In-Premises Optical Fibre Installed Base Analysis to 2007. [Online]. Available: www.ieee802.org/3/10GMMFSG/public/mar04/flatman_1_0304.pdf

[19] [Online]. Available: http://www.irda.org/

[20] [Online]. Available: http://www.vlcc.net/

[21] J. Grubor, S. Randel, K.-D. Langer, and J. W. Walewski, "Broadband Information Broadcasting Using LED-Based Interior Lighting," *IEEE/OSA Journal of Lightwave Technology*, vol. 26, no. 24, pp. 3883–3892, Dec.15, 2008.

[22] J. Grubor, S. C. J. Lee, K.-D. Langer, T. Koonen, and J. W. Walewski, "Wireless high-speed data transmission with phosphorescent white-light LEDs," in *European Conference on Optical Communications*, September 2007, p. PD3.6.

[23] J. Armstrong, "OFDM for Optical Communications," *IEEE/OSA Journal of Lightwave Technology*, vol. 27, no. 3, pp. 189–204, Feb.1, 2009.

[24] J. M. Cioffi. (2008, June) A Multicarrier Primer. [Online]. Available: http://www-isl.stanford.edu/~cioffi/pdf/multicarrier.pdf

[25] S. C. J. Lee, F. Breyer, S. Randel, H. P. A. van den Boom, and A. M. J. Koonen, "High-Speed Transmission over Multimode Fiber using Discrete Multitone Modulation," *OSA Journal of Optical Networking*, vol. 7, no. 2, pp. 183–196, 2008.

[26] S. C. J. Lee, F. Breyer, S. Randel, O. Ziemann, H. P. A. van den Boom, and A. M. J. Koonen, "Low-Cost and Robust 1 GBit/s Plastic Optical Fiber Link Based on Light-Emitting Diode Technology," in *Optical Fiber Communication Conference*, February 2008.

[27] G. D. Bergland, "Numerical Analysis: A Fast Fourier Transform Algorithm for Real-Valued Series," *Commun. ACM*, vol. 11, no. 10, pp. 703–710, 1968.

[28] H. Sorensen, D. Jones, M. Heideman, and C. Burrus, "Real-valued fast Fourier transform algorithms," *IEEE Transactions on Acoustics, Speech and Signal Processing*, vol. 35, no. 6, pp. 849–863, June 1987.

[29] J. M. Tang and K. A. Shore, "Maximizing the Transmission Performance of Adaptively Modulated Optical OFDM Signals in Multimode-Fiber Links by

Optimizing Analog-to-Digital Converters," *IEEE/OSA Journal of Lightwave Technology*, vol. 25, no. 3, pp. 787–798, March 2007.

[30] J. Armstrong and B. J. C. Schmidt, "Comparison of Asymmetrically Clipped Optical OFDM and DC-Biased Optical OFDM in AWGN," *IEEE Communications Letters*, vol. 12, no. 5, pp. 343–345, May 2008.

[31] J. M. Tang, P. M. Lane, and K. A. Shore, "High-Speed Transmission of Adaptively Modulated Optical OFDM Signals Over Multimode Fibers Using Directly Modulated DFBs," *IEEE/OSA Journal of Lightwave Technology*, vol. 24, pp. 429–441, 2006.

[32] S. L. Jansen, I. Morita, T. C. W. Schenk, N. Takeda, and H. Tanaka, "Coherent Optical 25.8-Gb/s OFDM Transmission Over 4160-km SSMF," *IEEE/OSA Journal of Lightwave Technology*, vol. 26, no. 1, pp. 6–15, Jan.1, 2008.

[33] B. J. C. Schmidt, A. J. Lowery, and J. Armstrong, "Experimental Demonstrations of Electronic Dispersion Compensation for Long-Haul Transmission Using Direct-Detection Optical OFDM," *IEEE/OSA Journal of Lightwave Technology*, vol. 26, no. 1, pp. 196–203, Jan.1, 2008.

[34] W. Shieh, X. Yi, and Y. Tang, "Transmission Experiment of Multi-Gigabit Coherent Optical OFDM Systems over 1000km SSMF Fibre," *Electronics Letters*, vol. 43, no. 3, pp. 183–184, 1 2007.

[35] D. J. G. Mestdagh and P. M. P. Spruyt, "A Method to Reduce the Probability of Clipping in DMT-Based Transceivers," *IEEE Transactions on Communications*, vol. 44, no. 10, pp. 1234–1238, Oct 1996.

[36] R. W. Bauml, R. F. H. Fischer, and J. B. Huber, "Reducing the Peak-to-Average Power Ratio of Multicarrier Modulation by Selected Mapping," *Electronics Letters*, vol. 32, no. 22, pp. 2056–2057, 1996.

[37] P. Van Eetvelt, G. Wade, and M. Tomlinson, "Peak to Average Power Reduction for OFDM Schemes by Selective Scrambling," *Electronics letters*, vol. 32, no. 21, pp. 1963–1964, 1996.

[38] S. H. Muller and J. B. Huber, "OFDM with Reduced Peak-to-Average Power Ratio by Optimum Combination of Partial Transmit Sequences," *Electronics letters*, vol. 33, no. 5, pp. 368–369, 1997.

[39] L. J. Cimini Jr and N. R. Sollenberger, "Peak-to-Average Power Ratio Reduction of an OFDM Signal using Partial Transmit Sequences," in *1999 IEEE International Conference on Communications, 1999. ICC'99*, vol. 1, 1999.

[40] P. K. Frenger and N. A. B. Svensson, "Parallel Combinatory OFDM Signaling," *IEEE Transactions on Communications*, vol. 47, no. 4, pp. 558–567, 1999.

[41] J. Armstrong, T. Gill, and C. Tellambura, "Performance of PCC-OFDM with Overlapping Symbol Periods in a Multipath Channel," in *Global Telecommunications Conference, 2000. GLOBECOM '00. IEEE*, vol. 1, 2000, pp. 87–91 vol.1.

[42] J. A. Davis and J. Jedwab, "Peak-to-Mean Power Control in OFDM, Golay Complementary Sequences, and Reed-Muller Codes," *IEEE Transactions on Information Theory*, vol. 45, no. 7, pp. 2397–2417, 1999.

[43] T. Pollet and M. Peeters, "Synchronization with DMT modulation," *Communications Magazine, IEEE*, vol. 37, no. 4, pp. 80–86, Apr 1999.

[44] P. H. Moose, "A Technique for Orthogonal Frequency-Division Multiplexing Frequency Offset Correction," *IEEE Transactions on Communications*, vol. 42, no. 10, pp. 2908–2914, 1994.

[45] T. M. Schmidl and D. C. Cox, "Robust Frequency and Timing Synchronization for OFDM," *IEEE Transactions on Communications*, vol. 45, no. 12, pp. 1613–1621, Dec 1997.

[46] U. Lambrette, M. Speth, and H. Meyr, "A New Symbol Timing Recovery Algorithm for OFDM Systems," *IEEE Communication Letters*, vol. 1, no. 2, pp. 46–48,, 1997.

[47] J. J. van de Beek, M. Sandell, and P. O. Brjesson, "ML Estimation of Time and Frequency Offset in OFDM Systems," *IEEE Transactions on Signal Processing*, vol. 45, no. 7, pp. 1800–1805, 1997.

BIBLIOGRAPHY

[48] P. S. Chow, J. M. Cioffi, and J. A. C. Bingham, "A Practical Discrete Multitone Transceiver Loading Algorithm for Data Transmission over Spectrally Shaped Channels," *IEEE Transactions on Communications*, vol. 43, no. 234, pp. 773–775, Feb/Mar/Apr 1995.

[49] J. G. Proakis, *Digital Communications (-4th ed.).* McGraw-Hill, 2001.

[50] R. Gallager, *Information Theory and Reliable Communication.* Wiley, 1968.

[51] R. Gaudino, G. Bosco, A. Bluschke, O. Hofmann, N. Kiss, M. Matthews, P. Rietzsch, S. Randel, S. C. J. Lee, and F. Breyer, "On the Ultimate Capacity of SI-POF Links and the Use of OFDM: Recent Results from the POF-ALL Project," in *International Conference on Plastic Optical Fibers*, September 2007.

[52] D. Cardenas, A. Nespola, P. Spalla, S. Abrate, and R. Gaudino, "A Media Converter Prototype for 10-Mb/s Ethernet Transmission Over 425 m of Large-Core Step-Index Polymer Optical Fiber," *IEEE/OSA Journal of Lightwave Technology*, vol. 24, no. 12, pp. 4946–4952, Dec. 2006.

[53] A. A. M. Saleh, "Fundamental Limit on Number of Channels in Subcarrier-Multiplexed Lightwave CATV System," *Electronics Letters*, vol. 25, no. 12, pp. 776–777, June 1989.

[54] D. J. G. Mestdagh, P. Spruyt, and B. Biran, "Analysis of clipping effect in DMT-based ADSL systems," in *Communications, 1994. ICC '94, SUPER-COMM/ICC '94, Conference Record, 'Serving Humanity Through Communications.' IEEE International Conference on*, May 1994, pp. 293–300 vol.1.

[55] D. J. G. Mestdagh, "Calculation of ADC Resolution for DMT Modulation," *Electronics Letters*, vol. 31, no. 16, pp. 1315–1316, Aug 1995.

[56] Application Note 2710. (2003, Sep.) HFAN-02.2.2: Optical Modulation Amplitude and Extinction Ratio. [Online]. Available: http://www.maximic. http://www.maxim-ic.com/appnotes.cfm/an_pk/2710

[57] *IEEE Standard for Information Technology -Telecommunications and information exchange between systems Local and metropolitan area networks Specific requirements Part 3*, IEEE Std. Section 58.7.6, Rev. 802.3-2005, 2005.

[58] I. Mollers, D. Jager, R. Gaudino, A. Nocivelli, H. Kragl, O. Ziemann, N. Weber, T. Koonen, C. Lezzi, A. Bluschke, and S. Randel, "Plastic Optical Fiber Technology for Reliable Home Networking: Overview and Results of the EU Project POF-ALL - [Topics in optical communications]," *IEEE Communications Magazine*, vol. 47, no. 8, pp. 58–68, August 2009.

[59] J. Vinogradov, O. Ziemann, O. Lednicky, J. Gottschalk, M. ZCEh, and S. Tchoupkoua, "Optimal Equalizers for SI-POF and Gpbs," in *International Conference on Polymer Optical Fiber*, August 2008.

[60] F. Breyer, S. C. J. Lee, S. Randel, and N. Hanik, "Real-time Gigabit Ethernet Transmission over up to 25 m Step-Index Polymer Optical Fibre using LEDs and FPGA-Based Signal Processing," in *European Conference on Optical Communications*, September 2009.

[61] ——, "PAM-4 Signalling for Gigabit Transmission over Standard Step-Index Polymer Optical Fiber," in *European Conference on Optical Communications*, September 2008.

[62] D. F. Cardenas Lopez, A. Nespola, S. Camatel, S. Abrate, and R. Gaudino, "100 Mb/s Ethernet Transmission Over 275 m of Large Core Step Index Polymer Optical Fiber: Results From the POF-ALL European Project," *IEEE/OSA Journal of Lightwave Technology*, vol. 27, no. 14, pp. 2908–2915, July15, 2009.

[63] S. Randel, S. C. J. Lee, B. Spinnler, F. Breyer, H. Rohde, J. Walewski, A. M. J. Koonen, and A. Kirstaeter, "1 Gbit/s Transmission with 6.3 bit/s/Hz Spectral Efficiency in a 100 m Standard 1 mm Step-Index Plastic Optical Fibre Link Using Adaptive Multiple Sub-Carrier Modulation," in *Proc. European Conference on Optical Communications 2006, PD4.4.1*, Cannes, France, 2006.

[64] M. Yaseen, S. D. Walker, and R. J. S. Bates, "531-Mbit/s, 100-m All-Plastic Optical Fiber Data Link for Customer-Premises Network Applications," *Conference on Optical Fiber Communication/International Conference on Integrated Optics and Optical Fiber Communication*, p. ThC5, 1993.

BIBLIOGRAPHY

[65] J. Gottschalk, J. Vinogradov, O. Ziemann, and O. Lednicky, "Optimal Equalizers for SI-POF and Gpbs," in *Proceedings of the 17th International Conference on Plastic Optical Fibers*, August 2007.

[66] S. C. J. Lee, F. Breyer, S. Randel, M. Schuster, J. Zeng, F. Huijskens, H. P. A. van den Boom, A. M. J. Koonen, and N. Hanik, "24 Gb/s Transmission over 730 m of Multimode Fiber by Direct Modulation of an 850 nm VCSEL using Discrete Multi-Tone Modulation," in *Optical Fiber Communication Conference*, March 2007.

[67] S. C. J. Lee, A. M. J. Koonen, S. Randel, J. Vinogradov, O. Ziemann, and B. Offenbeck, "10 Gbit/s over Large-Diameter Polymer Optical Fibers using Discrete Multitone Modulation," in *International Conference on Plastic Optical Fibers*, September 2007.

[68] S. C. J. Lee, F. Breyer, S. Randel, H. A. van den Boom, and A. M. J. Koonen, "Orthogonal Frequency Division Multiplexing over Multimode Optical Fibers," in *12th Annual Symposium of the IEEE/Leos Benelux Chapter*, 2007.

[69] S. C. J. Lee, F. Breyer, S. Randel, J. Zeng, H. P. A. van den Boom, and A. M. J. Koonen, "Discrete Multi-Tone Modulation for Low-Cost and Robust 10 Gb/s Transmission over Polymer Optical Fiber," in *European Conference on Optical Communications*, September 2007.

[70] *IEEE P802.3ba 40Gb/s and 100Gb/s Ethernet Task Force*, IEEE Std. [Online]. Available: http://www.ieee802.org/3/ba/

[71] J. Yu, "42.8 Gb/s Chirp-Managed Signal Transmission over 100 m Graded-Index Plastic Optical Fiber," *Optical Fiber Communication Conference and Exposition and The National Fiber Optic Engineers Conference*, p. PDP28, 2008.

[72] S. Schöllmann, C. Wree, A. Joshi, and W. Rosenkranz, "First Experimental Transmission over 50 m GI-POF at 40 Gb/s for Variable Launching Offsets," in *33rd European Conference and Exhibition on Optical Communication ECOC*, 2007.

174

[73] A. Polley and S. E. Ralph, "100 m, 40 Gb/s Plastic Optical Fiber Link," *Optical Fiber Communication Conference and Exposition and The National Fiber Optic Engineers Conference*, p. OWB2, 2008.

[74] H. Yang, S. C. J. Lee, E. Tangdiongga, C. Okonkwo, H. P. A. van den Boom, F. Breyer, S. Randel, and A. M. J. Koonen, "47.4 Gb/s Transmission Over 100 m Graded-Index Plastic Optical Fiber Based on Rate-Adaptive Discrete Multitone Modulation," *IEEE/OSA Journal of Lightwave Technology*, 2010, accepted for publication.

[75] S. C. J. Lee, F. Breyer, S. R. D. Cardenas, H. van den Boom, and T. Koonen, "Discrete Multitone Modulation for High-Speed Data Transmission over Multimode Fibers using 850-nm VCSEL," in *Optical Fiber Communication Conference*, March 2009.

[76] H. Yang, S. C. J. Lee, E. Tangdiongga, F. Breyer, S. Randel, and A. M. J. Koonen, "40-Gb/s Transmission over 100m Graded-Index Plastic Optical Fiber Based on Discrete Multitone Modulation," in *Optical Fiber Communication Conference*. Optical Society of America, 2009, p. PDPD8.

[77] G. Yabre, "Theoretical Investigation on the Dispersion of Graded-Index Polymer Optical Fibers," *IEEE/OSA Journal of Lightwave Technology*, vol. 18, no. 6, pp. 869–877, June 2000.

[78] T. Ishigure, H. Kano, and Y. Koike, "Which is a more serious factor to the bandwidth of GI POF: differential mode attenuation or mode coupling?" *IEEE/OSA Journal of Lightwave Technology*, vol. 18, no. 7, pp. 959–965, July 2000.

[79] P. Pepeljugoski, D. Kuchta, Y. Kwark, P. Pleunis, and G. Kuyt, "15.6-Gb/s Transmission over 1 km of Next Generation Multimode Fiber," *IEEE Photonics Technology Letters*, vol. 14, no. 5, pp. 717–719, May 2002.

[80] P. K. Pepeljugoski and D. M. Kuchta, "Design of Optical Communications Data Links." *IBM Journal of Research and Development*, vol. 47, no. 2-3, pp. 223–238, 2003.

BIBLIOGRAPHY

[81] P. Matthijsse, G. Kuyt, F. Gooijer, F. Achten, R. Freund, L. Molle, C. Caspar, T. Rosin, D. Schmidt, A. Beling, and T. Eckhardt, "Multimode Fiber Enabling 40 Gbit/s Multi-Mode Transmission over Distances >400 m," in *Optical Fiber Communication Conference, 2006 and the 2006 National Fiber Optic Engineers Conference. OFC 2006*, March 2006, pp. 3 pp.–.

[82] S. S.-H. Yam and F. Achten, "Single Wavelength 40 Gbit/s Transmission over 3.4 km Broad Wavelength Window Multimode Fibre," *Electronics Letters*, vol. 42, no. 10, pp. 592–594, May 2006.

[83] S. S.-H. Yam, F.-T. An, M. Marhic, and L. G. Kazovsky, "Polarization Sensitivity of 40 Gb/s Transmission over Short-Reach 62.5 μm Multimode Fiber using Single-Mode Transceivers," in *Optical Fiber Communication Conference, 2004. OFC 2004*, vol. 2, Feb. 2004.

[84] S. S.-H. Yam, F.-T. An, S. Sinha, M. E. Marchic, and L. G. Kazovsky, "40 Gb/s Transmission over 140 m 62.5 μm Multimode Fiber using Polarization Controlled Launch," in *Lasers and Electro-Optics, 2004. (CLEO). Conference on*, vol. 1, May 2004.

[85] L.-G. Zei, S. Ebers, J.-R. Kropp, and K. Petermann, "Noise Performance of Multimode VCSELs," *IEEE/OSA Journal of Lightwave Technology*, vol. 19, no. 6, pp. 884–892, Jun 2001.

[86] K. H. Hahn, M. R. Tan, and S. Y. Wang, "Intensity Noise of Large Area Vertical Cavity Surface Emitting Lasers in Multimode Optical Fibre Links," *Electronics Letters*, vol. 30, no. 2, pp. 139–140, Jan 1994.

[87] J. Y. Law and G. P. Agrawal, "Mode-Partition Noise in Vertical-Cavity Surface-Emitting Lasers," *IEEE Photonics Technology Letters*, vol. 9, no. 4, pp. 437–439, April 1997.

[88] R. E. Epworth, "The phenomenon of modal noise in analogue and digital optical fibre systems," in *European Conference on Optical Communications*, Genova, Italy, September 1978, pp. 492–501.

176

[89] M. Nakamura, N. Suzuki, Y. Uematsu, T. Ozeki, and S. Takahashi, "Laser Linewidth Requirement for Eliminating Modal Noise in Pulse Frequency Modulation Video Transmission," *IEEE/OSA Journal of Lightwave Technology*, vol. LT-2, no. 5, pp. 735–740, October, 1984.

[90] K. H. Hahn, M. R. Tan, Y. M. Houng, and S. Y. Wang, "Large Area Multitransverse-Mode VCSELs for Modal Noise Reduction in Multimode Fibre Systems," *Electronics Letters*, vol. 29, no. 16, pp. 1482–1483, Aug. 1993.

[91] A. M. J. Koonen, "Bit-Error-Rate Degradation in a Multimode Fiber Optic Transmission Link Due to Modal Noise," *IEEE Journal on Selected Areas in Communications*, vol. 4, no. 9, pp. 1515–1522, Dec 1986.

[92] *Lighting of Indoor Work Places, European Stand. EN 12464-1, 2003.*, European Stand. Std.

[93] S. C. J. Lee, J. W. Walewski, S. Randel, F. Breyer, H. P. A. van den Boom, and A. M. J. Koonen, "Discrete Multitone for Noval Application Areas of Optical Communications [Invited]," in *IEEE/LEOS Summer Topicals*, July 2008.

[94] J. Armstrong and A. J. Lowery, "Power Efficient Optical OFDM," *Electronics Letters*, vol. 42, no. 6, pp. 370–372, March 2006.

[95] S. C. J. Lee, S. Randel, F. Breyer, and A. M. J. Koonen, "PAM-DMT for Intensity-Modulated and Direct-Detection Optical Communication Systems," *IEEE Photonics Technology Letters*, 2009, accepted for publication.

List of Publications

Journal Papers

P1. S. Randel, F. Breyer, <u>S. C. J. Lee</u>, and J. W. Walewski, "Advanced Modulation Schemes for Short-Range Optical Communications [Invited]," *IEEE J. Selected Topics in Quantum Electronics*, 2010, accepted for publication.

P2. H. Yang, <u>S. C. J. Lee</u>, E. Tangdiongga, C. Okonkwo, H. P. A. van den Boom, F. Breyer, S. Randel, and A. M. J. Koonen, "47.4 Gb/s Transmission Over 100 m Graded-Index Plastic Optical Fiber Based on Rate-Adaptive Discrete Multitone Modulation," *IEEE/OSA Journal of Lightwave Technology*, 2010, accepted for publication.

P3. <u>S. C. J. Lee</u>, S. Randel, F. Breyer, and A. M. J. Koonen, "PAM-DMT for Intensity-Modulated and Direct-Detection Optical Communication Systems," *IEEE Photonics Technology Letters*, 2009, accepted for publication.

P4. B. Inan, <u>S. C. J. Lee</u>, S. Randel, I. Neokosmidis, A. M. J. Koonen, and J. W. Walewski, "Impact of LED Nonlinearity on Discrete Multitone Modulation," *IEEE/OSA Journal of Optical Communications and Networking*, vol. 1, no. 5, pp. 439–451, Oct, 2009.

P5. <u>S. C. J. Lee</u>, F. Breyer, S. Randel, R. Gaudino, G. Bosco, A. Bluschke, M. Matthews, P. Rietzsch, R. Steglich, H. P. A. van den Boom, and A. M. J. Koonen, "Discrete Multitone Modulation for Maximizing Transmission Rate in Step-Index Plastic Optical Fibers," *IEEE/OSA Journal of Lightwave Technology*, vol. 27, no. 11, pp. 1503–1513, June, 2009.

P6. <u>S. C. J. Lee</u>, S. Randel, F. Breyer, O. Ziemann and A. M. J. Koonen, "DMT Modulation for 1 to 10-Gbit/s Transmission over POF [Invited]", *Fiber and Integrated Optics*, vol. 28, Special Issue: Polymer Optical Fiber, to be published (2009).

List of Publications

P7. <u>S. C. J. Lee</u>, F. Breyer, S. Randel, H.P.A. van den Boom and A. M. J. Koonen, "High-speed transmission over multimode fiber using discrete multitone modulation [Invited]", *OSA Journal of Optical Networking*, vol. 7, pp. 183-196 (2008).

P8. M. Schuster, S. Randel, C.A. Bunge, <u>S. C. J. Lee</u>, F. Breyer, B. Spinnler, K. Petermann, "Spectrally Efficient Compatible Single-Sideband Modulation for OFDM Transmission with Direct Detection", *IEEE Photonics Technology Letters*, May 2008, vol. 20, no. 9, pp. 670-672.

P9. S. Toyoda, K. Fujiura, M. Sasaura, K. Enbutsu, A. Tate, M. Shimokozono, H. Fushimi, T. Imai, K. Manabe, T. Matsuura, T. Kurihara, <u>S. C. J. Lee</u>, H. de Waardt, "KTN-crystal-waveguide-based electro-optic phase modulator with high performance index", *Electronics Letters*, vol. 40, no. 13, pp. 830-831 (2004).

International Conferences

P10. A. M. J. Koonen, <u>S. C. J. Lee</u>, H.-D. Jung, H. Yang, E. Tangdiongga, H. P. A. van den Boom, "Optical Fiber In-Building Networks - Architectures and Techniques [Invited]", Intelligent Buildings and Smart Homes Conference 2009, 18-20 Nov., Taipei, Taiwan.

P11. <u>S. C. J. Lee</u>, F. Breyer, D. Cardenas, S. Randel, T. Koonen, "Real-Time Implementation of a 1.25 Gbit/s DMT Transmitter for Robust and Low-Cost LED-Based Plastic Optical Fiber Applications," proc. European Conference on Optical Communications (ECOC 2009), Vienna, September 2009.

P12. F. Breyer, <u>S. C. J. Lee</u>, D. Cardenas, S. Randel, N. Hanik, "4 Gbit/s over 50-m Large Core Diameter GI-POF using Low-cost VCSEL," proc. European Conference on Optical Communications (ECOC 2009), Vienna, September 2009.

P13. H. Yang, E. Tangdiongga, <u>S. C. J. Lee</u>, S. Randel, H. P. A. van den Boom, T. Koonen, "Real-Time Gigabit Ethernet Transmission over up to 25 m Step-Index Polymer Optical Fibre using LEDs and FPGA-Based Signal Processing,"

proc. European Conference on Optical Communications (ECOC 2009), Vienna, September 2009.

P14. T. Koonen, <u>S. C. J. Lee</u>, H. Yang, H.-D. Jung, E. Tangdiongga, H.P.A. van den Boom, S. Randel, "Research Trends in Optical In-Building Networks [Invited]," CLEO Pacific Rim 2009, Shanghai, China.

P15. H. Yang, <u>S. C. J. Lee</u>, E. Tangdiongga, F. Breyer, S. Randel, A. M. J. Koonen, "40-Gb/s Transmission over 100m Graded-Index Plastic Optical Fiber based on Discrete Multitone Modulation," Postdeadline Paper, PDPD8, OFC 2009, San Diego, CA, USA.

P16. <u>S. C. J. Lee</u>, F. Breyer, S. Randel, D. Crdenas, H.P.A. van den Boom and A. M. J. Koonen, "Discrete Multitone Modulation for High-Speed Data Transmission over Multimode Fibers using 850-nm VCSEL," OWM2, OFC/NFOEC 2009, San Diego, CA, USA.

P17. B. Inan, <u>S. C. J. Lee</u>, S. Randel, I. Neokosmidis, A. M. J. Koonen, J.W. Walewski, "The Impact of LED Transfer Function Nonlinearity on High-Speed Optical Wireless Communications Based on Discrete Multitone Modulation," JThA52, OFC/NFOEC 2009, San Diego, CA, USA.

P18. F. Breyer, <u>S. C. J. Lee</u>, S. Randel, N. Hanik, "PAM-4 signaling for gigabit transmission over standard ste-index plastic optical fibre using light emitting diodes," proc. ECOC 08, (Vol. 3, pp. 81-82). Brussels, country-regionBelgium.

P19. <u>S. C. J. Lee</u>, J.W. Walewski, S. Randel, F. Breyer, H.P.A. van den Boom and A. M. J. Koonen, "Discrete multitone for novel application areas of optical communications [Invited]," IEEE/LEOS Summer Topical Meetings 2008, Acapulco, Mexico (2008).

P20. S. Randel, F. Breyer and <u>S. C. J. Lee</u>, "High-speed transmission over multimode optical fibers [Invited]," OFC/NFOEC 2008, OWR2, San Diego, CA, USA (2008).

P21. O. Ziemann, H. Poisel, S. Randel and <u>S. C. J. Lee</u>, "Polymer optical fibers for short-shorter and shortest data links [Invited]," OFC/NFOEC 2008, OWB1,

San Diego, CA, USA (2008).

P22. <u>S. C. J. Lee</u>, F. Breyer, S. Randel, O. Ziemann, H.P.A. van den Boom, A. M. J. Koonen, "Low-cost and robust 1-Gbit/s plastic optical fiber link based on light-emitting diode technology," OFC/NFOEC 2008, OWB3, San Diego, CA, USA.

P23. F. Breyer, <u>S. C. J. Lee</u>, S. Randel, N. Hanik, "Comparison of OOK- and PAM-4 modulation for 10 Gbit/s transmission over up to 300 m polymer optical fiber," OFC/NFOEC 2008, OWB5, San Diego, CA, USA.

P24. <u>S. C. J. Lee</u>, F. Breyer, S. Randel, H.P.A. van den Boom, A. M. J. Koonen, "Gigabit Ethernet over standard step-index polymer optical fiber," Proceedings of the 17th International Conference on Plastic Optical Fibers (POF 2008) 26 - 28 August 2008, Santa Clara, California, USA. (pp. 1-4).

P25. Ziemann, O. Lednicky, J. Vinogradov, R. Gaudino, H. Kragl, S. Randel, <u>S. C. J. Lee</u>, B. Offenbeck, "The development of Gbps over SI-POF systems in the POF-ALL project," proc. POF 2008. (pp. 1-4). Santa Clara, CA, USA.

P26. Ziemann, S. Loquai, S. Randel, <u>S. C. J. Lee</u>, C.A. Bunge, "New results of mode mixing in PF-GI-POF," proc. POF 2008. (pp. 1-5). Santa Clara, CA, USA.

P27. J. Grubor, <u>S. C. J. Lee</u>, K-D. Langer, A. M. J. Koonen, J. Walewski, "Wireless high-speed data transmission with phosphorescent white-light LEDs," Post-deadline Paper, PDP 3.6, ECOC 2007, Berlin, Germany.

P28. <u>S. C. J. Lee</u>, F. Breyer, S. Randel, J. Zeng, H.P.A. van den Boom, A. M. J. Koonen, "Discrete multi-tone modulation for low-cost and robust 10-Gb/s transmission over polymer optical fibre," Th 9.6.4, ECOC 07, Berlin, Germany (2007).

P29. J. Zeng, <u>S. C. J. Lee</u>, F. Breyer, S. Randel, J. Yang, H.P.A. van den Boom, A. M. J. Koonen, "Transmission of 1.25 Gb/s per channel over 4.4 km silica multimode fibre using QAM subcarrier multiplexing," proc. ECOC 07, W 7.4.3, Berlin, Germany.

P30. F. Breyer, <u>S. C. J. Lee</u>, S. Randel, N. Hanik, "1.25 Gbit/s transmission over up to 100 m standard 1 mm step-index polymer optical fibre using FFE or DFE equalisation schemes," proc. ECOC 07, Th 9.6.6, Berlin, Germany.

P31. S. Randel, A. M. J. Koonen, <u>S. C. J. Lee</u>, F. Breyer, M. Garcia Larrode, J. Yang, A. Ng'Oma, G.J. Rijckenberg, H.P.A. van den Boom, "Advanced modulation techniques for polymer optical fiber transmission [Invited]," proc. ECOC 07, POF Symposium, Th 4.1.4, Berlin, Germany (2008).

P32. S. Randel, M. Schuster, <u>S. C. J. Lee</u> and F. Breyer, "Myths and truths about optical OFDM [Invited]," IEEE LEOS Summer Topicals 2007, Portland, OR, USA (2007).

P33. <u>S. C. J. Lee</u>, A. M. J. Koonen, S. Randel, J. Vinogradov, O. Ziemann, B. Offenbeck, "10 Gbit/s over large diameter polymer optical fibers using discrete multitone modulation," Proceedings of the 16th International Conference on Plastic Optical Fibers (POF 2007) 10 - 12 September 2007, Turin, Italy. (pp. 71-74). Turin, Italy.

P34. S. Randel, <u>S. C. J. Lee</u>, F. Breyer, "1Gbit/s transmission over POF using light emitting diodes," proc. POF 2007. (pp. 111-112). Turin, Italy.

P35. F. Breyer, <u>S. C. J. Lee</u>, S. Randel, N. Hanik, "10 Gbit/s transmission over 220 m perfluorinated graded-index polymer optical fiber using PAM-4 modulation and simple equalization schemes," proc. POF 2007. (pp. 92-95). Turin, Italy.

P36. R. Gaudino, G. Bosco, A. Bluschke, O. Hofmann, N. Kiss, M. Mettthews, P. Rietzsch, S. Randel, <u>S. C. J. Lee</u>, F. Breyer, "On the ultimate capacity of SI-POF links and the use of OFDM: recent results from the POF-ALL project," proc. POF 2007. (pp. 283-288). Turin, Italy.

P37. <u>S. C. J. Lee</u>, F. Breyer, S. Randel, J. Zeng, F.M. Huijskens, H.P.A. van den Boom, A. M. J. Koonen, N. Hanik, "24-Gb/s transmission over 730 m of multimode fiber by direct modulation of an 850-nm VCSEL using discrete multi-tone modulation," Postdeadline Paper, PDP6, OFC 2007, Anaheim, CA, USA.

P38. <u>S. C. J. Lee</u>, F. Breyer, S. Randel, B. Spinnler, I.L. Lobato Polo, D. van den Borne, J. Zeng, E. de Man, H.P.A. van den Boom, A. M. J. Koonen, "10.7 Gbit/s transmission over 220 m polymer optical fiber using maximum likelihood sequence estimation," proc. OFC 07, OMR2, Anaheim, CA, USA.

P39. S. Randel, <u>S. C. J. Lee</u>, B. Spinnler, F. Breyer, H. Rohde, J. Walewski, A. M. J. Koonen, A. Kirstdter, "1 Gbit/s transmission with 6.3 bit/s/Hz spectral efficiency in a 100m standard 1 mm step-index plastic optical fibre link using adaptive multiple sub-carrier modulation," Postdeadline Paper, PDP Th4.4.1, ECOC 2006.

P40. J. Zeng, A. Ng'Oma, <u>S. C. J. Lee</u>, Y. Watanabe, H.P.A. van den Boom, A. M. J. Koonen, "1.25 Gb/s subcarrier modulated transmission over graded-index perfluorinated polymer fibre," Proceedings of the Joint International Conference on Plastic Optical Fiber & Microoptics (POF/MOC 2006) 10 - 14 September 2006, Seoul, Korea. (pp. 96-101). Seoul, Korea.

P41. <u>S. C. J. Lee</u>, H.P.A. van den Boom, R.L. Duijn, S. Randel, B. Spinnler, P.K. van Bennekom, F.M. Huijskens, J. Zeng, A. M. J. Koonen, G.D. Khoe, "2 x 500Mb/s transmission across 25m of 1mm step-index PMMA POF with angular mode group diversity multiplexing," Proceedings of the 15th International Conference on Plastic Optical Fibers (POF 2006) 11 - 14 September 2006, pp. 348-353, Seoul, Korea.

P42. S. Randel, <u>S. C. J. Lee</u>, F. Breyer, H. Rohde, B. Spinnler, "Exploiting the capacity of 1mm PMMA step-index polymer optical fibers," proc. Joint Intern. Conf. on Plastic Optical Fiber & Microoptics (POF/MOC)2006, pp. 443-447, Seoul, Korea.

P43. <u>S. C. J. Lee</u>, H.P.A. van den Boom, R.L. Duijn, P.K. van Bennekom, J. Zeng, S. Randel, B. Spinnler, A. M. J. Koonen, "1.25 Gb/s transmission over 25m of 1mm standard step-index PMMA polymer optical fiber for gigabit Ethernet," Proceedings of the 11th European Conference on Networks & Optical Communications (NOC 2006) 11 - 13 July, pp. 110-117, Berlin, Germany.

Regional Conferences and Workshops

P44. <u>S. C. J. Lee</u>, F. Breyer, S. Randel, H.P.A. van den Boom, A. M. J. Koonen, "Low-cost 10-Gb/s transmission systems with multimode fibre using discrete multitone modulation," proc. ePhoton One Summer School 2007, Brest, France.

P45. F. Breyer, <u>S. C. J. Lee</u>, S. Randel, N. Hanik, "500-Mbit/s transmission over 50 m standard 1-mm step-index polymer optical fibre using PAM4-modulation and simple equalisation schemes," proc. ePhoton One Summer School 2007, Brest, France.

P46. <u>S. C. J. Lee</u>, F. Breyer, S. Randel, H.P.A. van den Boom, A. M. J. Koonen, "Orthogonal frequency division multiplexing over multimode optical fibers," proc. 12th Annual Symposium of the IEEE/LEOS Benelux Chapter 2007, pp. 127-130, Brussels, Belgium.

P47. <u>S. C. J. Lee</u>, F. Breyer, S. Randel, B. Spinnler, I.L. Lobato Polo, D. van den Borne, J. Zeng, E. de Man, H.P.A. van den Boom, A. M. J. Koonen, "Performance of maximum likelihood sequence estimation in 10 Gb/s transmission systems with polymer optical fiber," In Proceedings of the 11th Annual Symposium of the IEEE/LEOS Benelux Chapter, pp. 17-19, 30 Nov. - 1 Dec., 2006, Eindhoven, The Netherlands.

P48. J. Zeng, A. Ng'Oma, <u>S. C. J. Lee</u>, Y. Watanabe, H.P.A. van den Boom, A. M. J. Koonen, "Subcarrier modulated transmission over silica and polymer multimode fibres," In Proceedings of the 11th Annual Symposium of the IEEE/LEOS Benelux Chapter, pp. 193-196, 30 Nov. - 1 Dec. 2006, Eindhoven, The Netherlands.

P49. M. Schuster, B. Spinnler, C.-A. Bunge, S. Randel, <u>S. C. J. Lee</u>, F. Breyer, "Realisierungsmglichkeiten fr OFDM in der optischen Weitverkehrstechnik," 8.ITG-Fachtagung Photonische Netze. Leipzig, Germany (2006).

P50. S. Randel, J. Walewski, H. Rohde, B. Spinnler, F. Breyer, <u>S. C. J. Lee</u>, "In-building gigabit networks based on 1mm PMMA step-index polymer optical fibres," proc. ITG-Konferenz Breitbandversorgung in Deutschland. Berlin.

Books

P51. F. Breyer, N. Hanik, <u>S. C. J. Lee</u>, S. Randel, Getting the Impulse Response of SI-POF by Solving the Time-Dependent Power-Flow Equation using the

Crank-Nicholson Scheme. - In: *POF Modelling - Theory, Measurement and Application, C. A. Bunge, H. Poisel (Ed.)*, December 2007, Verlag Books on Demand GmbH, Norderstedt.

Acknowledgements

Acknowledgements

About the author

Jeffrey Lee was born in Singapore, on October 27, 1979. He received his M.Sc. degree in Electrical Engineering from the Eindhoven University of Technology (TU/e), the Netherlands, in 2005. He started his research in 2003 at NTT Photonics Laboratories in Atsugi (Japan), on the design and characterization of electro-optical phase modulators. Following that, he conducted his Masters thesis work at Siemens AG in Munich (Germany), dealing with the electrical gain control of Erbium-doped fiber amplifiers for long-haul fiber-optic transmission systems.

In September 2005, he started working towards the Ph.D. degree at the TU/e, in collaboration with Siemens AG in Munich (Germany). The research is focused on digital signal processing which includes mainly orthogonal frequency division multiplexing (OFDM) and discrete multitone (DMT) for short-range optical communication channels such as silica multimode fibers, plastic optical fibers, and optical wireless communication systems.

During his Ph.D. studies, he has authored and co-authored more than 50 publications, including 10 invited papers and a book chapter. In addition, he wrote 5 patents related to optical communications. He is a member of the IEEE and serves actively as a reviewer for IEEE and OSA journals. Jeffrey was the winner of the Corning Outstanding Student Paper Award at the Optical Fiber Communications Conference (OFC) 2009.